

Alma Mater Studiorum - Università di Bologna

DOTTORATO DI RICERCA IN

CHIMICA

Ciclo 35

**Settore Concorsuale:** 03/A2 - MODELLI E METODOLOGIE PER LE SCIENZE CHIMICHE

**Settore Scientifico Disciplinare:** CHIM/02 - CHIMICA FISICA

**DRIVE UP ELECTROCHEMICAL AND ELECTROCHEMILUMINESCENCE SIGNAL  
THROUGH BIOSENSING MECHANISM OPTIMIZATION**

Presentata da:

Dott. Pavlos Nikolaou

**Coordinatore Dottorato:**  
Prof. Luca Prodi

**Supervisore:**  
Prof. Francesco Paolucci

**Esame finale anno 2023**

*A mio padre,*

# CONTENTS

<b>ABSTRACT</b>	VIII
<b>INTRODUCTION</b>	1
<b>I Introduction in Electrochemiluminescence (ECL)</b>	2
I.1 ECL annihilation mechanism	2
I.2 ECL Coreactant mechanism	3
I.3 ECL advantages	4
<b>II Introduction in Biosensors</b>	4
II.1 Different types of biosensors	5
II.2 ECL and biosensors	6
<b>III Magnetic Beads Introduction</b>	7
III.1 Magnetic beads in biosensors uses	7
III.2 Magnetic beads, ARRAYS and ASSAYS	8
<b>The aim of the thesis</b>	11
<b>References</b>	12
<b>CHAPTER 1</b>	14
<b>Can a metal-based dye be replaced by a free one?</b>	
<b>1.1 Introduction</b>	15
1.1.1 Metal based luminophores dyes	15
1.1.2 Iridium complexes	17
1.1.2.1 Iridium complexes for ECL applications	17
1.1.2.2 Applications in life science	18
1.1.3 Ruthenium complexes	19
1.1.3.1 Ruthenium complexes for ECL applications	20
1.1.3.2 Ruthenium complexes in life science	21
1.1.3.3 Ruthenium complexes with dipyrido-[3,2-a:2',3'-c]-phenazine (-dppz) ligand	23

1.1.3.4 [Ru(phen) <sub>2</sub> (dppz)] <sup>2+</sup> as intercalated agent	24
1.1.4 Metal-free Thermally Activated Delayed Fluorescence Materials	25
1.1.5 Metal-free Boron-dipyrromethene based luminophores	27
<b>1.2 Iridium dyes in aprotic conditions</b>	<b>29</b>
1.2.1 Electrochemical characterization for the iridium complexes	31
1.2.2 Electrochemiluminescence features of Iridium complexes	33
1.2.3 Comparison among Iridium complexes	35
<b>1.3 Ru[(1,10-phenanthroline)<sub>2</sub>dipyrido[3,2-a:2',3'-c]phenazine]<sup>2+</sup> complex dye in aprotic conditions</b>	<b>37</b>
<b>1.4 Electrochemical and Electrochemiluminescence features of Thermally Activated Delayed Fluorescence Materials in aprotic conditions</b>	<b>39</b>
1.4.1 Electrochemical characterization of TADF	40
1.4.2 ECL efficiency for TADF molecules	42
<b>1.5 Photophysical and Electrochemiluminescence of novel coumarin based oxazaborines</b>	<b>43</b>
1.5.1 Electrochemical characterization	44
1.5.2 Photochemical properties	45
1.5.3 Electrochemiluminescence study	46
1.5.4 ECL efficiency for OxaBo compounds	47
<b>1.6 Conclusions</b>	<b>48</b>
<b>References</b>	<b>49</b>

## CHAPTER 2

<b>Would the use of semi-conductors for Electrochemiluminescence applications be possible?</b>	54
<b>2.1 Introduction</b>	<b>55</b>

2.1.1 Semiconductors	55
2.1.1.1 Energy band theory	56
2.1.1.2 Endogenous Semiconductors	57
2.1.1.3 Exogenous Semiconductors	58
2.1.2 Titanium Dioxide (TiO <sub>2</sub> )	59
2.1.2.1 Electronic structure of TiO <sub>2</sub>	60
2.1.2.2 Uses and advantages of TiO <sub>2</sub>	60
2.1.3 Zirconium dioxide (ZrO <sub>2</sub> )	61
<b>2.2 Electrochemical characterization of Mox materials using ECL</b>	61
2.2.1 Electrochemical performance for Mox	62
2.2.2 Ruthenium complex immobilized in Mox/FTO electrodes in different thicknesses	65
<b>2.3 Conclusions</b>	69
<b>References</b>	69
<b>CHAPTER 3</b>	72
<b>Can we develop an ultra-sensitive biosensor without any sequence and/or signal amplification?</b>	
<b>3.1 Introduction</b>	73
3.1.1 Hepatitis B Virus (HBV)	74
3.1.1.1 PCR and PCR-free methods for the diagnosis of HBV	75
3.1.2 Sars-CoV-2 (COVID-19)	76
3.1.3 Polymerase Chain Reaction (PCR)	78
3.1.3.1 Polymerase Chain Reaction free (PCR-free)	78
<b>3.2 Electrochemical platform preparation for HBV whole genome detection</b>	79
3.2.1 Analytical procedure	80
<b>3.3 Thermodynamic studies</b>	81

3.3.1 Surface electrochemical characterisation using electrochemistry	82
3.3.2 Detection of whole synthetic genome of HBV	83
3.3.2.1 Detection of HBV Extracted genome	85
3.3.2.2 Analytical differences between extracted and synthetic genome of HBV	86
3.3.3 Mechanism of the reaction	87
3.3.4 pH effect	88
3.3.5 Applicability in biological matrixes and selectivity	89
<b>3.4 Detection of whole genome of COVID-19</b>	<b>90</b>
3.4.1 COVID-19 synthetic genome quantification	90
3.4.2 Point of care-based sensor for the determination of extracted COVID-19 genome	92
3.4.3 Detection of COVID-19 genome using HT procedure	97
3.4.3.1 Detection of COVID-19 genome using biological matrixes and one step protocol	98
3.4.3.2 Investigations on the matrix effect	99
<b>3.5 Conclusions</b>	<b>100</b>
<b>References</b>	<b>101</b>
<b>CHAPTER 4</b>	<b>104</b>
<b>Surfaces could be replaced by other platforms such as magnetic beads?</b>	
<b>4.1. Introduction</b>	<b>105</b>
4.1.1 Magnetic Beads for electrochemiluminescence applications	106
4.1.2 Magnetic beads conjugated with luminophore complexes	107
<b>4.2 Analytical approach in a standard electrochemical system using MBs</b>	<b>108</b>
4.2.1 Chemicals and Materials	108

4.2.2 Instrumentation	109
<b>4.3 Preparation of ASSAY</b>	109
4.3.1 Amperometric detection of HRP	111
4.3.2 Optimal conditions	111
<b>4.4 Analytical characteristics for the determination of HRP</b>	114
4.4.1 Mechanism and electron-proton transfer	116
4.4.2 Stability and capture efficiency	119
<b>4.5 Magnetic beads directly conjugated with iridium dyes</b>	120
4.5.1 Preparation of MBs@Ir(III) conjugation	122
4.5.2 Electrochemiluminescence readout for MBs@Ir(III)	122
<b>4.6 Conclusions</b>	124
<b>References</b>	124
<b>Conclusions and perspectives</b>	126
<b>Ringraziamenti/ Acknowledgements/Ευχαριστίες</b>	128

# ABSTRACT

Biomarkers are biological indicators of human health conditions. Their ultra-sensitive quantification is of cardinal importance in clinical monitoring and early disease diagnosis. Biosensors are some worldwide simple and easy-to-use analytical devices as a matter of fact, biosensors using electrochemiluminescence (ECL) are one of the most promising biosensors that needs an ever-increasing sensitivity for improving its clinical effectiveness.

The principal aspiration of this project is the investigation of the ECL generation mechanisms for enhancing the ECL intensity and the development of an ultrasensitive sensor, the use of metal-oxide materials (Mox) and the substitution of metal-free dyes. Novel dyes such as BODIPY, TADF are used to improve the sensitivity of ECL techniques thanks to their advantageous and tunable properties, enhancing the signal and also the ECL efficiency. Additionally, the use of Mox could be beneficial for the investigation of two different ECL mechanisms, which occur simultaneously.

In this thesis, the investigation of size and distance effects on electrochemical (EC) mechanisms was carried out through the innovative combination of a standard detection system using different size of micromagnetic beads (MBs). That allowed the discovery of an unexpected and highly efficient mechanistic path for electrochemical generation at small distances from the electrode's surface. The smallest MBs (0.1 $\mu$ m) demonstrate an enhancement of electrochemical signal than the bigger one (2.8 $\mu$ m) until 4 times of magnitude.

Finally, a novel ultrasensitive sensor, based on the coreactant-luminophores mechanism, was developed for the determination of whole viral genome specific for cardiac HBV and COVID-19 virus.

In conclusion, the ECL and the use of EC techniques (such as amperometry), improved the understanding of mechanisms responsible for the ECL/EC signal led to a great enhancement in the signal.



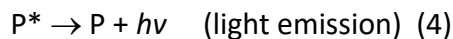
# **INTRODUCTION**

# I Introduction in Electrochemiluminescence (ECL)

Electrogenerated chemiluminescence (ECL) is a unique combination of electrochemistry and spectroscopy, that is used as a powerful analytical technique offering high sensitivity and selectivity, low noise to signal ratios and wide dynamic range for sensing and detecting applications. The ECL signal can be produced in the surface of an electrode via applied voltage undergo high-energy electron-transfer reaction to generate electronically excited states that luminescent signals[1][2]. It must be mentioned that ECL does not require an external light source, which not only simplifies the detection apparatus but also reduces the background noises compared to the conventional photoluminescence sensing system, leading to high sensitivity.

## I.1 ECL annihilation mechanism

In general, the principal mechanism of ECL is generated via annihilation, that involves homogeneous electron transfer reaction between electrochemically generated anions and cations which are produced on the surface of the electrode. This annihilation mechanism is mentioned below [Eq. 1-4]



in which P=luminophore, A=oxidized luminophore, D=reduced luminophore and P\*=luminophore excited state.

That was the first ECL phenomenon presented in 1927 by Dufford et al. from the observation of light emission during the electrolysis of Grignard compounds in anhydrous media[3]. On the other hand, in the 1980's Bard and co-workers[4][1] proposed different approaches to the generation of ECL in protic media, in particular in aqueous solutions, whose mechanism was based on the reaction between a so-called coreactant and the luminophore. This strategy conducted the application of ECL to aqueous environments, making it suitable for the analysis of bio-related samples. Typically, in coreactant-ECL, the excited state is generated through the reaction between two different precursors, an emitter (i.e., the luminophore) and a coreactant chosen among various classes of chemicals, whose fundamental feature is to present a highly unstable oxidized (or reduced) form that undergoes a fast-chemical degradation, forming a high-energy radical. In that way, two different mechanisms are possible, depending on the nature of the coreactant; the oxidative-reduction or the reductive-oxidation one. In all cases, the rate-determining steps for the overall process including the kinetics underlying the heterogeneous electron transfer reactions of the coreactant, the stability of coreactant radicals, and the distribution of ECL luminophores can influence the ECL efficiency[5][6].

## I.2 ECL Coreactant mechanism

The most known system for coreactant ECL, in use, is the combination of *tripropyl-n-amine* (TPA) as coreactant and tris(2,2'-bipyridine) ruthenium (II)  $[\text{Ru}(\text{bpy})_3^{2+}]$  as emitter, both in aqueous solution.

In such a system, the application of a positively enough potential drives the simultaneous oxidation of both dye and coreactant, both free to diffuse in solution (Figure I.1a). By contrast, in the commercial immunoassay application, the luminophore  $\text{Ru}(\text{bpy})_3^{2+}$  is usually anchored, following the biorecognition event, onto, e.g., the surface of a magnetic microbead distanced from the electrode surface, preventing any direct electron transfer to the electrode. Bard and co-workers proposed a variant of the previous mechanism explaining the observation of the ECL emission under such conditions, i.e., when the oxidation of TPA only occurs[7]. This mechanism involves both  $\text{TPA}^{\bullet}$  and  $\text{TPA}^{\bullet\bullet}$  (figure I.1b).

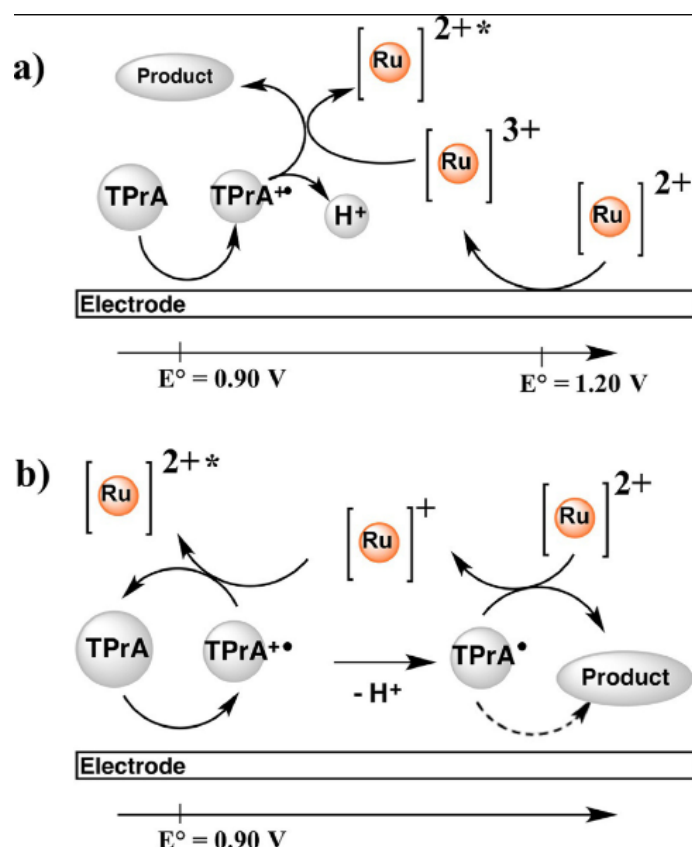


**Figure I.1:** ECL mechanisms for the couple  $\text{Ru}(\text{bpy})_3^{2+}/\text{TPA}$ : a) both luminophore and coreactant are oxidized in the “oxidative-reduction” mechanism; b) ECL generation obtained only by TPA oxidation and involving the homogeneous reaction of the radical cation ( $\text{TPA}^{\bullet\bullet}$ ), as proposed by Bard[7]. The luminophore in the excited state  $\text{Ru}^{2+*}$  relaxes to the ground state and emits photon. Reproduced from Ref.[8], copyright 2015, with permission of American Chemical Society.

In the coreactant process for ECL biosensing, luminophores mainly include inorganic complex, organic compound, and nanomaterial, while the coreactants mainly involve peroxydisulfate ( $\text{S}_2\text{O}_8^{2-}$ ) for the cathodic coreactant process and TPA and hydrogen

peroxide ( $H_2O_2$ ) for the anodic coreactant process. In recent years, extensive research has been performed on ECL, particularly in bioanalysis, bioimaging, nanomaterials and detection devices owing to its high sensitivity and selectivity, low background and simplified optical setup[9].

### **I.3 ECL advantages**

Although electrochemiluminescence technology has achieved fine and continuous innovation in the development of detection systems, the design, synthesis of ECL properties of materials, and collaboration with other devices, are challenges still present that have to be undertaken in the future [10],[11]. Some of the ECL advantages are mentioned below:

1. ECL allows high signal-to-noise measurement because ECL does not require an excitation light source and thus background noise due to scattered light is reduced.
2. ECL is a highly localized and time-triggered detection method since ECL signal generating reactions will only take place on the electrode for the duration of an applied potential.
3. ECL is a powerful analytical technique used in many areas, ranging from fundamental studies to practical applications such as pharmaceutical analysis, immunoassays, clinical diagnosis and environmental analysis, among others [12].

## **II Introduction in Biosensors**

A sensor is a device that responds to a physical or chemical stimulus, such as heat, light, sound, pressure, magnetism, or a specific movement, and transmits a result in the form of a thrust. A sensor, therefore, can recognize an internal signal (or energy) and convert it into the appropriate external signal (or other form of energy). Since Clark and Lyons invented the glucose sensor in 1962, many biological elements have been added to the sensor to produce an electrical signal that is a function of the concentration of the analyte being assessed [13]. Umesh Lad, Santosh Khokhar, and Girish M. Kale of the University of Leeds (U.K.) observed the trends in electrode design, materials, and fabrication and assess performance of creatinine biosensors in terms of selectivity, sensitivity, stability, and response time [14]. Biosensors combine a biological recognition material that responds to the substance being measured with a transducer whose function is to convert an observe changes into a measurable signal. The biological element can be either a biocatalyst (enzymes, microorganisms, tissue material) or a bioligand (antibody, nucleic acids, lipid layers, genome). Typically, the biorecognition element can be attached directly to the transducer or retained within a carrier material, which is subsequently deposited at the transducer surface (figure I.2). The choice of immobilization process is important because the active sites

of the biorecognition element should not be compromised. In addition, the immobilization process also affects the lifetime of the biosensor in terms of storage and operational stability.

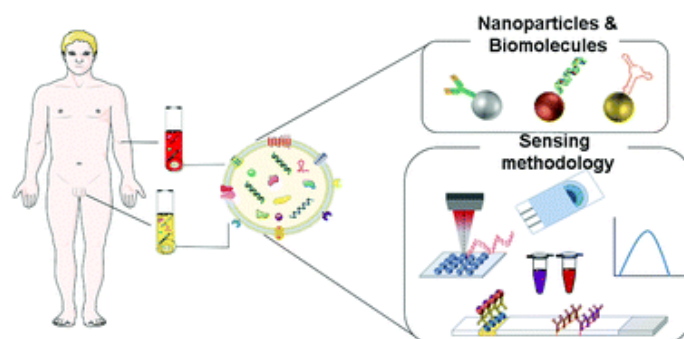


**Figure 1.2:** Methods and targets for biosensing application. With the permission of [15].

## II.1 Different types of biosensors

Biosensors are classified based on: a) The signal converter used b) the nature and mode of action of the recognition of biomolecule and c) the immobilization method. Based on the signal converter, biosensors are distinguished into optical (measurement of the absorbance, fluorescence and chemiluminescence), electrochemical (Amperometric and potentiometric), thermal (measuring the release and absorption of heat), gravimetric measuring the change in mass and there are two types, the piezoelectric and acoustic surface waves [16–20] (figure 1.3).

Optical biosensors are very widespread because through them the change in the optical properties (absorption or fluorescence) of the recognized biomolecule occurs during the detection of the analyte or the analyte itself. Electrochemical biosensors are the most widespread and frequently used biosensors. The signal transducer is electrochemical and is usually held on an electrode's surface. They rely on some enzyme-catalyzed reaction that leads to the formation of products that are detected. Converting the signal from electrochemical to measurable electrical is easy and inexpensive.

Specifically, the electrochemical signal of electrochemical biosensors is divided into a potentiometric and amperometric ones.

- Potentiometric biosensors: calculate the oxidation/reduction potential of an electrochemical reaction. The potential that flows through an electrochemical cell under zero current conditions is recorded.
- Amperometric biosensors are self-contained integrated devices based on the measurement of the current resulting from the oxidation or reduction of an electroactive biological element providing specific quantitative analytical information.

Gravimetric biosensors are divided into piezoelectric (Piezoelectric) and surface acoustic wave (Surface Acoustic wave). Both of them, are mass sensors since they exhibit a linear relationship between the change in mass on the surface of the crystal and its frequency of oscillation. Also, thermal biosensors focus on the recognition of the analyte from the biomolecule, the temperature is measured by the heat that is released or absorbed.

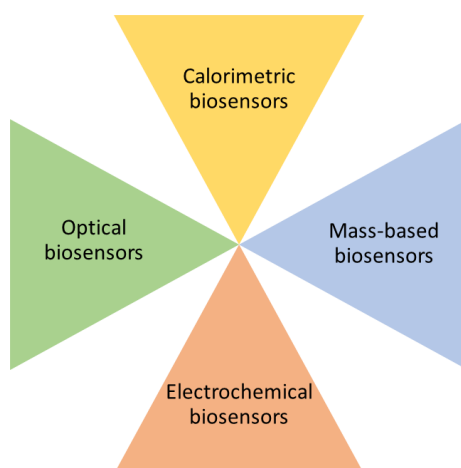


**Figure I.3:** Different types of biosensors.

Based on the type of recognition biomolecule, biosensors are divided into Enzymatic (immobilized enzymes and proteins), DNA biosensors (nucleic acids), cellular biosensors (immobilized cells or a tissue), Immunosensors (immobilized antibody or antigen coupled to an enzyme or dye) and Microorganism Biosensors.

## II.2 ECL and biosensors

The biosensors can be easily combined with the ECL approach. The applications of a typical system in an ECL immunoassay and DNA assay for clinical diagnostic were reported in 1991 [21]. Jameison et al. reported significant research on ECL enzyme biosensors in 1996 [22]. In their research, many classical chemistry analytes were commonly quantified by coupling them to enzyme systems that either utilized b-nicotinamide adenine co-factors or produced  $H_2O_2$ . Their ECL biosensor systems mainly included ECL detection of NADH using dehydrogenases and  $H_2O_2$  using oxidases. ECL biosensing method generally uses biomolecular probes and ECL reagents/materials to measure the concentration of target molecules by translating a biochemical interaction into a quantifiable ECL signal. The classical molecular recognition elements mainly include antibody, single-strand DNA (ss-DNA), enzyme, and biological receptor, etc. According to the recognition principle, the ECL biosensing methods are mainly cataloged into immunoassay, DNA hybridization biosensing, and enzyme catalytic biosensing. In order to understand the advantages of ECL biosensing

methods, here, the advantages of ECL immunoassay (ECLIA) as an example is presented compared with that of other immunoassays. Since radio-immunoassays (RIAs) were first employed for measuring endogenous plasma insulin in 1959, the labeled immunoassays using label reagents, such as chromogenic, fluorescent, CL, biochemiluminescence (BCL), electrochemical, ECL reagents, and enzymes have been greatly developed. Although RIAs are currently employed in hospitals, they are gradually replaced by other labeled immunoassays, such as CL and BCL immunoassays, because radioactivity is health harming and increases environmental pollution. Fluorescent immunoassays endure from fluorescence of proteins itself, and enzyme-labeled immunoassays go through enzyme instability and low bioaffinity of a big enzyme-labeled antibody. Electrochemical immunoassays are limited by their low reproducibility and low sensitivity. Therefore, ECLIA has been extensively employed in clinical diagnosis, and some ECLIA kits have been commercialized.

### **III Magnetic Beads Introduction**

Magnetic beads (MBs) have been recently exploited as supports and/or carriers. MBs have particular characteristics that make them useful in biosensor configurations: they are biocompatible, they have large surface area, they can be easily functionalized, and their location and transport can be controlled by a magnetic field. MBs used in biomedical applications usually present a core/shell structure. Such microbeads have an inorganic core e.g. iron oxide, surrounded by an outer layer of shell wall that consists of long-chain organic ligands or inorganic/organic polymers. The attachment of bioactive ligands to the surface of the outer shell is the key to bio-application of MBs[23].

#### **III.1 Magnetic beads in biosensors uses**

Many types of biosensors have been using surface-functionalized magnetic particles to recognize specific molecular targets with high sensitivity and selectivity. In the field of biomedical applications, a wide spectrum of advanced materials, including micro and nanoparticles, have been developed for sample preparation and biosensing platforms [27][28]. The use of magnetic particles has allowed the biomedical processes to be quick, simple, robust, and high-throughput systems. A lot of reviews present several cases of magnetic materials applied in isolation/pre-concentration of various target molecules and their use in recent biosensing platforms for biomedical applications [24–26]. It has been highly anticipated that these current developments in magnetic particle may contribute to future innovation in point-of-care and high-throughput systems to increase the chance of successful diagnostics and clinical treatments. The use of MBs as antibody immobilization support is described in several magneto-controlled competitive immunoassays and immunosensors. In the simplest approach, the immunocomplexes are first formed and later captured on magnetized electrodes for the electrochemical measurement.

### III.2 Magnetic beads, ARRAYS and ASSAYS

Magnetic beads can be easily coated with different biomolecules, as presented in figure I.4, such as DNA, Proteins, antibodies and/or chemical groups (-COOH, -NH<sub>2</sub>). In every case, MBs can be used for the creation of an ASSAY and the detection of a specific analyte.

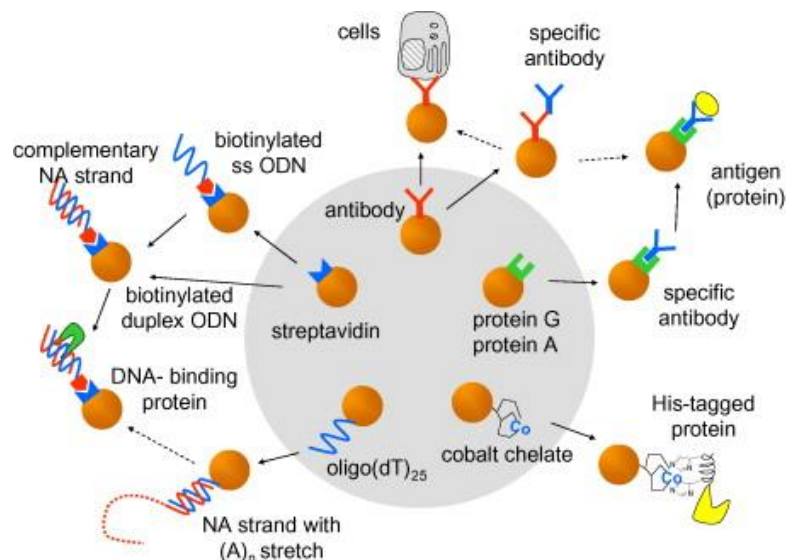


**Figure I.4:** Magnetic beads (MBs) as versatile tools for bioassays. MBs modified with various recognition elements (examples of commercially available MBs shown on the gray background) can be used for specific bioaffinity capture of different molecules. With the permission of [29].

Microbead-based arrays are an emerging technology used for early diagnosis, in simultaneous detection, quantification, and profiling of a range of targets of interest relevant to a particular disease. Preliminary work was carried out as early as 1926 when various particulate materials were used in biological investigations. The first systematic study of the development of well-defined albumin microspheres for diagnostic applications was performed in the late 1960s by Rhodes, Scheffel, Wagner, Zolle and their colleagues [30]. Attempts towards optimizing and developing antibody-based multiplexed assays (and commercial instruments and kits) date back to over 20 years ago. By using a multiplex detection-based system, scientists can predict the possibility of disease occurrence before the appearance of the first clinical symptoms at the very early stages. Biomarkers may be related to genetic information such as a mutation or change in amino acid positions in a double-stranded DNA or RNA structure, alterations in a complex protein or gene structure, or the appearance of a single specific (or multiple) antigens that correlate with the presence of a disease. This technology also has significant applications in the analysis of protein/gene/DNA profiles, experiments for drug discovery, research, and optimization of clinical



laboratory diagnosis [31–34]. Certain particular biomarkers have been shown to be characteristic of many specific disease states, or other physiological interferences of an organism that can be used as an indicator to diagnosis or predict disease [35][36][37].

There are two basic different types of microbead-based technologies: solid-state planar bead arrays, and liquid-state suspension bead arrays, which both have extensive multiplexing capability (figure I.5).

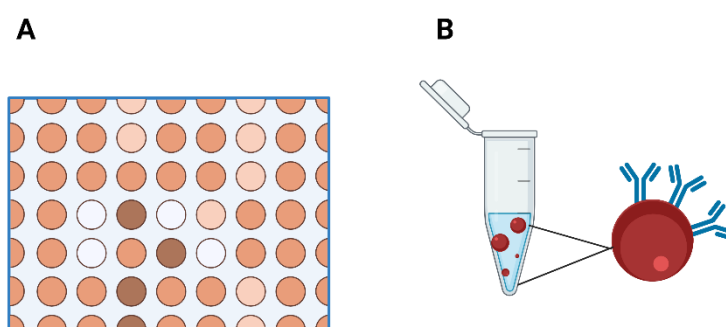


**Figure I.5:** Schematic representation of A) planar array and B) suspension array.

In the microbead planar array format (figure I.5A), microspheres are attached in place at known locations onto a solid surface by various means (such as creating microholes and micromachined cavities etc.). The solid surfaces can be made of polymers or glass [38]. Binding reactions take place in the same way as for suspension arrays, and ultimately there is a two-dimensional array consisting of false or true reacted spots. The multiplexed suspension arrays (figure I.5B) are composed of a mixture of optically encoded polymeric microspheres each conjugated to a specific antibody or other ligand designed to recognize and capture different specific analytes.

High-throughput screening of biomarkers in clinical analysis can be achieved by a multiplexing approach, which means simultaneous quantification of many different biomarkers whose interrelated expression levels combined, may be indicative of an individual disease, or show the presence of one particular type of disease such as cancer, neurological or infectious disease. Multiplexed bioassays increase the sensitivity and provide a more efficient, fast and accurate diagnosis using a single relatively small sample volume [39–41].

In suspension bead-based assays, suspended beads are mixed with a sample containing different antigens or analytes [42]. The detection principles of suspension bead based assays can be categorized into three subtypes: protein determination (immunoassays), nucleic acid detection, and receptor-ligand assays. Immunoassays are probably the most important analysis method for biological molecules, as the molecular recognition reaction provides high selectivity and chemical sensitivity. Although conventional microtiter plate assays continue to play an important role, enzyme assays, DNA binding, and competitive immuno-assays have

been performed on microdevices [43]. Firstly, the microbead-based immunoassay detection principle mainly includes sandwich-type assays and competitive type assays[44]. In a competitive assay, the interaction of unlabeled analyte (usually the antigen in the sample) with the labeled antibody on the surface of microspheres is the goal. A reduction in the binding of the labeled antigen then signifies the presence of the unlabeled form. In this system, the detectable signal declines with an increase in analyte concentration, which creates a high background signal. On the other hand, in non-competitive immunoassay formats (usually sandwich-type formats), the antigens are captured by bead-conjugated primary antibodies and then sandwiched between the primary antibody and a matching fluorescently labeled secondary detector antibody as is used in a traditional sandwich immunoassay complex. This assay type can achieve the highest level of sensitivity because of the use of two matching antibodies.

## The aim of the thesis

Aforesaid, the ultrasensitive quantification of biomarkers in biological samples is such as current, as a future challenging topic in the field in electrochemistry and especially in the early disease diagnosis. ECL is an electrochemical technique which can be used for this aim in this PhD project.

In the first chapter, different metal, and metal-free dyes luminophores will be analyzed using ECL technology. New dyes will be used for the enhancement of ECL signal owing a higher ECL efficiency than the classic ruthenium dyes. Initially, as it is described in paragraph I.1 the study of annihilation mechanism in ECL will be mandatory for the calculation of ECL efficiency. Standard dyes of Ru[(bpy)<sub>3</sub><sup>2+</sup>] and Iridium complexes with different ligands will be analyzed via annihilation mechanism and the possibility of their replacement with metal-free dyes, will be discussed.

In the second chapter, different semiconductor materials will be investigated using Ru[(bpy)<sub>3</sub><sup>2+</sup>] and TPA in the homogeneous phase. Three different thicknesses of TiO<sub>2</sub> will be explored furthermore using ECL technology replying to if a semiconductor could be used in ECL application and in biosensors.

However, in chapter 3, according to the results of chapter 1 and 2, the preparation of an ultra-sensitive biosensor for the detection of viral genome will be talked through. In particular in this chapter prompted by the pandemic diseases COVID-19 we will develop an ultrasensitive method without any amplification of sequence and/or signal is required. The DNA of hepatitis type B (HBV) virus and the RNA of COVID-19 has been chosen as DNA and RNA case of study. The method is based on the combination of surface cooperative hybridization of HBV genome and ECL transduction using the [Ru(phen)<sub>2</sub>dppz]<sup>2+</sup> complex (phen = 1,10-phenanthroline; dppz = quinoxalino[2,3-f][1,10]phenanthroline) as ECL-active dye. The analytical performances of the PCR-free biosensor using both synthetic HBV and COVID-19 genome (SG ds-HBV, SG-COVID-19) and samples extracted from real samples (EG ds-HBV, EG-COVID-19) are presented and argued.

In the final chapter we will review the possibility of replacing the standard platforms in biosensors field with magnetic beads (MBs). These magnetic beads will host our system of sensing and according to their size properties the electrochemical signal will be enhanced. Moreover, novel dyes of Iridium with different ligands will be attached according to streptavidin-biotin bond binding in the surface of MBs debating if it could be possible to replace the ruthenium dyes in ECL technology.

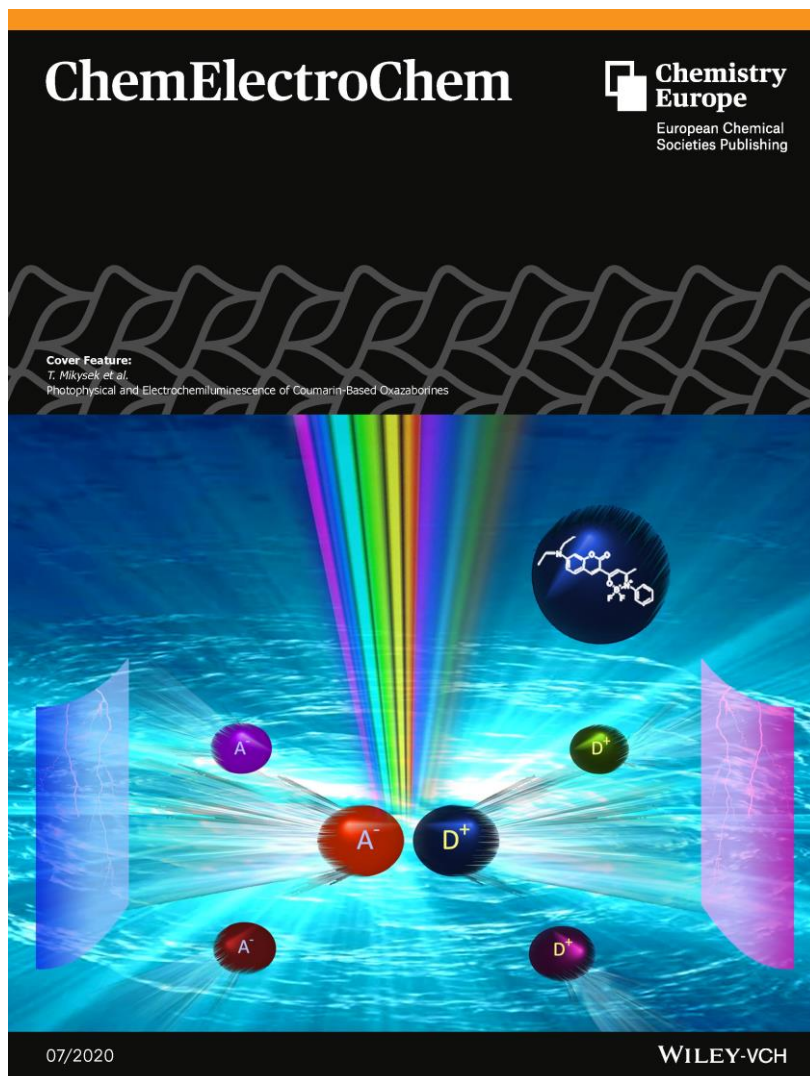
On this wise, we will demonstrate how the combination of ECL, semi-conductor materials and different dyes compounds can give us new ways for developing ultrasensitive biosensors improving and enhancing the ECL signal. Moreover, it also paves the combination of new worldwide used MBs in the field of biosensors in electrochemistry, only by changing their size in a standard early diagnostic system.

## References

- [1] H.S. White et al. *J. Am. Chem. Soc.* 104 (1982) 6891–6895.
- [2] W. Miao *Chem. Rev.* 108 (2008) 2506–2553.
- [3] R.T. Dufford et al. *J. Am. Chem. Soc.* 49 (1927) 1858–1864.
- [4] M. Hesari et al. *J. Electrochem. Soc.* 163 (2016) H3116–H3131.
- [5] L. Chen et al. *Chem. Sci.* 10 (2019) 8654–8667.
- [6] E.J. O’Reilly et al. *RSC Adv.* 5 (2015) 67874–67877.
- [7] W. Miao et al. *J. Am. Chem. Soc.* 124 (2002) 14478–14485.
- [8] K. Imai et al. *J. Phys. Chem. C.* 119 (2015) 26111–26118.
- [9] A. Fiorani et al. *Anal. Chem.* 90 (2018) 12959–12963.
- [10] S. Zhang et al. *Front. Chem.* 8 (2021) 1–7.
- [11] S. Kesarkar et al. *ChemElectroChem.* 4 (2017) 1690–1696.
- [12] X. Liu et al. *Biosens. Bioelectron.* 201 (2022) 113932.
- [13] L.C.C. Jr. et al. *ANNALS.* 102 (1962).
- [14] U. Lad et al. *Anal. Chem.* 80 (2008) 7910–7917.
- [15] B. Martín-Gracia et al. *J. Mater. Chem. B.* 8 (2020) 6710–6738.
- [16] D.R. Thévenot et al. *Biosens. Bioelectron.* 16 (2001) 121–131.
- [17] E. Cesewski et al. *Biosens. Bioelectron.* 159 (2020) 112214.
- [18] J. Wang *Biosens. Bioelectron.* 21 (2006) 1887–1892.
- [19] B. Danielsson et al. *Sensors Actuators B. Chem.* 6 (1992) 138–142.
- [20] G. Samourganidis et al. *Coatings.* 8 (2018).
- [21] G.F. Blackburn et al. *Clin. Chem.* 37 (1991) 1534–1539.
- [22] F. Jameison et al. *Anal. Chem.* 68 (1996) 1298–1302.
- [23] G.T. Hermanson et al. *Bioconjugate Techniques.* Academic Press (1992).
- [24] D.K. Yi et al. *J. Am. Chem. Soc.* 127 (2005) 4990–4991.
- [25] A.L. Elrefai et al. *J. Magn. Mater.* 474 (2019) 522–527.
- [26] Y. Xianyu et al. *TrAC - Trends Anal. Chem.* 106 (2018) 213–224.
- [27] K. Wu et al. *Nanotechnology.* 30 (2019).
- [28] Y. Ha et al. *ACS Appl. Nano Mater.* 1 (2018) 512–521.
- [29] E. Paleček et al. *Talanta.* 74 (2007) 276–290.
- [30] P.R. Srinivas et al. *Lancet Oncol.* 2 (2001) 698–704.

- [31] M.J. Fritzler, M.L. Fritzler *Expert Opin. Med. Diagn.* 3 (2009) 81–89.
- [32] S. Rödiger et al. *Microchim. Acta.* 181 (2014) 1151–1168.
- [33] J.P. Nolan et al. *Trends Biotechnol.* 20 (2002) 9–12.
- [34] L.A. Fraser et al. *Molecules.* 20 (2015) 21298–21312.
- [35] O. Golubnitschaja et al. *Surv. Ophthalmol.* 52 (2007) 155–161.
- [36] M.S. Pepe et al. *J. Natl. Cancer Inst.* 93 (2001) 1054–1061.
- [37] X. Luo et al. *Chem. Soc. Rev.* 42 (2013) 5944–5962.
- [38] J. Thompson *Penn Diss.* (2011) 152.
- [39] Y. Leng et al. *Chem. Soc. Rev.* 44 (2015) 5552–5595.
- [40] H.Y. Hsu et al. *Electrophoresis.* 30 (2009) 4008–4019.
- [41] A. Sukhanova et al. *Crit. Rev. Oncol. Hematol.* 68 (2008) 39–59.
- [42] R. Wilson et al. *Angew. Chemie - Int. Ed.* 45 (2006) 6104–6117.
- [43] M.A.M. Gijs *Microfluid. Nanofluidics.* 1 (2004) 22–40.
- [44] P. Antal-Szalmás et al. *Cytom.* 23 (2013) 1–8.

# CHAPTER 1



**Can a metal-based dye be replaced by  
a free one?**

## 1.1 Introduction

As it mentioned at the introductory chapter, electrochemiluminescence (ECL) are a sensitive detection modality, where high energy states are produced on the surface of electrodes which facilitate electron transfer. This electron transfer phenomenon yields to excite species and subsequently emit light which can be recorded as an intensity signal [1]. Various compound such as 9, 10-diphenylanthracene (DPA) or ECL luminophores were discovered [2]. Tris(2, 2'-bipyridyl) dichlororuthenium(II) hexahydrate ( $[\text{Ru}(\text{bpy})_3]\text{Cl}_2$ ) was used as the ECL luminophore.  $[\text{Ru}(\text{bpy})_3]^{2+}$ , showed strong luminophore characteristics, and provided high chemical stability in aqueous solutions with high emission quantum yield and a long excited state duration of  $\sim 600$  ns [3],[4]. The ECL luminophores can be grouped in two main categories: inorganic complexes and organic molecules[5–7].

Coordination complexes based on transition metals, such as ruthenium [8–10], iridium[10–13], osmium [14],[15] and platinum[16],[17] are the main dyes used in real ECL application. Among all the investigated metals, ruthenium is the forefather and the most widely used, while iridium is gaining more attention for its promising higher efficiency. Organic molecules has been the subject of investigation since the beginning of ECL studies[18], leading the way to inorganic complexes which are more suitable for sensing in water solutions, where ECL finds its application. However, new concepts such as aggregation-induced emission (AIE) and thermally-activated delayed fluorescence (TADF) brought a renewed interest for ECL organic emitters, in particular, the possibility to use water solutions and a hypothetical 100% internal conversion by up-conversion of triplet excitons in singlet excitons, respectively. Hither, the investigated mechanism is the annihilation mechanism as it was presented in the Chapter (I.1) of the introduction.

### 1.1.1 Metal based luminophores dyes

The general structure of cyclometalated dyes is presented in figure 1.1 with the later C-N ligands.

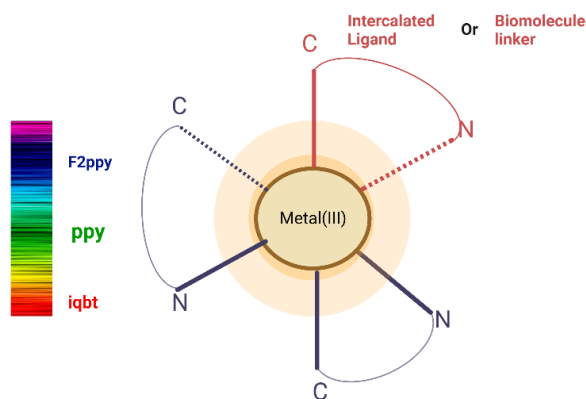


**Figure 1.1:** Structure of metal-based luminophores dyes.

The general structure of the cyclometalated (III) complexes includes; one metal(III) core ion surrounded by three equal bidentate monoanionic ligands. Usually, the atoms of the ligand, which are bonded to the metal(III) central ion, are N and C (with a formal negative charge) including the coordinative disposition and involving the formation of a five- or six-membered metallacycle. These C<sup>N</sup> ligands and their resulting complexes are named cyclometalating ligands. Most of the cyclometalating ligands have one neutral coordinating part and one anionic part. The metal–C bond between the metal(III) and carbon atom of C<sup>N</sup> ligands is usually strong enough to be comparable to covalent bonds that leads to a multiply bonded and compact structure with extensive electronic interactions between the d-orbital of metal(III) ion and  $\pi$ -orbital of the ligands; some possible C<sup>N</sup> ligands are presented in figure 1.2.

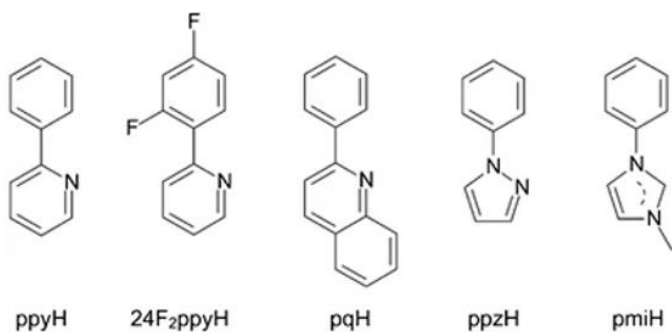


**Figure 1.2 :** Different C<sup>N</sup> ligands.

In the beginning of the 21<sup>st</sup> century, it has been reported from Fuyuki et al. [19], Gross et al. [20], and Bruce and Richers [21], that among many different C<sup>N</sup> ligands could be attached to iridium(III) core, the most popular is 2-phenylpyridine (ppy) forming facial isomer of Ir(ppy)<sub>3</sub> chelate, particularly interesting from the ECL point of view because the neutral Ir(ppy)<sub>3</sub> molecule is formally isoelectronic with Ru(bpy)<sub>3</sub><sup>2+</sup> cation.



The isoelectronic character of these two species allowed one to expect observation of the ECL emission from Ir(ppy)<sub>3</sub> chelate.

### 1.1.2 Iridium complexes

According to previous reported works of Bruce and Richers in 21<sup>st</sup> century [21], a consequence of the relatively weak oxidizing power of the iridium complex and the higher energy of its emission [22] ( $E^0_{\text{Ox}} = 0.86 \text{ V vs. SCE}$ ;  $\lambda_{\text{max}} = 530 \text{ nm}$ ) [23] compared [Ru(bpy)<sub>3</sub>]<sup>2+</sup> ( $E^0_{\text{Ox}} = 1.35 \text{ V vs. SCE}$ ;  $\lambda_{\text{max}} = 620 \text{ nm}$ ). Kapturkiewicz [24] was the first to consider the importance of the electron transfer reactions leading to the ECL of iridium complexes. His studies introduced a roadmap for the synthesis of more ECL efficient iridium complexes and the following years saw a range of new ECL systems based on cyclometalated iridium complexes with ligands such as 2-phenylbenzothiazole [25] and 2-phenylbenzimidazole [26]. Although, efficient co-reactant iridium ECL seemed elusive at this stage, the fundamental understanding gained in this work opened the door for new applications for luminescent iridium complexes in ECL-based sensing and biosensing [27].

#### 1.1.2.1 Iridium complexes for ECL applications

Several studies have been reported on the aspects in the ECL of cyclometalated iridium (III) complexes, especially co-reactant ECL in water solution for biosensing applications. For example Zhou *et al.* [28] showed an extremely sensitive ECL-based detection method using [Ir(ppy)<sub>2</sub>(dcbpy)]<sup>+</sup> (ppy: 2-phenylpyridyl and dcbpy: 4,4'-dicarboxy-2,2'-bipyridyl), to investigate carbohydrate expression on cell surfaces with a potential application in studying disease such as Alzheimer and cancer.

In a novel approach, Schmittel *et al.* [29–31] defined the concept of “lab-on-a-molecule” and employed it for a series of chemical and biochemical sensing applications. They also showed a chloro-bridged iridium dimer [(pq)<sub>2</sub>IrCl]<sub>2</sub> as a dual channel operator for the detection of cyanide and acetate anions using PL and ECL in aqueous solutions, respectively. Their strategy was based on the weak PL of the iridium dimer which increased by over 350-fold in the presence of cyanide. On the other hand, the complex produced no ECL in the presence of cyanide, which dramatically increased in the presence of acetate anions. The requirements of lab-on-a-molecule probes for efficient multi-analyte detection were summarized in a recently reviewed article [32]. De Cola *et al.* have described a series of neutral bis-cyclometalated iridium(III) complexes with outstanding ECL properties in aqueous media [33]. One complex in particular, [Ir(pphent)<sub>2</sub>(pic)] (where pphent = phenylphenanthridine and pic = picolinate), outperformed Ru(bpy)<sub>3</sub><sup>2+</sup> by a factor of 3.7 under conditions similar to those used in immunoassays. Iridium-based

electrochemiluminophores, showing outstanding results in organic solvent, are found to underperform in the presence of water. Although the color emission for this series did not differ very much from that of the ruthenium standard, which is clearly a promising direction for enhanced detection limits in real world bioanalytical applications.

The advent of electrochemiluminescent systems based on cyclometalated iridium complexes has allowed unprecedented opportunity for tuning the photophysical and electrochemical properties of ECL emitters. This, combined with improvement in spectroscopic and electrochemical instrument design, opened interesting new possibilities. These techniques are typically used to probe a system with two or more luminophores with differing emission colours and/or oxidation potentials, the mixture is subjected to various potentials or a continuously varying electrode potential and the resultant ECL spectra are recorded. Potential-resolved ECL systems were reported in 2012 by Schmittel *et al.*[34]. This control is expected to be beneficial not only for novel multi-analyte detection systems, but also for the design of multi-coloured ECLs.

### 1.1.2.2 Applications in life science

Amongst the various metal complexes, cyclometalated iridium(III) species [35–37] have received extensive investigation for applications in life science. Typically, these complexes comprise an iridium(III) center bound to two cyclometalated ligands such as phenylpyridine and one bidentate ligand such as a picolinamide. The chemical nature of this family of complexes can be readily tuned by chemical variations of the coordinated ligands, thus allowing tuning of properties such as charge, lipophilicity, and solubility, as well as photoluminescent characteristics. In fact, it is known that iridium complexes can be tuned to be emissive across the entire range of the visible spectrum, from blue to red, and further in the near-infrared region. Given this versatility, it is not surprising that a large number of iridium complexes have been investigated for their potential application as cellular markers and therapeutic agents. The strategies adopted to design iridium (III) complexes for life science can be broadly divided into two categories. Complexes can be conjugated to biological or targeting vectors, with the aim of inducing a specific biological behavior. For example, the complex could be bioconjugated to target localization within a specific organelle such as mitochondria, to interact with specific biological species such as a proton in the measurement of intracellular pH, or to sense and quantify the presence of specific analytes also for the development of immunoassays combined with magnetic beads (figure 1.3). The complexes can also be designed to exhibit a photophysical response that is able to be modulated by the targeted event, as for example in the case of fluorogenic turn-on species or ratiometric complexes [38]. On the other hand, the complexes might lack bioconjugation, and their biological behavior can be investigated to elucidate a structure–activity profile. In this case, it becomes immediately apparent how a rationalization between structure and activity is quite complex to achieve, even though it would be extremely beneficial for the design of advanced and superior iridium complexes for targeted applications in life science. The main critical aspects that are typically invoked in structure–activity studies are charge,

lipophilicity and solubility [39]. These are indeed very useful, but in general these considerations seem to be appropriate for small sub-libraries of complexes that have analogous chemical formulations. What constitute also a complication is the fact that very often the experimental conditions used by the research groups worldwide are very different, with variations occurring on the specific cell lines used, concentration, incubation time, imaging time, and imaging protocol. These aspects often lead to results that are not just dependent on the chemical nature and characteristics of the metal complex. Nonetheless, the field has rapidly broadened in the past decades from being just limited to cellular imaging.

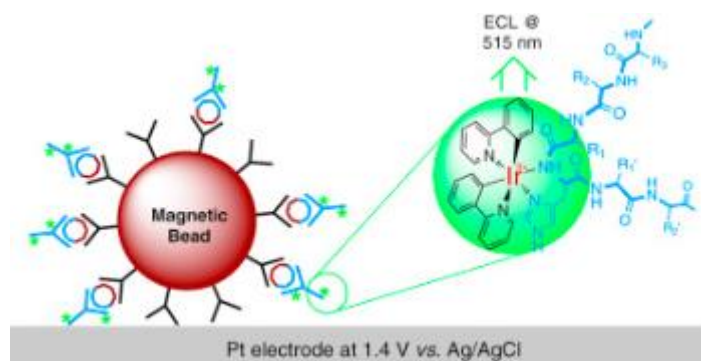


**Figure 1.3:** ECL immunoassay featuring the on-site formation of the iridium (III) luminophores. With the permission of [40].

### 1.1.3 Ruthenium complexes

Over the last couple of years, the field of coordination and organometallic chemistry of ruthenium (Ru) has grown and evolved at unprecedented rates. Recent publications largely highlight key advances on Ru-based complexes and on their chemically addressable applications in challenging areas like biology, medicine, catalysis, nanoscience, redox and photoactive materials, *etc.* [41],[42]. This explosive expansion is mainly due to the unique ability of the ruthenium core to permit multiple oxidation states, hence versatile electron-transfer pathways.

Both Ru(II) and Ru(III) oxidation states accommodate six-coordinated octahedral configurations in which the additional axial ligands help fine-tune the steric and electronic properties of the complexes. Of consequence are also the relative weakness of certain metal-ligand bonds as well as the thermodynamic and kinetic stability of Ru(III)-complexes vs. Ru(II)-complexes since ligand exchange kinetics are immediately affected [43]. Proper variations of ancillary ligands, allowing modulation of redox properties and ligand interactions, have resulted in a large platform of Ru complexes endowed with achiral or chiral configurations [44–47]. While older research takes new directions, cutting-edge applications have emerged in the already mentioned fields, yet also in materials science, petrochemistry, and oleochemistry. Further valorization of Ru complexes in photochemistry and photophysics, for pharmaceuticals and agrochemicals will undoubtedly be forthcoming. Admittedly, this brief overview cannot cover the huge diversity of recently introduced ruthenium complexes and concentrates essentially on concepts and trends disclosed during 2013–2014 and early

2015. A critical appraisal of these aspects is presented showcasing Ru-driven advances in anticancer chemotherapy, medicinal applications, catalysis, water oxidation, photoactive complexes, functional and nanomaterials and complex design that have newly taken center stage.

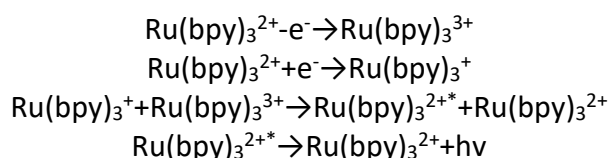
### 1.1.3.1 Ruthenium complexes for ECL applications

Tokel and Bard's work [48] about the emission from the excited state of  $\text{Ru}(\text{bpy})_3^{2+}$  formed via the electrochemical method started the application of the  $\text{Ru}(\text{bpy})_3^{2+}$  ECL in analytical science. Since then,  $\text{Ru}(\text{bpy})_3^{2+}$  ECL has become a sensitive detection method and  $\text{Ru}(\text{bpy})_3^{2+}$  has also been one of the most studied and exploited inorganic ECL compounds to date because of its stability and its capability of undergoing ECL at room temperature in aqueous buffered solutions. As reported in several scientific publications,  $\text{Ru}(\text{bpy})_3^{2+}$  has been widely used in ECL flow cells and probe injection analysis systems to detect various chemicals and biochemical assays [49][50].

Compared with the solution-phase ECL procedure, the immobilization of the  $\text{Ru}(\text{bpy})_3^{2+}$  makes experimental design simple and the cost low because there is no need to deliver extra  $\text{Ru}(\text{bpy})_3^{2+}$  reagent.

Although  $\text{Ru}(\text{bpy})_3^{2+}$  ECL detection has some benefits, there are some drawbacks, such as lack of selectivity and dependence on the environmental factors, e.g., viscosity [51], temperature, surfactant [52], ion strength, and pH. However, the lack of selectivity can be overcome by coupling  $\text{Ru}(\text{bpy})_3^{2+}$  ECL with flow injection analysis (FIA), high-performance liquid chromatography (HPLC), capillary electrophoresis (CE) and micro total analysis systems ( $\mu\text{TAS}$ ), as discussed in the following sections.  $\text{Ru}(\text{bpy})_3^{2+}$  ECL, as a detection method with detection limits of sub-picomolar concentration and an extremely wide dynamic range, has been used successfully for the determination of oxalate and some amine-containing analytes in FIA, HPLC, CE and  $\mu\text{TAS}$ .

Generally, a  $\text{Ru}(\text{bpy})_3^{2+}$  ECL reaction is initiated in three main ways. The first ECL reaction sequence is based on the annihilation of  $\text{Ru}(\text{bpy})_3^+$  and  $\text{Ru}(\text{bpy})_3^{3+}$ , which are produced by applying a suitable voltage. When  $\text{Ru}(\text{bpy})_3^+$  reacts with  $\text{Ru}(\text{bpy})_3^{3+}$ , the excited state  $\text{Ru}(\text{bpy})_3^{2+*}$  results, and that produces an orange emission centered on 610 nm. The above annihilation reaction can be carried out as redox-cycling procedure by using interdigitated carbon electrodes [53]. The original  $\text{Ru}(\text{bpy})_3^{2+}$  species is regenerated in the following procedure:



This mechanism was analytically described in the introduction chapter named as annihilation mechanism.

### 1.1.3.2 Ruthenium complexes in life science

Though started over 50 years ago, the development of metal anticancer drugs has traditionally focused on cytotoxic platinum compounds, several of which have reached clinical application [54]. The deeper understanding of cancer biology triggered the introduction of targeted chemotherapies, using other metal-based drugs, able to address specific cancer physiologies or disease states [55][56]. As most of the ruthenium complexes are less toxic than their platinum counterparts, this progress offers considerable added value for medical implementation. Although so far none of the ruthenium complexes are in clinical use as anticancer drugs, the remarkable success in clinical trials of NAMI-A, KP1019, and KP1339, combined with abundant reports on the enhanced *in vitro* and *in vivo* activity of other types of ruthenium complexes, prompted ruthenium chemotherapeutics to rapidly become a major area in anticancer drug advancement [57][58]. In an illustrative example NAMI-A, inactive against primary tumors but specifically targeting tumor metastases, was shown to display an improved antimetastatic activity when turned into macromolecular NAMI-A, a biocompatible amphiphilic block copolymer forming micelles that increase the cytotoxicity and cell uptake of the drug. In the search for superior metallodrugs, ruthenium chemistry is taking momentum through the introduction of Ru-containing macromolecular complexes (dendrimers, dendronized polymers, protein conjugates, intelligent nanoparticles for advanced drug delivery, and polymer Ru-complex conjugates) that better differentiate between tumor cells and healthy cells [58].

Currently considered among the most promising alternatives to platinum drugs, active by interaction with DNA, ruthenium complexes also operate via different mechanisms [59][60]. Both Ru(II) and Ru(III) oxidation states are stable in physiological solutions, with the latter considered to be less reactive; therefore, Ru complexes are generally reported to act as redox-activatable prodrugs. Recent research largely illustrates that the *in vitro* and *in vivo* properties of ruthenium compounds can be finely tuned by ligand variation. Intense investigations converge on ligand selection from the arene, phosphine, aromatic heterocycles, pyridine, pta, pybox, pyrazolone-based  $\beta$ -ketoamine, nitrosyl, Schiff-base, carboxamide, carbothioamide, thiourea, thiocarbamate, thiosemicarbazone, and hydrazone classes [61–65]. Innovations were applied to construct coordination-driven self-assembled arene-Ru metallic-rectangles endowed with stronger cytotoxicity against all cancer cell lines and even more effective than established anticancer drugs like doxorubicin and cisplatin [66]. That interest in the bioactivity profiles of ruthenium complexes has grown rapidly is amply demonstrated by design of new Ru compounds inhibiting enzymes, by the novel multinuclear systems acting as drug delivery vehicles or imaging and theranostics agents and signal transduction elements. A major contribution came as well from the advent of refined bioanalytical, biophysical and spectroscopic techniques used to elucidate the structure and the *in vivo* functioning of these complexes[67],[68]. Some arene-functionalized dinuclear organometallic Ru(II) complexes are capable of crosslinking model peptide and oligonucleotide sequences while cytotoxicities are linked to their more rigid or more flexible conformations. The mechanism of action of

ruthenium-based antitumor drugs was studied, especially in regard to the capacity of ruthenium to mimic iron in its binding to biological molecules. Along these lines, new ruthenium complexes containing the enantiopure ligands 2,6-bis[4'-l-phenyloxazolin-2'-yl-pyridine] ((*R,R*)-Ph-pybox), 2,6-bis[4'(*S*)-isopropylloxazolin-2'-yl-pyridine] ((*S,S*)-*i*Pr-pybox) or 2,6-bis[4'-l-isopropylloxazolin-2'-yl-pyridine] ((*R,R*)-*i*Pr-pybox) and the water soluble 1,3,5-triaza-7-phosphaadamantane (PTA) or *N*-substituted PTA phosphanes, have been synthesized. Their interactions with plasmidic DNA and cytotoxic activities against human cervical cancer HeLa cell lines have been evaluated, evidencing the distinct ability of the enantiomeric ligands in affecting the cell cycle of HeLa tumor cells.

Incorporation of biologically-derived ligands that primarily aim at minimizing toxicity toward normal cells is a viable avenue for engineering ruthenium complexes since they provide ways to improve antiproliferative activity of metal-based drugs. Such ligands display different coordination modes, facilitate compatibility of the complex with the biological environment, and promote a higher cellular uptake. The diversity of bio-relevant ligands installed as essential components of ruthenium complexes ranges from amino acids, peptides, proteins, carbohydrates, purine bases and oligonucleotides to steroids and other bioactive entities endowed with specific properties [69],[70]. This methodology is confirmed by excellent studies on Ru complexes that open unique opportunities for rational design and production of potent ruthenium anticancer drugs tackling distinct transport pathways and mechanisms of action.

Photoactivation of ruthenium complexes for triggering and/or modulating their antitumor activity [71],[72] is presently of great interest. The process enables transformation of unreactive Ru(II) complexes into light-driven cytotoxic species [73] that can subsequently interact with proteins and DNA at the cellular level. In some representative examples, it has been demonstrated that, using a clinical grade photodynamic therapy laser source, red-to-blue upconverting liposomes were capable of triggering photodissociation of ruthenium polypyridyl complexes from PEGylated liposomes [74]. Several ruthenium(II) polypyridyl complexes have been elaborated to act as two-photon absorption agents in mitochondria-targeted photodynamic therapy, a promising new technique for resolving tumors selectively and subduing resistance to alternative anticancer therapies. Cellular toxicity induced by photorelease of certain bioactive molecules has been proved as a valid alternative for Ru photodynamic therapeutic agents (PDT) with dual-action [75].

When photoactivated, surface-grafted ruthenium complexes on mesoporous silica nanoparticles undergo photoexpulsion and subsequent release as cytotoxic entities toward cancer cells [76]. Nowadays, numerous accounts on photoactivatable Ru(II) complexes that exhibit different types of biologically relevant activities have been published [77],[78]. Of real consequence for therapeutic purposes, catalytic reactions induced in cells by certain metallodrugs pertaining to the class of redox modulators or photosensitizers may ensure low-dose therapy protocols. An interesting catalytic procedure demonstrated that transfer hydrogenation promoted by Noyori-type

ruthenium complexes can reduce coenzyme  $\text{NAD}^+$  to  $\text{NADH}$  in human ovarian cancer cells by using non-toxic concentrations of formate as a hydride donor source [79]. Such advanced catalytic processes enhance capabilities of ruthenium complexes, while also increasing selectivity towards cancer cells *versus* normal cells.

Ruthenium complexes additionally find important medicinal applications as nitric oxide carriers and donors for induction of vascular relaxation (some  $\text{Ru(III)}$  complexes can act as nitric oxide scavengers thus improving graft survival). Drugs based on specific  $\text{Ru}$  complexes are active against parasitic diseases (e.g., leishmanicidal and protozoanidal agents), as antibacterial, antifungal and anticorrosion additives in coatings on  $\text{Ti}$ -alloys used in medical devices[80],[81].

### 1.1.3.3 Ruthenium complexes with dipyrido-[3,2-a:2',3'-c]-phenazine (-dppz) ligand

Among the  $\text{Ru(II)}$  polypyridyl complexes,  $[\text{Ru}(\text{bpy})_2\text{dppz}]^{2+}$  (figure 1.4) is one of the most well studied molecules, where  $\text{bpy} = 2,2'$ -bipyridine,  $\text{dppz} = \text{dipyrido}[3,2\text{-}a:2',3'\text{-}c]\text{phenazine}$ . In 1990, the Barton group first reported that  $[\text{Ru}(\text{bpy})_2\text{dppz}]^{2+}$  could serve as a non-radioactive luminescent DNA probe[82]. This complex shows no photoluminescence in aqueous solution at ambient temperature but displays intense photoluminescence in the presence of double-helix DNA, with an enhancement factor of  $>10^4$ . This phenomenon, which is known as the DNA “light-switch” effect, has attracted much attention and has been used extensively to study the interaction of metal polypyridyl complexes with DNA.

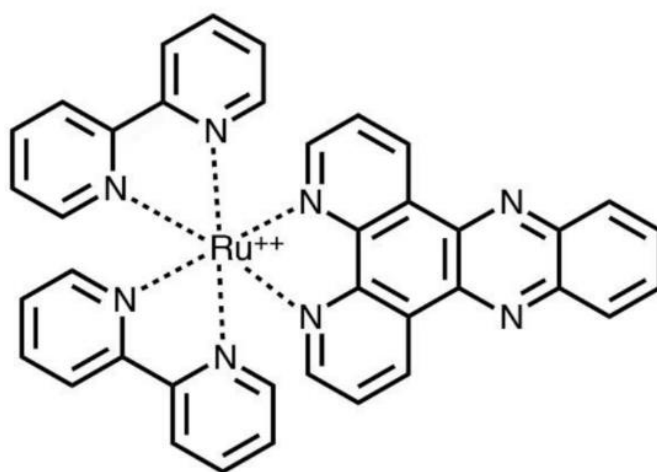


**Figure 1.4:** Molecular structure of  $[\text{Ru}(\text{bpy})_2(\text{dppz})]^{+2}$ .

Rather than presenting a thorough history of the development of  $\text{Ru}$ - $\text{dppz}$  complexes in the past few decades, in this perspective, we focus on advances in applications of the  $\text{Ru}$ - $\text{dppz}$  system. Strategies for the modification of  $\text{Ru}$ - $\text{dppz}$  complexes are discussed that leverage the DNA binding affinity, DNA damage, and cellular uptake of the  $\text{Ru}$ - $\text{dppz}$  complexes. However, extensive discussion of such modifications of  $\text{dppz}$  is beyond the scope of this perspective. Recent comprehensive reviews on the

photophysical properties, environmental effects and substituent effects of dppz compounds provide additional details for many of these systems[83],[84]. In particular, we place emphasis on the recent advances in novel applications in DNA intercalation for the development of ECL biosensors.

#### **1.1.3.4 [Ru(phen)<sub>2</sub>(dppz)]<sup>2+</sup> as intercalated agent**

One of the most studied complex families in the last ten years is that of compounds type [Ru (L)<sub>2</sub>dppz]<sup>2+</sup>, where L represents a range of aromatic ligands with structures similar to bipyridyl or phenanthroline (phen). However, if double strand DNA is present in solution, its luminescence greatly increases. This is a consequence due to the very high intercalating capacity of the -dppz which, inserted in the double helix of the DNA, cannot form hydrogen bonds with water, with the consequent increase in the life time of the excited state of the complex which can therefore be deactivated by radiative way: if it is present the double helix the life time of the excited state of the complex is about 200 ns, while in the absence of DNA it drops to about 200 ps [85]. To better understand this behavior, let us consider in detail the characteristics of the excited state of the complex (Figure 1.5). The absorption of light radiation overall causes a charge transfer from the metal to the binder (MLCT transition). The initial Frank-Condon state in which the electron is transferred from the metal center to the orbitals of the ligands is followed by a rapid localization of the charge towards the non-coordinating nitrogen of the dppz ligand. The excited state that is thus formed is responsible for the strong emission (at about 620 nm) in non-aqueous solvents. In water, as already mentioned, the hydrogen bonds between the solvent molecules and the nitrogens of the -dppz originate a non-emitting state. When the -dppz ligand intercalates in the DNA double helix, the formation of the aforementioned hydrogen bonds is prevented, and the luminescence effect is comparable to that observed in non-aqueous solvents.



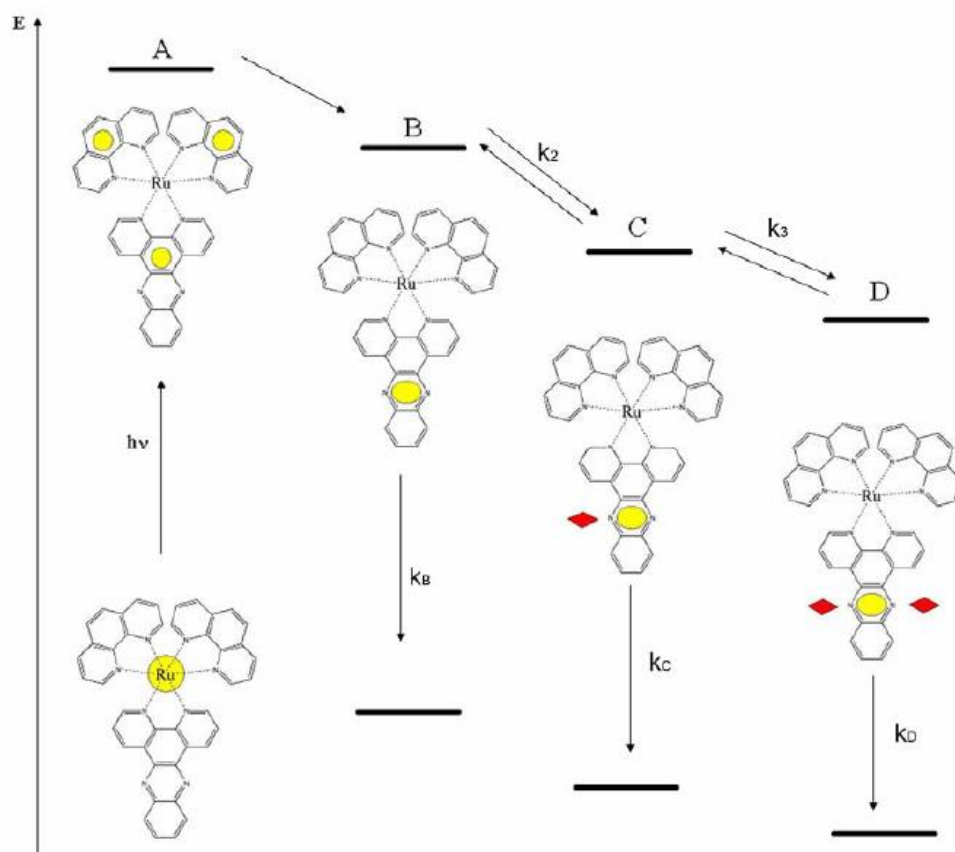


**Figure 1.5:** Schematic description of the different excited states of  $[\text{Ru}(\text{phen})_2\text{dppz}]^{2+}$ . The first excitation is the metal-bonding charge transfer (MLCT).

An interesting fact is the difference of about seven orders of magnitude in the emission efficiency between the  $\Delta$  and  $\Lambda$  enantiomer of the complex. Both are able to fit between the nitrogenous base pairs of the major sulcus of the B-DNA, but the  $\Delta$  has a greater intercalation density thanks to a more favorable orientation of the phenanthroline ligands with respect to the direction of helix winding.

#### 1.1.4 Metal-free Thermally Activated Delayed Fluorescence Materials

Over the past decades, the rapid developments of both materials technology and biomedicine have accelerated the exploitation of a wide variety of new functional materials, providing potential alternatives for diagnosis and treatment of various diseases, especially cancer. However, exploring advanced luminescent materials as theragnostic agents with ideal photophysical properties and reliable biosafety is still urgently needed. In recent years, a report of thermally activated delayed fluorescence (TADF) materials with an extremely small singlet-triplet energy gap ( $\Delta E_{ST}$ ) performing theoretically 100% internal quantum efficiencies (QE) via the reverse intersystem-crossing (RISC) process, followed by delayed fluorescence emission [129]. Since the pioneering Nature paper of Adachi and co-workers in 2012[128], considerable efforts have been triggered to develop efficient TADF materials for different applications including optoelectronics, bioimaging, biosensors, and nanomedicine. Strikingly, by virtue of the tailorable synthesis, low-cost input, favorable photophysical features (e.g., long-lived emissive feature), and excellent biocompatibilities (e.g., metal-free

molecular structure), the purely organic TADF materials have shown fascinating appeal in the field of biomedicine [86–88].

Typically, the distinct optical and electronic properties of TADF materials could be attributed to the sufficiently small  $\Delta E_{ST}$  between the  $S_1$  and  $T_1$  states, enabling an efficient RISC process and a resultant  $\approx 100\%$  internal QE by harvesting both singlet and triplet excitons, which is a crucial theoretical breakthrough in organic electronics. Likewise, such unique optical properties render TADF materials as promising candidates for biomedical applications. Despite the great potential of TADF mechanism in the ECL field, there are rare reports on this topic. Previously, Ishimatsu et al. reported liquid-phase annihilation ECL using TADF small molecules, i.e. 1,2,3,5-tetrakis(carbazol-9-yl)-4,6-dicyanobenzene (4CzIPN) and its derivatives [89]. Generally, two types of ECL mechanisms are represented in TADF: the prompt ECL and the delayed ECL. In general, TADF emitters are triggered by the application of the potential and follows the annihilation mechanism, where 25% singlet and 75% triplet excitons are generated via hole and electron injection (Figure 1.6). Assuming non-radiative decay and phosphorescence emission are ignored, the triplet excitons could retransform into singlet excitons by RISC process, and both the initial and back-formed singlet excitons could realize prompt ECL and delayed ECL emission. Hence, the efficient triplet to singlet transformation is essential to maximize electrochemiluminescence of TADF molecules.

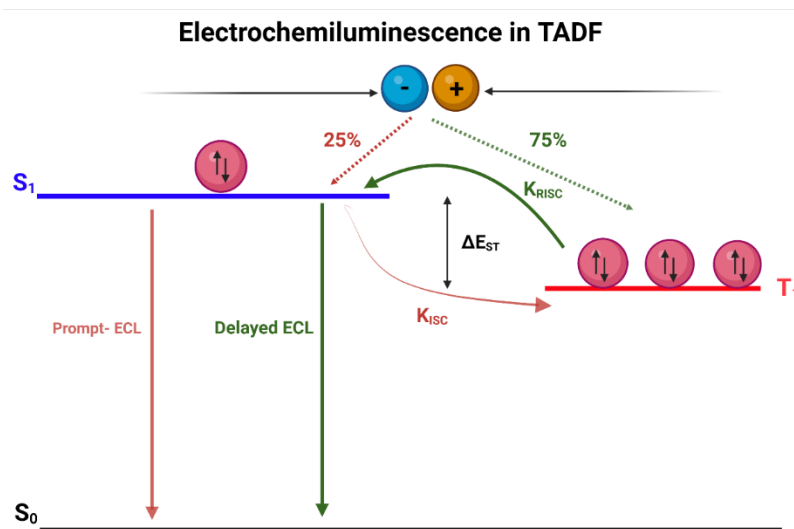


**Figure 1.6:** Electrochemiluminescence mechanism of TADFs.

However, as typical metal-free luminophores, TADF emitters could be utilized for conventional fluorescence imaging in different biological systems [130]. Meanwhile, the long-lived emission feature renders the TADF materials fluorescence lifetime imaging or time-resolved luminescence imaging capability, which could eliminate the interference of background signals and improve the accuracy in bioimaging [90]. Moreover, the TADF phenomenon originates from the RISC process, which is highly sensitive to both thermal energy and oxygen concentration, such characters could be applied to temperature and oxygen sensing[91]. Beyond these, the TADF

molecules with small  $\Delta E_{ST}$  and efficient intersystem-crossing (ISC) process could also be used as novel metal-free photosensitizers for photodynamic therapy. This is because that along with the excited triplet state ( $T_1$ ) decays back to the excited singlet state ( $S_1$ ), energy could be transferred to the surrounding oxygen leading to the reactive singlet oxygen ( $^1O_2$ ) generation for PDT [87],[92–94].

In this chapter in collaboration with Prof. PG Cozzi (University of Bologna) we investigate the electrochemical and electrochemiluminescence features of the TADFs which are presented in figure 1.7.

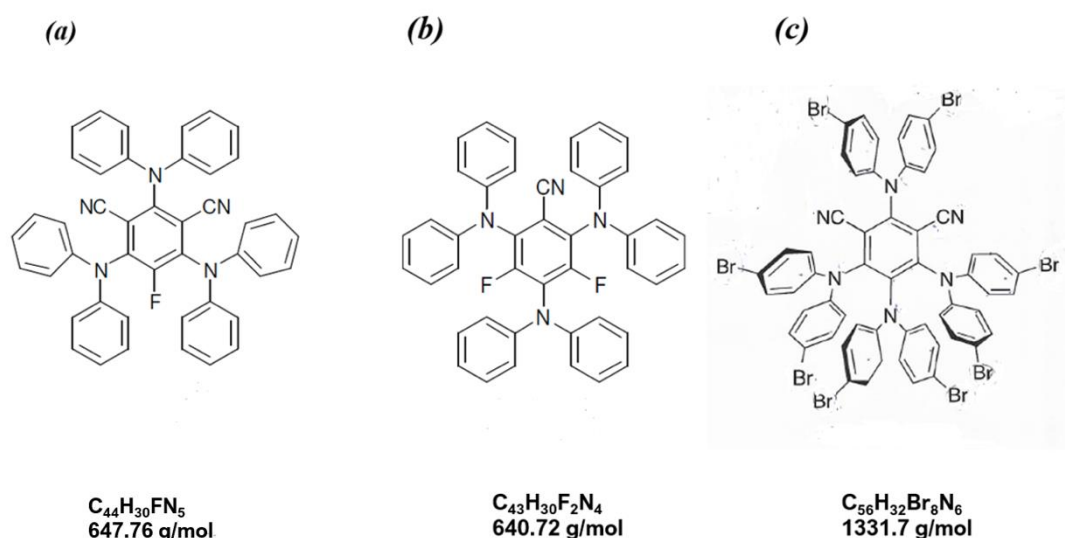


Figure 1.7: TADF molecule structures.

### 1.1.5 Metal-free Boron-dipyrromethene based luminophores

Among the numerous classes of highly fluorescent dyes, the set based on 4,4-difluoro-4-bora-3a,4a-diaza-s-indacene (BODIPY, difluoroboron *dipyrromethene*, Figure 1.8 shows perhaps the highest potential and has spectacularly risen in popularity. Although the first member of this set was reported as early as 1968 by Treibs and Kreuzer[131], the possible uses of BODIPY-based dyes for biological labeling, for electroluminescent devices, as tunable laser dyes, as potential candidates for solid-state solar concentrators, as fluorescent switches, and fluorophores in sensors and labels were fully recognized only since the mid-1990s. As a result, since then the number of research papers and patents has increased spectacularly as more researchers enter the field. The many excellent features of BODIPY can explain its ever-growing success. The robustness against light and chemicals, the relatively high molar absorption coefficients  $\epsilon(\lambda)$  and fluorescence quantum yields  $\Phi$ , negligible triplet-state formation, narrow emission bandwidths with high peak intensities, good solubility, resistance towards self-aggregation in solution, excitation/emission wavelengths in the visible spectral region ( $\geq 500$  nm), and fluorescence lifetimes  $\tau$  in

the nanosecond range all contribute to the appeal of these interesting compounds. Moreover, their spectroscopic and photophysical properties can be fine-tuned by attachment of ancillary residues at the appropriate positions of the difluoroboron dipyrromethene core. The wide versatility of synthetic pathways to the BODIPY class of fluorophores allows the creation of a perfect fit between the structure of the dye and its desired spectroscopic and photophysical characteristics.

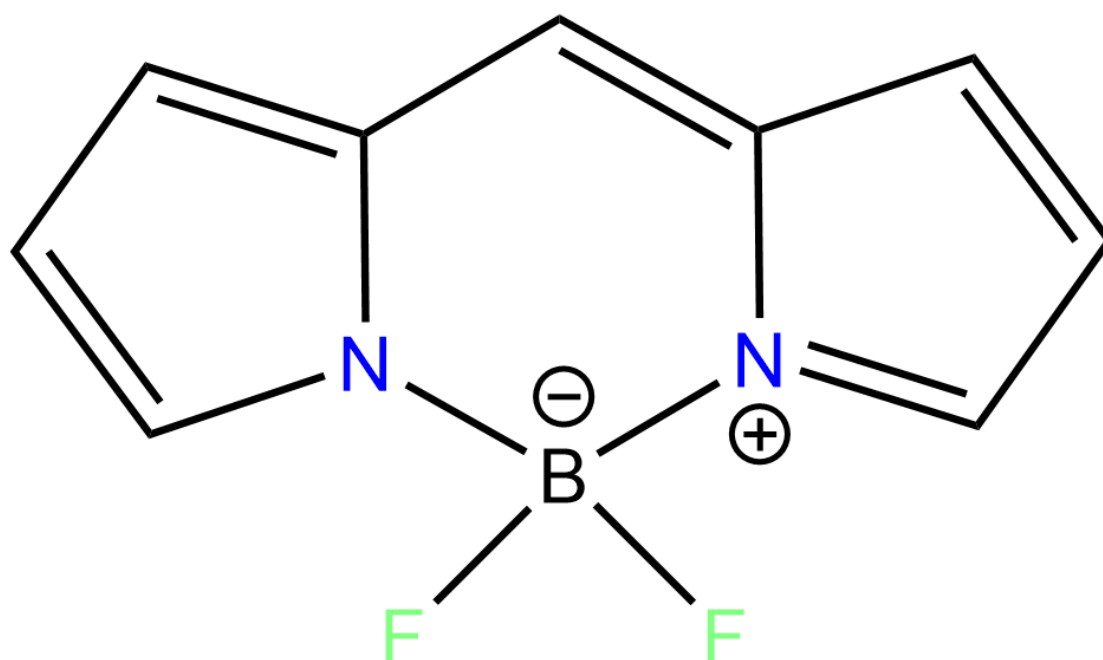
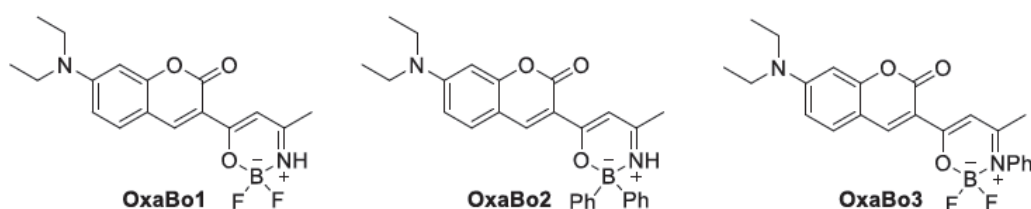


Figure 1.8: BODIPY structure.

Among organic molecules, boron-dipyrromethene (BODIPY) dyes emerged as highly efficient ECL emitters. Bard and co-workers pioneered reported the ECL propriety of various BODIPY derivatives[95]. BODIPY are a versatile class of luminophores with high fluorescence quantum yields in the visible spectral region and their photophysical properties could be easily modify by tuning the ECL emission wavelength and efficiency [96],[97].In addition BODIPYs were successfully modified, by Foster and coworker, introducing donor/acceptor groups so as to tune the emission wavelength and increase the Stokes Shift[98–100] .Another important class of fluorophores are tetra-coordinated six-membered boron compounds with O–B–N moiety, also called oxazaborines [101]. These compounds have interesting luminescent properties such as aggregation-induced emission (AIE). Recently TADF for a number of these compounds was described [102],[103].

Based on these attractive properties, BODIPY derivatives have found utility as laser dyes[104], photosensitizers [105],[106] fluorescent labels for in vivo imaging [107],[108] and in optical devices[109]. The electrochemical and ECL properties of BODIPY derivatives are also of note, as these compounds often display reversible redox behavior in aprotic solvents and excellent stability upon oxidation or reduction. These attractive electrochemical properties, coupled with robust and tunable

photophysics, distinguish BODIPY derivatives as excellent candidates for ECL applications [110],[95]. A number of electrochemical [111],[112] and ECL studies [110,113,114] of BODIPY dyes have been reported. In a recent study, A. Bard et. al. described the electrochemical, photophysical, and ECL properties of a 2,2'-bipyridine-BODIPY derivative (BB2), in which the meso-position of two fully substituted BODIPY moieties were linked directly to a 2,2'-bipyridine (bpy) spacer at the 4- and 4'-positions[115] . This BODIPY-appended bipyridine derivative was highly fluorescent and produced strong ECL emission in the presence of a coreactant. In this chapter we are going to investigate the electrochemiluminescence response of the following BODIPYs molecules names as OxazaBorines (OxaBo) in aprotic conditions based on the annihilation mechanism.



**Figure 1.9:** Structure of BODIPYs (OxaBo1-3).

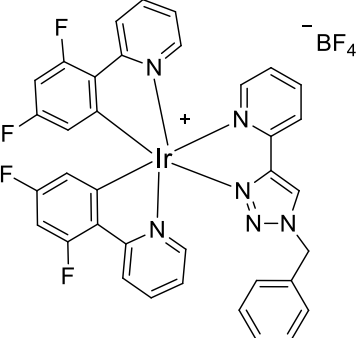
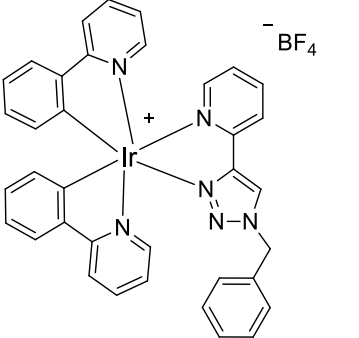
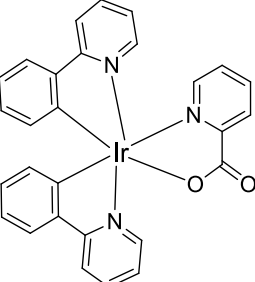
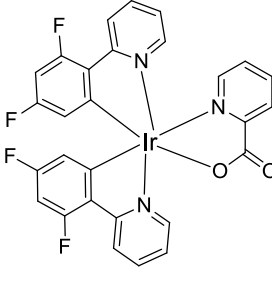
In collaboration with Prof. T. Mikysek (University of Pardubice Studentska) we study the coumarin-oxazaborine moiety to be directly joined through carbon-carbon bond and form donor–acceptor (D-A) chromophores **OxaBo** with 7-aminocoumarin donor and oxazaborine acceptor (Figure 1.9). That arrangement can substantially change the electron distribution as well as photophysical, electrochemical and ECL properties with a strong effect on the final quantum yield.

## 1.2 Iridium dyes in aprotic conditions

In this section four different iridium based luminophores will be investigated, in which two of them own a charge ligand due to the L= o-tolylazopyridine (tazpy) presence; the rest of them own a picolinate (pic) ligand occupying a C^N pair of ligand. As main ligands (C^N), the anions of 2-phenylpyridine (ppy), and 2-(2,4-difluorophenyl)pyridine (F2-ppy) were chelated to the iridium center. We expect that the relative energy levels of the main and ancillary ligands in the complexes could lead to emission of color tuning and luminous efficiency improvement by possible inter-ligand energy transfer. The table T1.1 presents the structures of iridium complexes, in which the investigation will occur in aprotic solvent. As solvent, the use of acetonitrile (AcN) increases the solubility of iridium complexes. To do so, an electrochemical cell with three electrodes: Pt wire (counter electrode), Ag wire (pseudo-reference electrode) and a Pt 2mm disc (working electrode) has been used. These three-

electrode system were put in a one-compartment air light cell, with high-vacuum O-rings and glass stopcocks. After the clean of the electrochemical cell, a volume of 4mL of AcN was used in every measurement in RT conditions, without the presence of oxygen, and the concentration of each iridium molecule remains constant (0.5mM). However, as supporting electrolyte was used a 0.1M tetrabutylammonium hexafluorophosphate (TBAH). After the preparation of electrochemical cell, it was placed in a dark box in front of a photomultiplier (PMT) tube which was used for the detection of the light emission. For every electrochemical measurement a Biologic® potentiostat was used for the potential application.

**Table T1.1:** Iridium complexes.

<p>[Ir(F2ppy)<sub>2</sub>tazpy]BF<sub>4</sub> AB141</p>  <p><math>C_{36}H_{24}BF_8IrN_6</math> Molecular Weight: 895.63</p>	<p>[Ir(ppy)<sub>2</sub>tazpy]BF<sub>4</sub> AB148</p>  <p><math>C_{36}H_{28}BF_4IrN_6</math> Molecular Weight: 823.67</p>
<p>[Ir(ppy)<sub>2</sub>pic] MPP04</p>  <p><math>C_{28}H_{20}IrN_3O_2</math> Molecular Weight: 622.69</p>	<p>[Ir(F2ppy)<sub>2</sub>pic] (=Firpic) MPP03</p>  <p><math>C_{28}H_{20}IrF_4N_3O_2</math> Molecular Weight: 658.69</p>

### 1.2.1 Electrochemical characterization for the iridium complexes

First, a cyclic voltammetry (CV) experiment was performed for the investigation of the redox window of all iridium complexes. The metallic center of these complexes can be easily oxidized from (III) to (II); on the other hand, a possible reduction may be observed due to the nature of the C<sup>N</sup> ligands. In figure 1.10a-d is presented the electrochemical voltammograms of each complex.

In positive potential (oxidation), it is presented a fully reversible oxidation of each complex. In negative potentials, a reduction peak is observed because of the C<sup>N</sup> ligands in different potential ranges; thus, not always the reduction process is reversible. This irreversible anodic wave is attributed to a small amount of complex decomposition (except the figure 1.10 c) that can occur under highly negative applied potentials. In the case of AB141, the peak-to-peak separation ( $E_{1/2}$ ) results at +1.45V for the oxidation and -1.15V for reduction, however the  $E_{1/2ox} - E_{1/2red}$  results at 2.6V. Although, for the AB148, the only difference with the previous complex is the elimination of the four fluorine atoms from the amidic rings.

This elimination makes the AB 148 owing a quasi-reversible oxidation in contrast of the previous complex. On the other hand, the reduction remains a non-reversible process, while the potential range and the  $\Delta E_{1/2}$  was decreased. The reduction  $E_{1/2red}$  occurs at -1.5V; thus, the oxidation  $E_{1/2ox}$  occurs at +1.45V at the same potential as AB141. However, the  $\Delta E_{1/2}$  is totally depended on the presence of fluorine, in this case it results at 2.95V (table T1.2), where the potential window is much larger than the previous case.

Picolinate ligand (abbreviated as pic) is known to bind to metal ions as a bidentate N,O-donor forming a stable five-membered chelate ring. It is interesting to note that the two donor sites of the picolinate ligand are of a significant different nature. The pyridine nitrogen is a soft donor and a recognized stabilizer of the lower oxidation states of transition metals, whereas the carboxylate oxygen is a hard donor and is known to stabilize transition metals in their higher oxidation states. Hence, coordination of iridium by the picolinate ligand may be expected to have an interesting effect on the redox properties of the complexes.

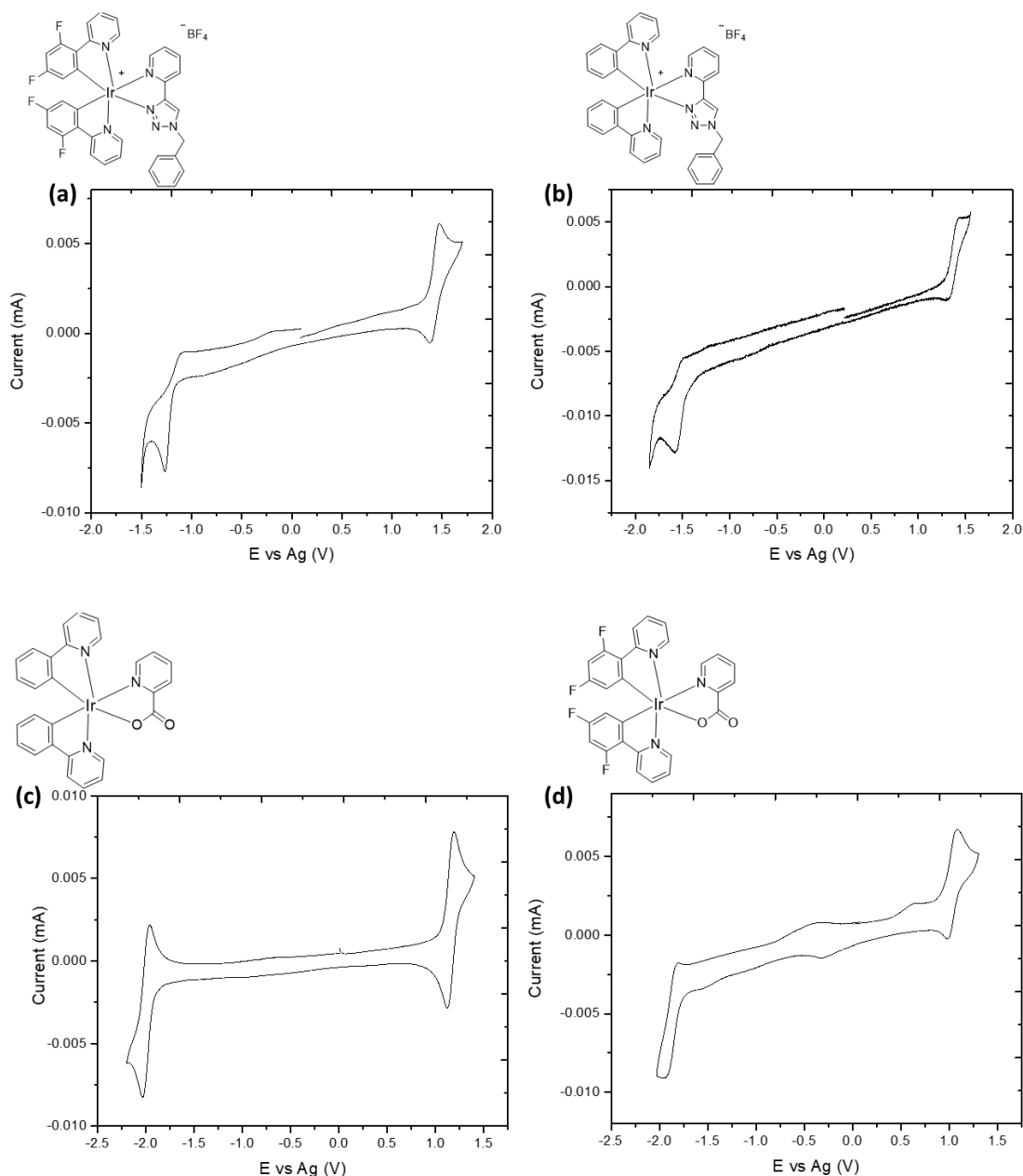


**Figure 1.10:** Cyclic voltammetry of 0.5mM compound of (a) AB141, (b) AB148, (c) MPP04 and (d) MPP03; Scan rate 100mV/s in CH<sub>3</sub>CN/TBAH (0.1M). Working electrode: Pt disk (2mm diameter) vs Ag electrode.

In fact, the complex MPP04 contains two ligands of ppy and one pic. As it is described above, pic stabilizes the oxidation part of the molecules. Thus, according to the figure 1.10 the oxidation process of the MPP04 occurs at +1.15V and it is totally reversible. In comparison with the two previous complexes, MPP04 can be oxidized in a lower potential according to pic ligand theory. Moreover, the reduction occurs at -2.01V and it is a reversible process. The  $E_{1/2ox} - E_{1/2red}$  ensue at 3.15V which indicates a large potential window, perhaps this difference from the complexes AB141,148 is an effect of the ligand's substitution. Figure 1.10 (d) shows the electrochemical signal during a CV process of MPP03. The oxidation region occurs at +1.1V and it is totally reversible,



due to the oxidation in the metal center of the dye. Contrastingly, the reduction peak is presented in negative potential at -1.9V, which is more negative than the case of AB148 complex. Not only the redox behavior of the MPP03 is observed but also some small anodic and cathodic peaks at negative potentials, specifically at -0.4V. This could happen due to the possible impurities of the material or/and of the presence of water traces. All the electrochemical features are presented in the table T1.2.

**Table T1.2:** Electrochemical features of iridium complexes

Compound	E <sub>1/2</sub> (red) vs Ag (V)	E <sub>1/2</sub> (ox1) vs Ag (V)	E <sub>ox1</sub> -E <sub>red</sub> vs Ag (V)
AB141	-1.15	1.45	2.60
AB148	-1.50	1.45	2.95
MPP03	-1.55	1.11	2.66
MPP04	-2.00	1.15	3.15

### 1.2.2 Electrochemiluminescence features of Iridium complexes

Owing the redox potential of each compound, a chronoamperometric experiment performed in combination with the detection of the light emission. This family of compounds follow the annihilation mechanism as it was mentioned on the introduction part. Examining the figure 1.11 a-d and calculating the integrates of current and ECL intensity of each complex, instead of absolute measurements, we can easily calculate the ECL efficiency. ECL research often reports emissions relative to Ru(bpy)<sub>3</sub><sup>2+</sup> in the following equation:

$$\Phi_{\text{ECLx}} = \Phi_{\text{ECLst}} \times \frac{\int \text{ECLx}}{\int \text{ECLst}} \times \frac{\int Q_{\text{st}}}{\int Q_{\text{x}}} \quad (\text{Eq 1}) [116]$$

with integrated ECL emissions (ECL) and integrated current or charge (Q) that flows into the cell. Single values instead of calibration plots are generally reported for  $\Phi_{\text{ECL}}$ , relative ECL efficiencies do not have standard solutions, standard concentrations, or standard coreactant concentrations.  $\Phi_{\text{ECLst}}$  is almost always Ru(bpy)<sub>3</sub><sup>2+</sup> ECL emissions taken as 5%, regardless of variations in concentrations, differences in testing conditions or discrepancies in solution polarity. This 5% quantum efficiency value measured in 1973 by the Bard research group also used a rotating ring-disk electrode (RRDE) at 52 revolutions per second in a concentration of 1 mM Ru(bpy)<sub>3</sub><sup>2+</sup> solution in the annihilation pathway [117].

According to the Eq1, the ECL efficiency of each iridium complex is presented in the Table T1.2.

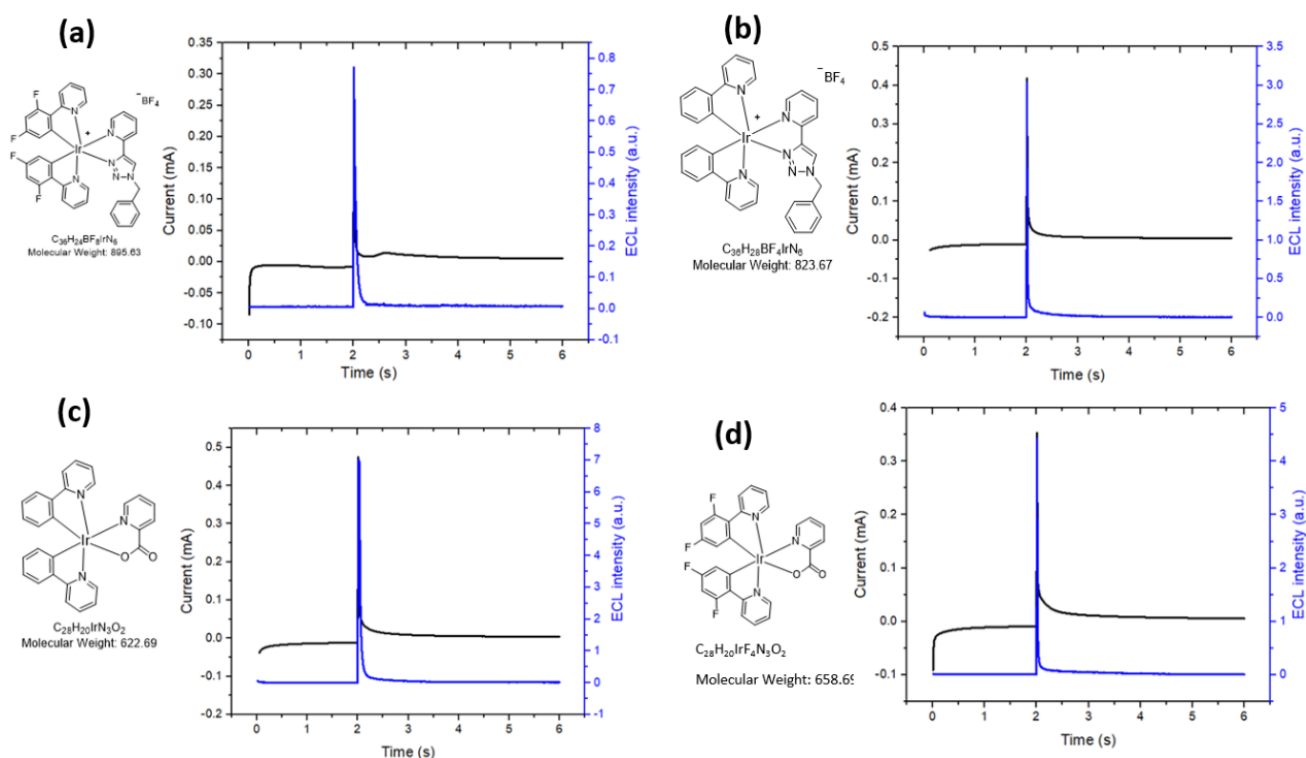


**Figure 1.11:** ECL intensity registered during a chronoamperometric measurement of 0.5mM compound of AB141, AB148, MPP04 and MPP03; Amplification 00 $\mu$ A. Solvent: CH<sub>3</sub>CN/TBAH (0.1M). Working electrode: Pt disk (2mm diameter) vs Ag electrode. PMT 750V.

According to the chronoamperometric analysis (figure 1.11b) and the equation (Eq1), the efficiency of the AB148 complex can be easily calculated. In such case the obtaining efficiency  $\Phi_{ECL}$  is 2% higher than the efficiency of AB141. Finally, this difference can be easily observed comparing the two chronoamperometric figures AB141 and AB148 figure 1.11a,b, in which the second case of the decay of ECL intensity line is much slower than the first time and its value is higher.

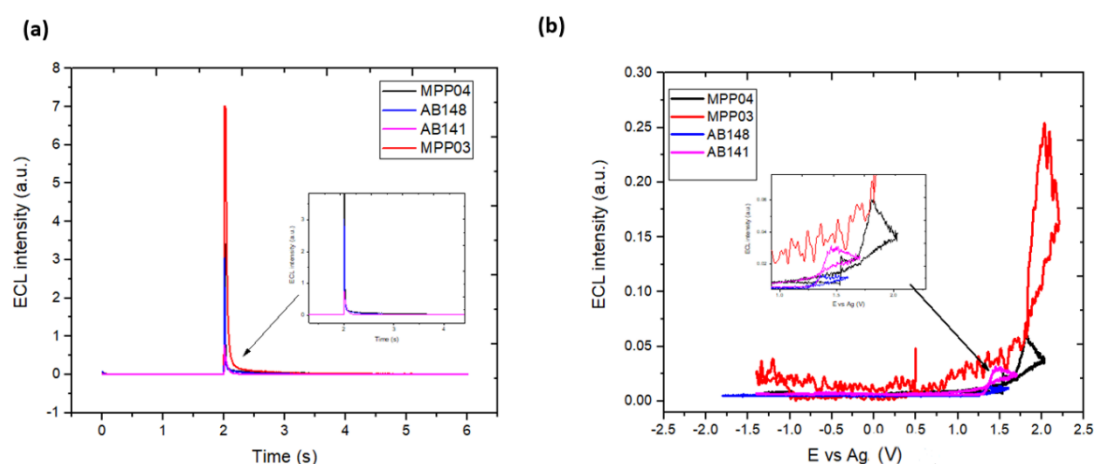
Consequently, the investigation of the MPP04 and MPP03 was performed, in which results a substitution of the tazpy to the pic ligand. In this case a higher ECL intensity and a better stability is expected than the AB148 and AB141 complexes. Indeed, the ECL response owns a high signal of 7 a.u. and 4.5 a.u., respectively. In the figure 1.11c,d is presented a slower ECL decay in contrast to the figure 1.11a,b, which means that we expect a higher ECL efficiency value. Indeed, using the equation Eq1, the  $\Phi_{ECL}$  is 8.8% and 6.8% for MPP04 and MPP03, respectively. All ECL efficiencies are presented in the table T1.3.

**Table T1.3:** ECL efficiency for iridium complexes

Complex	$\Phi_{\text{ECL}}$ (%)
AB141	0.5
AB148	2
MPP03	6.8
MPP04	8

### 1.2.3 Comparison among Iridium complexes

In a way of having a better comparison of iridium complexes more CV experiments registering the ECL intensity have been performed using a lower amplification.



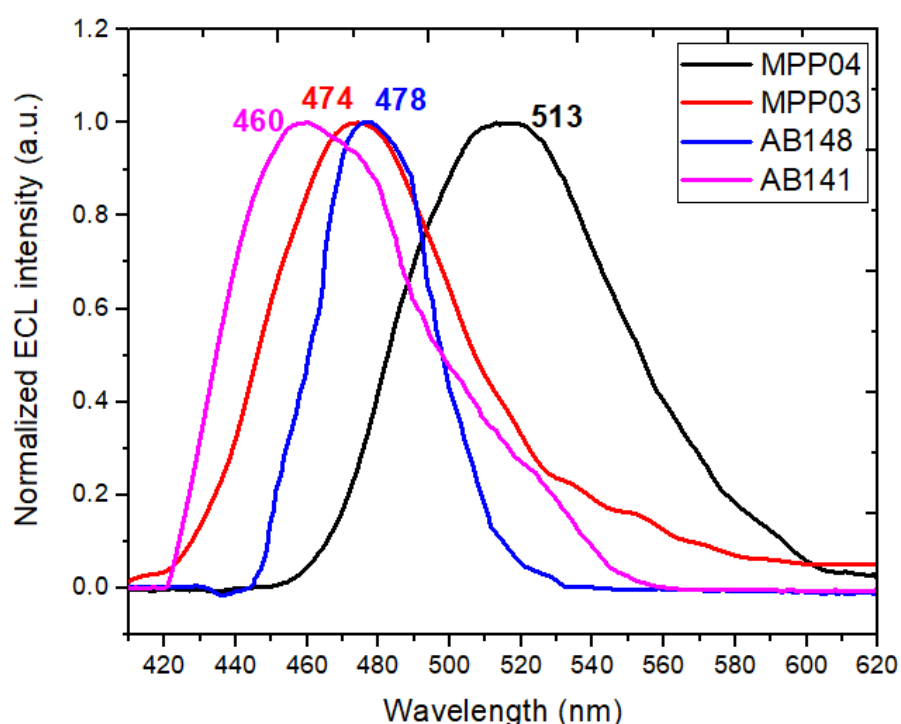
**Figure 1.12:** (a) ECL intensity registered during a chronoamperometric measurement of 0.5mM compound of AB141, AB148, MPP04 and MPP03; Amplification 00.0 $\mu$ A. (b) ECL intensity registered during a cyclic voltammetry measurement of 0.5mM compound of AB141, AB148, MPP04 and MPP03. Solvent: CH<sub>3</sub>CN/TBAH (0.1M). Working electrode: Pt disk (2mm diameter) vs Ag electrode. PMT 750V; Amplification 0 $\mu$ A.

Figure 1.12a demonstrates the comparison of ECL intensity during the previous chronoamperometric process. The iridium complex MPP03 presents the highest ECL intensity and in meanwhile the slowest decay, which indicates a longer lifetime. According to that, an intense ECL signal, well-distinguishable from the background, was recorded during several successive potentials scans without any significant decrease of the emitted light. Such is presented in the figure 1.12b, MPP03 obtains

the highest ECL intensity, which gives out positive potentials during a CV process. To do so, a lower amplification was used during the process.

The ECL emission was intense and stable enough to allow recording of the ECL spectrum reported in Figure 1.13. When the potential was repeatedly pulsed from 0 V to values between  $E_{ox}$  and  $E_{red}$  (V) depending on the complex, light emanated from the electrode surface, with brightness and color depending on the applied potential.

Substitution of the phenyl hydrogens with electron-withdrawing fluorinated atoms, particularly on the 4'- and 6'-positions, stabilizes the HOMO (the highest occupied molecular orbital) more than the LUMO (the lowest unoccupied molecular orbital), leading to an increased energy gap. Therefore, by replacing ppy with F2-ppy as a ligand, hypsochromic shifted emissions were observed.



**Figure 1.13:** Normalized ECL intensity vs Wavelength of 0.5mM AB141, AB148, MPP03 and MPP04 in  $CH_3CN/TBAH$  0.1M. Working electrode: Pt disk (2mm diameter) vs Ag electrode. PMT bias of 750V; integration time 100s; step 2nm.

**Table 1.4:** ECL spectrum for iridium complexes

Complex	$\lambda_{ecl}$ (nm)
AB141	460
AB148	478
MPP03	474
MPP04	513

The observed blue emissions from the fluorine-based ligands (F2ppy) complexes AB141 and MPP03 are remarkable since, as mentioned above, decorating the C<sup>N</sup> ligands with F or fluorinated groups is a common strategy to blue-shift the emission of this type of complex. The influence of the pyridinium fragment located para to the cyclometalating carbon is clearly shown by comparing the emission properties. On the other hand, when C<sup>N</sup> is deprotonated 2-phenylpyridine (ppy), the emission in I is red-shifted strongly.

In general, the compounds MPP04 and AB148 obtain a red-shift emission cause of the absence of F on the amidic ring, owing the emission wavelength at 513nm and 478nm, respectively. On the other hand, the complexes AB141 and MPP03 obtain a blue-shift with an ECL intensity at 460nm and 474nm, respectively (Table T1.4).

### **1.3 Ru[(1,10-phenanthroline)<sub>2</sub>dipyrido[3,2-a:2',3'-c]phenazine]<sup>2+</sup> complex dye in aprotic conditions**

Ru–dppz (dppz = dipyrido[3,2-*a*:2',3'-*c*]phenazine) complexes have an important role as environmental sensitive luminescence sensors and building blocks for larger supramolecular compounds. Their photophysical properties are known to be highly sensitive to intermolecular solvent–solute interactions and solvent bulk-properties. Ruthenium polypyridine complexes are interesting in building blocks for supramolecular architectures because they are chemically very stable, redox active and display a rich photochemistry.

Electrochemical data were obtained by cyclic voltammetry using a conventional single-compartment three-electrode cell arrangement in combination with a potentiostat “Biologic®”. As working electrode a 2mm Pt disk, as a counter electrode a platinum wire and as reference electrode an Ag/AgCl wire, were used. The measurements were carried out in anhydrous and Argon purged with 0.1 M tertbutylammonium tetrafluoroborate (TBAH) as supporting electrolyte.

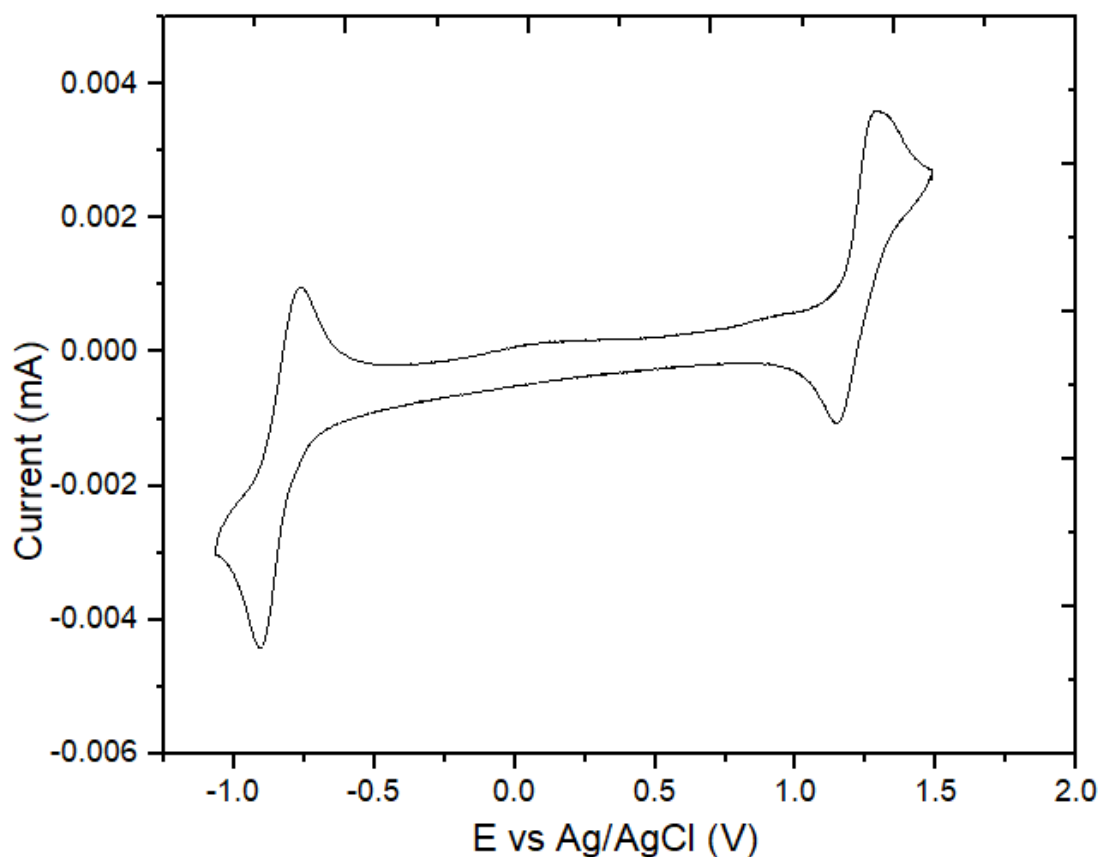


**Figure 1.14:** Cyclic voltammetry of 0.5mM Ru[(phen)<sub>2</sub>dppz]<sup>+2</sup>; Scan rate 100mV/s ) in CH<sub>3</sub>CN/TBAH (0.1M). Working electrode: Pt disk (2mm diameter) vs Ag/AgCl electrode.

In figure 1.14 the cyclic voltammogram of Ru-dppz is consistent with metal-based reversible oxidation and several ligand-based reduction steps. Oxidation of the Ru center is observed at +1.2 V vs Ag/AgCl electrode, and the ligand-based reduction step of the phen moiety of dppz is located at -0.88 V without any interference of the electron-withdrawing ability.

Furthermore, the oxidation (Ru(II)/Ru(I)) process reflects an increase of the electron-accepting properties of the  $\pi$ -extended ligand. The Ru-dppz molecules obtains a  $E_{1/2}$  equal to 1.04V. After the electrochemical characterization, the ECL efficiency of the Ru-dppz complex has been calculated via amperometric measurement.

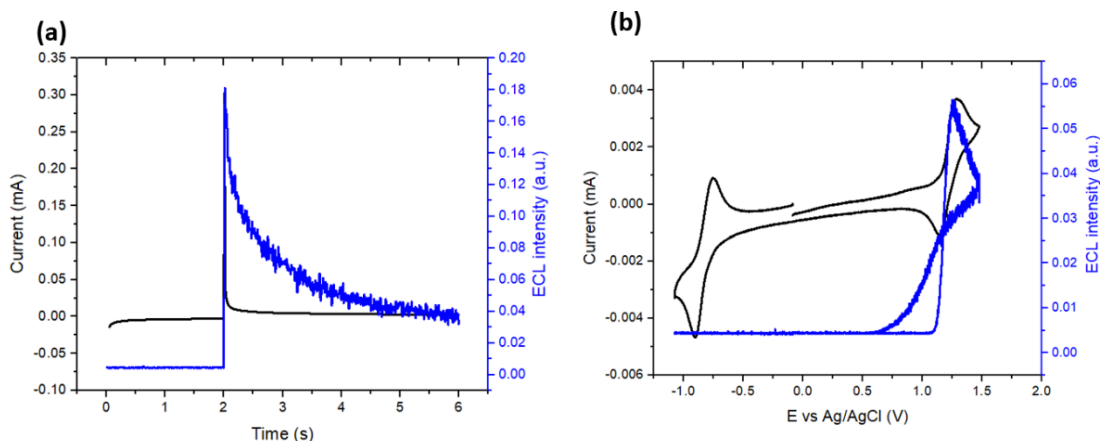


**Figure 1.15:** (a) ECL intensity registered during a chronoamperometric measurement of 0.5mM compound of  $\text{Ru}[(\text{phen})_2\text{dppz}]^{2+}$ ; (b) ECL intensity registered during a cyclic voltammetry measurement of 0.5mM  $\text{Ru}[(\text{phen})_2\text{dppz}]^{2+}$ . Solvent:  $\text{CH}_3\text{CN}/\text{TBAH}$  (0.1M). Working electrode: Pt disk (2mm diameter) vs Ag electrode. PMT 750V; Amplification  $00\mu\text{A}$ ; Scan Rate 100mV/s

The ECL efficiency can be meticulously calculated by the annihilation method and achieved by chronoamperometric techniques (figure 1.15 a) using the equation Eq1 of the section 2.2. In such case the  $\Phi_{\text{ECL}}$  efficiency results at 0.05% which is much lower than the iridium complexes in the previous chapter. In figure 1.15b is exhibiting the registration of ECL intensity during a CV process. In blue line is presenting the ECL intensity which occurs at +0.6V with a peak value of 0.055a.u.

## 1.4 Electrochemical and Electrochemiluminescence features of Thermally Activated Delayed Fluorescence Materials in aprotic conditions

As recent reports highlight the options to tailor certain organic dye classes for specific catalytic purposes [118],[119], providing either strongly oxidizing or powerful reducing properties, we accordingly questioned whether we could develop tuning guidelines to access broadly applicable, purely organic photocatalysts reaching both high oxidation and reduction potentials from a single, common scaffold. Prompted by the essential importance of having spatially separated HOMO and LUMO in a non-overlapping frontier molecular orbital (FMO) structure for the construction of thermally activated delayed fluorescence OLED emitters (TADF OLEDs)[120], and the initial proof of concept for their photocatalytic activity [121], we reasoned the intrinsic charge transfer processes in such TADF materials to be a suitable starting point for our investigations (Figure 1.16).

A1,A2:Acceptor (CN, Halogen)  
D: Donor

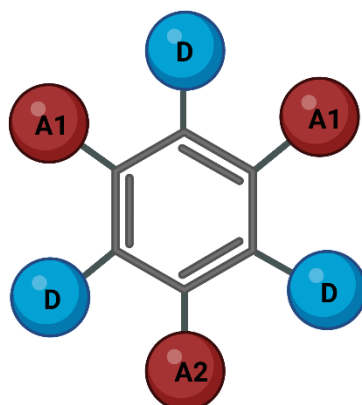


**Figure 1.16:** General structure of TADF.

Using cyanobenzenes as relatively strong acceptor moieties, we opted to:

(i) combine them with rather weak carbazole and diphenylamine derivatives as corresponding donors and additionally,

(ii) modify the aromatic acceptor core unit by targeted interchange of the cyano-groups with alternative (electron-withdrawing) substituents to thereby

(iii) gain a profound understanding of such unprecedented core modifications and their additional and interconnecting effects on the redox properties of the corresponding catalyst derivatives.

#### 1.4.1 Electrochemical characterization of TADF

The TADF's structure which are going to be investigated are represented in figure 1.7. Apart from accessing longer excited state lifetimes, we centered our effort on derivatives that could provide a wide redox window allowing a broad range of both reduction and oxidation processes, referring to the great success and versatile applicability of  $\text{Ru}(\text{bpy})_3^{2+}$ .



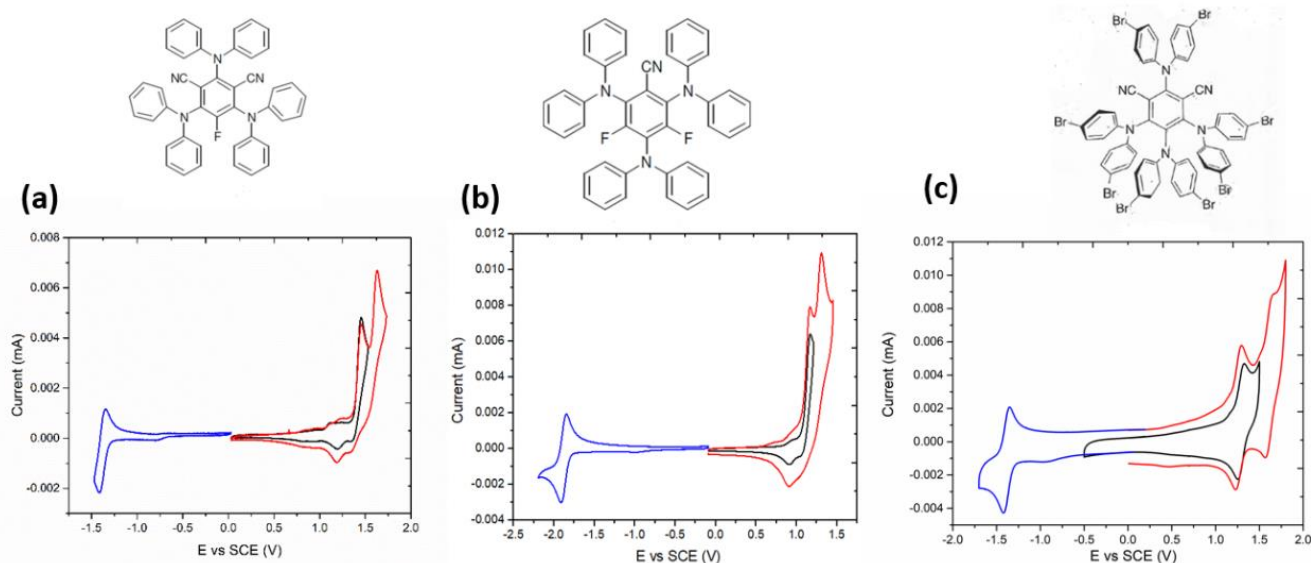


**Figure 1.17:** Cyclic voltammetry of 0.5mM (a) 3DPAFIPN (b) 3DPA2FBN (c) 4DPA2BrIPN; Scan rate 100mV/s in I/TBAH (0.1M). Working electrode: Pt disk (2mm diameter) vs SCE electrode.

In general, there are two different ligands of the TADF luminophores: (1) a donor-based effect which would lead to increased reducing power upon rising donor strength and/or number, as well as (2) an acceptor core where both number and kind withdrawing substituents (CN, Cl, F, ecc) matter to increase the oxidation potential. Respecting, the special nature of fluorine as  $\sigma$ -acceptor, but at the same time as a  $\pi$ -donor substituent, adds on further influence on the core substitution of the reduction potential that could lead to special interest of reaching more exceptional potentials. The acceptor core's strong electron withdrawing ability can be rationally enhanced by the attached donors (according to their strength) allowing for a significant contribution to further tune the oxidation potential.

In addition, figure 1.17 shows the cyclic voltammetry of (a) 3 diphenylamine 5-fluoro isophthalonitrile (**3DPAFIPN**) (b) 3 diphenylamine 3,5-difluoro benzonitrile (**3DPA2FBN**) (c) 4 diphenylamine 3,5 dibromuro isophthalonitrile (**4DPA2BrIPN**). The black line represents the first oxidation part, the red line two oxidations anodic peaks; thus the blue one is the reduction of each TADF molecule in 100mV/s of scan rate. Each TADF molecule presents different oxidation/reduction potential due to the different donors. Interestingly, interchanging fluorine and bromide as core substituents at the central benzene in the first case and as additional molecules in the diphenylamine ring (**3DPAFIPN** and **4DPA2BrIPN**) does not show any difference in the observed oxidation/reduction potential. Possibly, electro withdrawing inductive effects are counterbalanced by size dependent mesomeric effects [122–124].

On the other hand, **3DPA2FIPN** shows a more negative reduction potentials (-1.8V) where a weak acceptor core may be fundamental to an enhanced delocalization of the "hole" by improved interaction with the  $\pi$ -conjugated donor moieties. Additionally, the 2-fold fluorine substitution may beneficially contribute to further increase the electron density according to fluorine's well established electron donating ability (\*M). This special fluorine effect becomes more apparent in the direct comparison of the

two halogen substituted isophthalonitrile derivatives where fluorine clearly increases the reduction power.

Consequently, the substitution of a CN ligand to another fluorine ligand, give us a higher redox  $E_{1/2}$  value which, in this case is 2.92V, as shown in figure 1.17b. These high values offer, besides, the high ground state redox potential (TADF/TADF<sup>-</sup>) and (TADF/TADF<sup>+</sup>) as function of the donor-acceptor properties, an additional strong excited state redox potential (TADF<sup>\*</sup>/TADF<sup>-</sup>) and (TADF<sup>\*</sup>/TADF<sup>+</sup>). All the characteristic potentials for this redox process are presented in the table below T1.4.

**Table 1.4:** Electrochemical features for TADF complexes

Compound	$E_{1/2}(\text{red})$ vs SCE (V)	$E_{1/2}(\text{ox1})$ vs SCE (V)	$E_{1/2}(\text{ox2})$ vs SCE (V)	$E_{\text{ox1}}-E_{\text{red}}$ vs SCE (V)
3DPA_2F_Bn	-1.87	1.05	1.12	2.92
3DPAFIPN	-1.39	1.32	1.48	2.71
4DPA_2Br_IPN	-1.55	1.11	1.46	2.66

### 1.4.2 ECL efficiency for TADF molecules

For the calculation of ECL efficiency, three individual experiments have been performed using a chronoamperometric technique such as it has been done for the calculation of ECL efficiency in the case of Iridium and Ruthenium complexes.

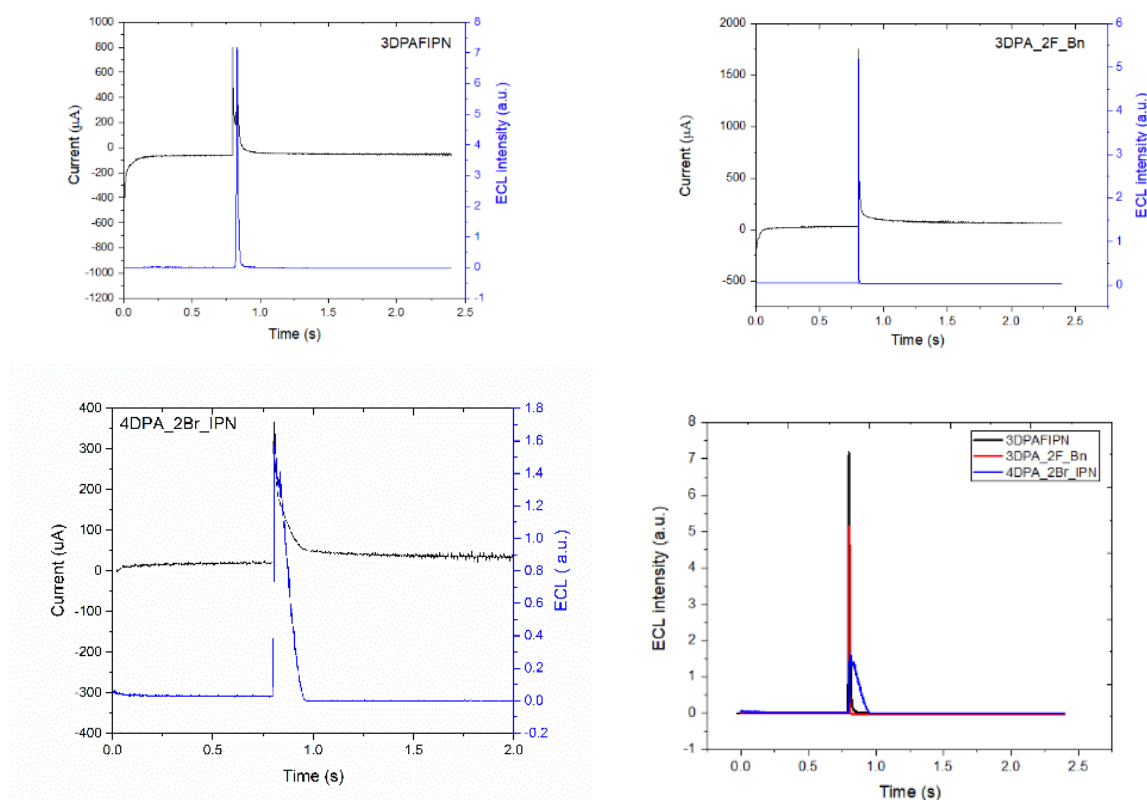


**Figure 1.18:** Current and Photocurrent intensity according to the time of each compound (0.5mM) in AcN/TBAH 0.1M. As WE is used a Pt disk electrode (2mm diameter) vs SCE electrode in duration step of 0.8s. Comparison diagram of ECL intensity versus time during chronoamperometric impulse. PMT bias of 750V; 00.0 $\mu$ A amplification.

Figure 1.18 presents the current and ECL intensity of each individual TADF complex and the comparison graph of ECL intensity. The highest ECL intensity value is presented by the **3DPAFIPN** (7a.u.), negligible differences are observed in comparison with **3DPA2FBN**. The substitution of one CN group with one fluorine may presents a lower ECL signal and a higher decay (comparison graph in red line). On the other hand, the lowest ECL intensity is presented by the **4DPA2BrIPN** but at the same time, the higher lifetime can verified by the comparison ECL intensity graph. We assumed that this behavior is a result of the presence of the bromide in the amidic rings. The bromide can stabilize the TADF molecule, which can be verified from the totally reversible oxidation peaks in the figure 1.17 c; thus, the lifetime of the excited state is increased.

According to that, the calculation of the  $\Phi_{ECL}$  is based on the equation Eq1 and the results are presented in the table T1.5.

**Table T1.5:** ECL features for TADF compounds

Compound	$\lambda_{ECLmax}$ (nm)	$\Phi_{Ecl}$ (%)
<b>3DPA_2F_Bn</b>	490	1.6
<b>3DPAFIPN</b>	530	2.3
<b>4DPA_2Br_IPN</b>	536	7.6

The **4DAP2BrIPN** exhibits the highest ECL efficiency than the rest of the TADFs as a result of the bromide presence. Between **3DPA2FBN** and **3DPAFIPN** there is no huge differences presented in ECL efficiency but on the other hand a great difference is shown in the blue-shift spectrum according to the presence of fluorine (figure 1.19), as it was described above.

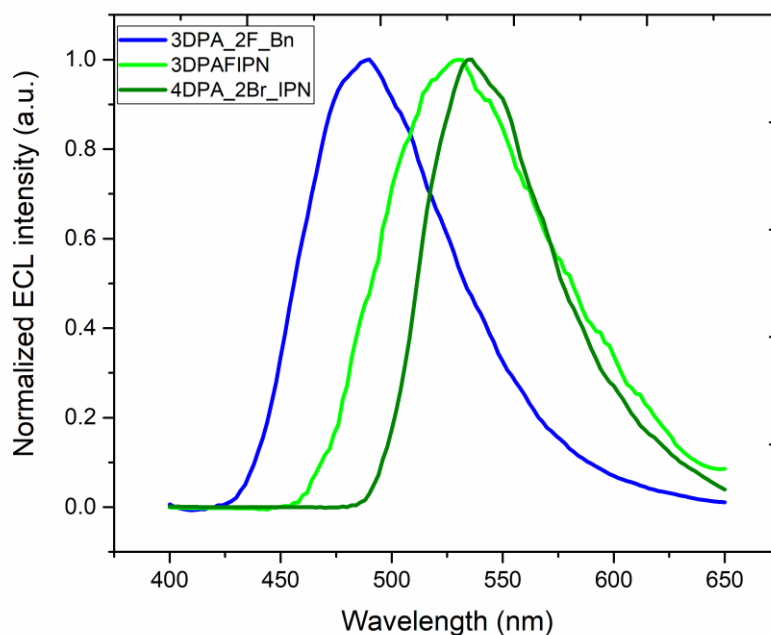


**Figure 1.19:** Normalized ECL intensity vs Wavelength of 0.5mM 3DPA\_2F\_Bn, 3DPAFIPN and 4DPA\_2Br\_IPN in CH<sub>3</sub>CN/TBAH 0.1M. Working electrode: Pt disk (2mm diameter) vs Ag electrode. PMT bias of 750V; integration time 100s; step 2nm.

## 1.5 Photophysical and Electrochemiluminescence of novel coumarin based oxazaborines

In this paragraph, the electrochemical photophysical and ECL property of this novel class of coumarin-based oxazaborines (compounds **OxaBo1**, **OxaBo2** and **OxaBo3** Figure 1.9) is outlined. They were synthesized and characterized in non-aqueous media in collaboration with Prof. T. Mikysek (University of Pardubice, Czech Republic). All these three novel compounds were analyzed in the same concentration and under the same conditions, in a way to be comparable with each other. Finally, the ECL properties and efficiencies of such compounds have been carried out in aprotic solvent.

### 1.5.1 Electrochemical characterization

The first oxidation of all studied compounds proceeds at potentials of +1.01 to +1.07 V (vs SCE) as one-electron reversible process except for compound **OxaBo2**, where the reversibility was observed at scan rate 8 V s<sup>-1</sup> and higher. The changes in substitution on oxazaborine core only negligibly influence first oxidation potential, hence when replacing both fluoro substituents by two phenyl groups it causes the shift of first oxidation potential by 60 mV to less positive values. On the other hand, the first

reduction of all three compounds proceeds at potentials of -1.24 to -1.43 V (vs SCE) as irreversible process (see Figure 1.20). Nevertheless, at higher scan rates ( $8 \text{ V s}^{-1}$ ) the first reduction changes to quasi-reversible process, this points to the fact that corresponding radical anion has low stability in acetonitrile.

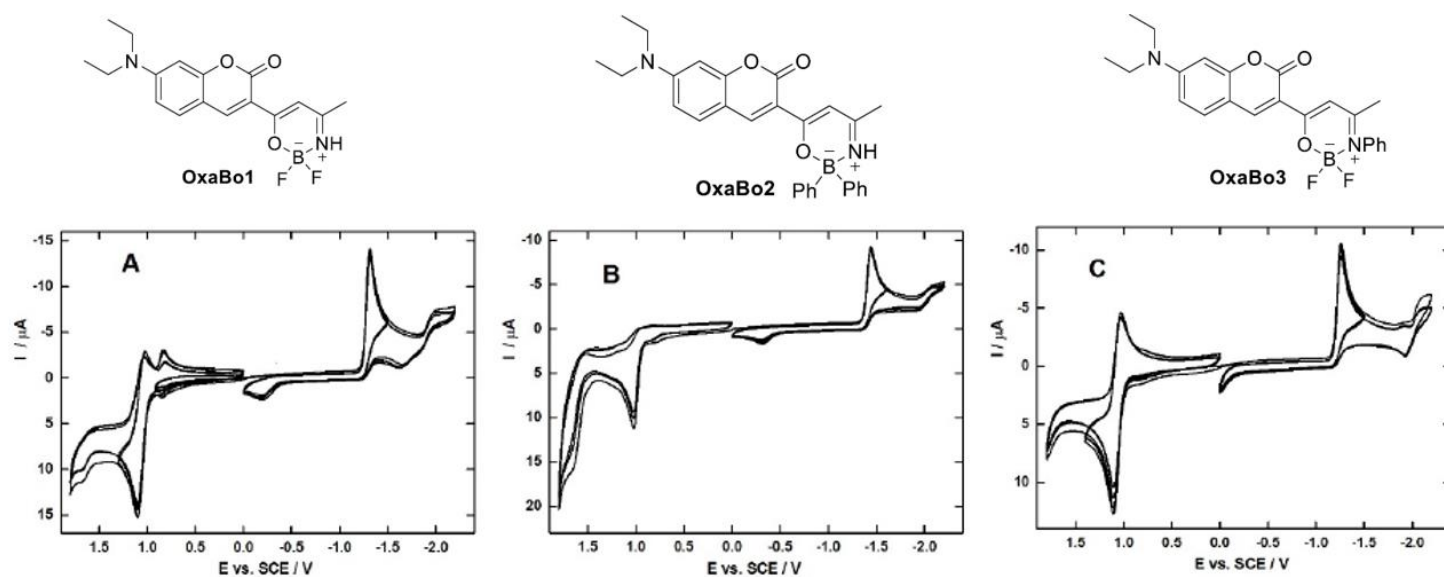


**Figure 1.20:** Electrochemical performance of **OxaBo 1-3** ( $5 \cdot 10^{-4} \text{ M}$ ) at glassy carbon electrode in AcN; scan rate  $\nu = 100 \text{ mV/s}$ .

Concerning different substitution on oxazaborine core, when comparing compounds **OxaBo1** and **OxaBo3** with compound **OxaBo2**, the shift of the first reduction potential by about 130-190 mV to fewer negative values due to presence of electron-withdrawing fluoro substituents can be observed. The easiest reduction process shows compound **OxaBo3**, where the role plays delocalization of electron density as results also from lowest value of first oxidation and reduction potential difference (see Table T1.6).

**Table T1.6:** Electrochemical features for OxaBo compounds

Compound	$E_{1/2}(\text{red})$ vs SCE (V)	$E_{1/2}(\text{ox1})$ vs SCE (V)	$E_{\text{ox}}-E_{\text{red}}$ vs SCE (V)
<b>OxaBo1</b>	-1.30	1.07	2.36
<b>OxaBo2</b>	-1.43	1.01	2.44
<b>OxaBo3</b>	-1.24	1.07	2.31

## 1.5.2 Photochemical properties

Fluorescence spectra for all compounds in this polar environment shows similar shape without strongly pronounced vibronic progressions suggesting intermolecular charge

transfer character of the transitions due to the presence of electron donating dimethylamine group. All the studied compounds show strong fluorescence in diluted solutions in acetonitrile with quantum yields around 70% and short fluorescence time constants 1.6–2.16 ns. Fluorescence spectra for all compounds in this polar environment shows similar shape without strongly pronounced vibronic progressions suggesting intermolecular charge transfer character of the transitions due to the presence of electron donating dimethylamine group[125].

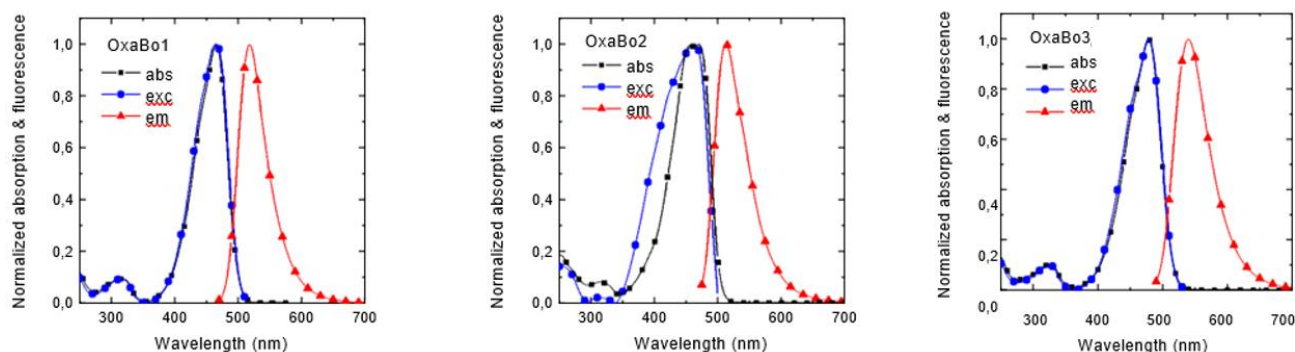


**Figure 1.21:** Normalized absorption (squares), fluorescence excitation (circles) and emission (triangles) of the studied coumarin-oxazaborine dyes OxaBo1, OxaBo2, OxaBo3.

Comparing compounds containing electron withdrawing fluorine atoms (**OxaBo1** and **3**), we can observe clear bathochromic shift in UV-Vis absorption and fluorescence excitation spectra (about 12 nm), and also in fluorescence emission (22 nm) induced by the presence of phenyl on the nitrogen atom. These shifts also translate to increased Stokes shift for **OxaBo3** (62 nm) compared to **OxaBo1** (53 nm) (figure 1.21). Considering the higher molar extinction coefficient of **OxaBo3** than **OxaBo1**, these results seem to indicate that the phenyl causes slightly increased intermolecular charge transfer character. An opposite behavior can be observed for compound **OxaBo2** where the fluorine atoms were replaced by phenyls. Comparing **OxaBo2** to the **OxaBo1**, a slight hypsochromic shift was observed for fluorescence excitation and also emission spectra as well as a slightly smaller Stokes shift (50 nm). These observations point to weaker charge transfer character probably due to weaker electron withdrawing moiety. The optical properties clearly confirm that the directly joined coumarinoxazaborine moieties allow for efficient intramolecular charge transfer. Further substitutions on these dyes can be used to tune the optical properties such as fluorescence emission wavelength and Stokes shift.

### 1.5.3 Electrochemiluminescence study

The relatively easy accessibility of the first oxidation and first reduction, and the high photoluminescence efficiency prompted us to study their electrochemiluminescence behavior with the so called ECL annihilation mechanism. Thus, ECL behavior was tested by chronoamperometry pulse/cyclic voltammetry and the light detection using a photomultiplier tube (PMT), under the same experimental condition previously reported. A platinum side-oriented 2mm diameter disks was used as working electrode, a platinum spiral as counter electrode and as reference electrode a saturated calomel electrode.

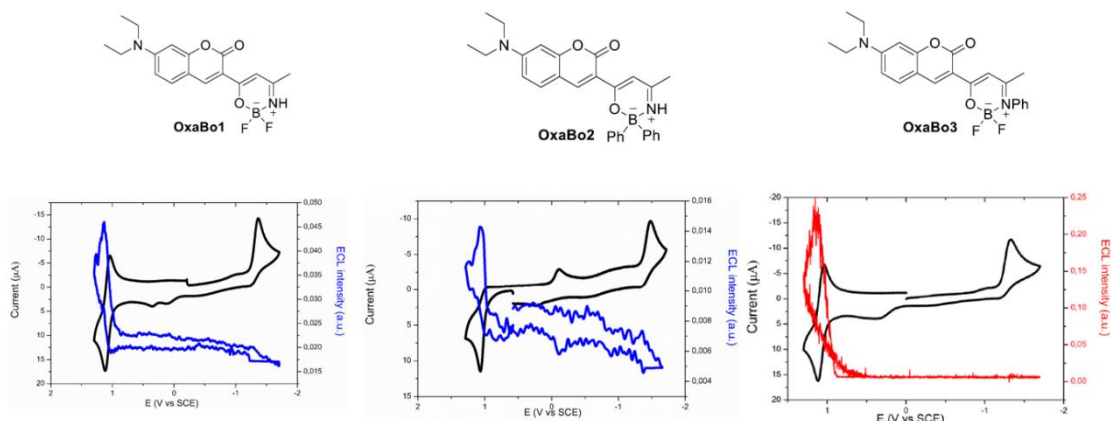


**Figure 1.22:** ECL intensity vs potential for 0.5 mM **OxaBo1-3** (current in black and ECL in blue/red) in  $\text{CH}_3\text{CN/TBAH}$  (0.1M). Working electrode: Pt disk (2mm diameter) vs SCE electrode with scan rate  $100 \text{ mV s}^{-1}$ . PMT bias of 750V.

Figure 1.22 shows the ECL emission that was recorded while cycling the potential between the first reduction and the first oxidation. According to the annihilation mechanism, which is shown in the introduction chapter, the generation of the excited state is induced by the homogeneous electron transfer between the electrogenerated anion and cation. In fact the emission occurs only when both anion and cation are present with an intensity of 0.22 a.u with an oxidation current of  $17.39 \mu\text{A}$ , in the case of **OxaBo3**. On the other hand, **OxaBo1** and **OxaBo2** present a such lower ECL intensity 0.045 and 0.014, respectively.

The **OxaBos** follow the annihilation mechanism for the creation of excited state; thus, the light emission is observed and registered. The observation of an intense ECL emission, easily visible by the naked eye, confirms the annihilation mechanism.

#### 1.5.4 ECL efficiency for **OxaBo** compounds

The ECL emission was intense and stable enough to acquire the ECL spectrum reported in figure 1.23. The spectrum characteristics are similar to PL spectrum with a maximum of emission of 553 nm for **OxaBo3** confirming the generation of the same excited state. Although the 10 nm shift of emission maximum to larger wavelengths is typically observed in the ECL spectra and is associated essentially to a different instrumental configuration or self-absorption, [126],[127] a different concentration between PL and ECL might explain the different broad structures of ECL / PL spectra. ECL spectrum was also recorded for **OxaBo1** while **OxaBo2** ECL emission was not enough intense to acquire reproducible spectrum.



**Table T1.7:** Electrochemiluminescence features for OxaBo molecules

Compound	$\lambda_{\text{ECLmax}}$ (nm)	$\Phi_{\text{ECL}}$ (%)
<b>OxaBo1</b>	521	7
<b>OxaBo2</b>	-	2
<b>OxaBo3</b>	553	20

Thus, ECL was achieved by the energy-sufficient homogeneous electron transfer occurring between the electrochemically generated molecule radical anion and the radical cation. Finally, the ECL efficiency can be calculated by the annihilation method and achieved by chronoamperometric techniques under the same experimental conditions. The results are reported in Table T1.7 and show that compound **OxaBo3** yields is ten times higher than the other compounds and almost four times higher than the standard  $[\text{Ru}(\text{bpy})_3]^{2+}$ .

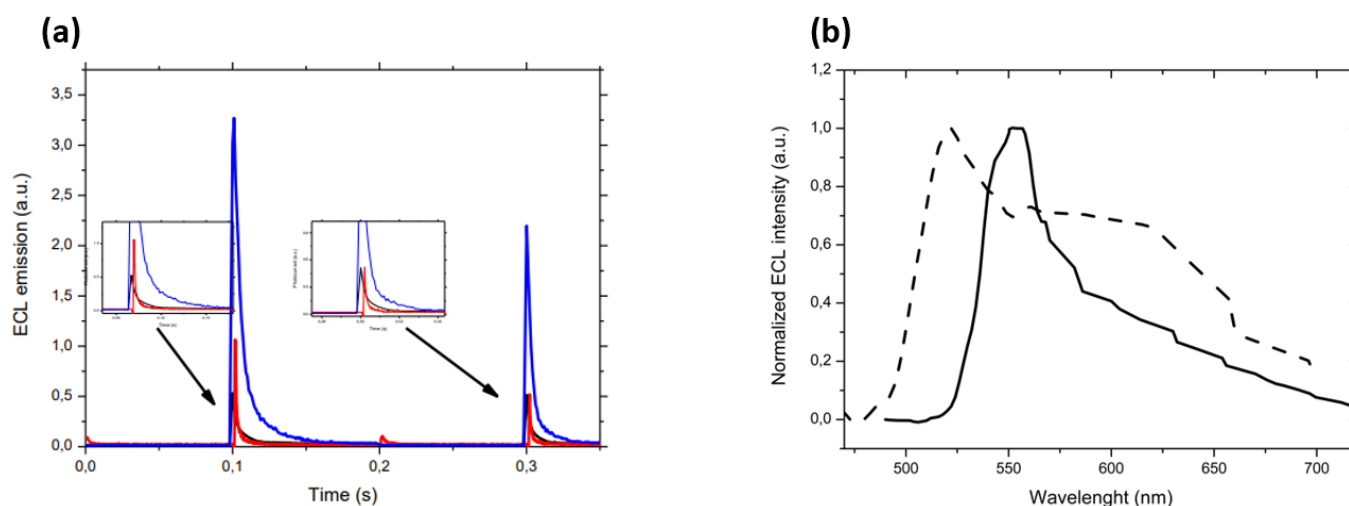


**Figure 1.23** (a) Comparison diagram of photocurrent intensity according of the time of OxaBo1 (black line), OxaBo2 (red line) and OxaBo3 (blue line) during a chronoamperometric impulse. (b) ECL spectra of 0.5mM **OxaBo1** (dash line) and **OxaBo3** (solid line) in  $\text{CH}_3\text{CN}/\text{TBAH}$  (0.1M). Working electrode: Pt disk (2mm diameter) vs SCE electrode. PMT bias of 750V; integration time 100s; step 2nm.

## 1.6 Conclusions

In conclusion, two different categories of luminophorous (metal based and metal free) are characterized using ECL. Initially a group of four iridium-based complexes with different C^N ligands exhibited diverse ECL efficiency, which resulted in 0.5-8%. Consequently, we examine a Ruthenium-based complex with a dppz ligand for application in bio-systems and for a development of an ECL biosensor. This complex, in aprotic conditions, out-turns a really low ECL efficiency (0.05%), which is 100 times of magnitude lower than the standard  $\text{Ru}(\text{bpy})_3^{+2}$  dye.



On the other hand, the electrochemical, photophysical and ECL property of a novel class of coumarinbased oxazaborines was handed over. The change in the connection between oxazaborine and coumarin moiety, led to a substantially improve in the photophysical properties. That can be attributed to higher degree of conjugation in the case of **OxaBo1–3**. These characteristics led this class of molecules to the application in the field of ECL and result in a very high ECL efficiency, four times higher than the standard dyes. Oxazaborines could potentially be applied as ECL luminophores in water by exploding their aggregation induced proprieties and such strategy is currently under investigation in our laboratory. However, a metal free dyes TADFs present a high ECL efficiency, and all complexes stand out due to their balanced redox potentials and their broad applicability in concert with a sound chemical stability. Moreover, we also evaluate the electrochemical features of TADF molecules, which own extended redox windows and they could be identified as ideal luminophores complexes as offering huge advantages such as accessibility, low-cost and metal-free materials. In conclusion, **4DPA\_2Br\_IPN** confers the higher ECL efficiency (7.6%) among TADF dyes.

## References

- [1] M. Su et al. *Anal. Chim. Acta.* 704 (2011) 16–32.
- [2] K.S.V. Santhanam, A.J. Bard *J. Am. Chem. Soc.* 87 (1965) 139–140.
- [3] J. V. Caspar, T.J. Meyer *J. Am. Chem. Soc.* 105 (1983) 5583–5590.
- [4] J. Van Houten, R.J. Watts *J. Am. Chem. Soc.* 98 (1976) 4853–4858.
- [5] H.S. White, A.J. Bard *J. Am. Chem. Soc.* 104 (1982) 6891–6895.
- [6] M.M. Richter, *Electrochemiluminescence ( ECL ),* (2004).
- [7] A. Fiorani et al. *Curr. Opin. Electrochem.* 8 (2018) 31–38.
- [8] S. Stagni et al. *Inorg. Chem.* 45 (2006) 695–709.
- [9] G.J. Barbante et al. *Analyst.* 136 (2011) 1329–1338.
- [10] G.J. Barbante et al. *Inorg. Chem.* 52 (2013) 7448–7459.
- [11] E. Kerr *Chem. – A Eur. J.* 21 (2015) 14987–14995.
- [12] K.N. Swanick *Chem. Commun.* 48 (2012) 3179–3181.
- [13] E.H. Doeven et al. *Chem. Sci.* 4 (2013) 977–982.
- [14] H.D. Abruña *J. Electroanal. Chem.* 175 (1984) 321–326.
- [15] C. Lee et al. *J. Electroanalytical Chem.* 244 (1988) 319–324.
- [16] G. Xiang et al. *ChemElectroChem.* 4 (2017) 1757–1762.
- [17] E.F. Reid et al. *Chem. – A Eur. J.* 19 (2013) 15907–15917.
- [18] W. Miao *Chem. Rev.* 108 (2008) 2506–2553.
- [19] K. Nishimura et al. *Japanese J. Appl. Physics, Part 2 Lett.* 40 (2001).

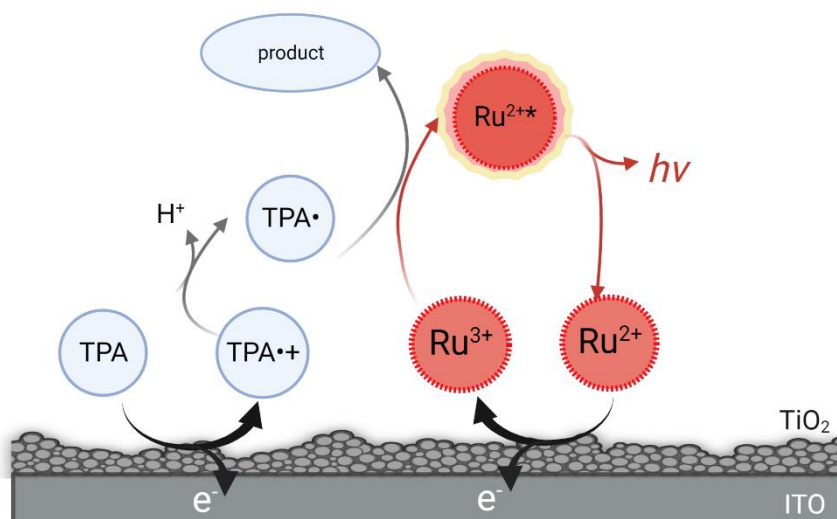
- [20] E.M. Gross et al. *J. Electrochem. Soc.* 149 (2002) E137.
- [21] D. Bruce, M.M. Richter *Anal. Chem.* 74 (2002) 1340–1342.
- [22] B.D. Stringer et al. *Organometallics*. 33 (2014) 4860–4872.
- [23] I.K. Jae et al. *J. Am. Chem. Soc.* 127 (2005) 1614–1615.
- [24] A. Kapturkiewicz *Anal. Bioanal. Chem.* 408 (2016) 7013–7033.
- [25] A. Kapturkiewicz et al. *Electrochem. Commun.* 6 (2004) 827–831.
- [26] A. Kapturkiewicz *Zeitschrift Fur Phys. Chemie.* 220 (2006) 525–542.
- [27] Y. Kawamura et al. *Appl. Phys. Lett.* 86 (2005) 1–3.
- [28] H. Zhou et al. *Chem. – A Eur. J.* 20 (2014) 14736–14743.
- [29] M. Schmittel, S. Qinghai *Chem. Commun.* 48 (2012) 2707–2709.
- [30] K. Chen, M. Schmittel, *Chem. Commun.* 50 (2014) 5756–5759.
- [31] Q. Shu et al. *Inorg. Chem.* 51 (2012) 13123–13127.
- [32] K. Chen et al. *Chem. Soc. Rev.* 44 (2015) 136–160.
- [33] J.M. Fernandez-Hernandez et al. *Anal. Chem.* 88 (2016) 4174–4178.
- [34] M. Schmittel et al. *Dalt. Trans.* 41 (2012) 6064–6068.
- [35] Q. Zhao et al. *Organometallics*. 29 (2010) 1085–1091.
- [36] C. Caporale, M. Massi *Coord. Chem. Rev.* 363 (2018) 71–91.
- [37] L. Murphy et al. *Chem. Commun.* 46 (2010) 8743–8745.
- [38] T.F. Anjong et al. *New J. Chem.* 41 (2016) 377–386.
- [39] D. Parker *Aust. J. Chem.* 64 (2011) 239–243
- [40] M. Zhou, Y. Xia *Anal. Chim. Acta.* 1023 (2018) 29–34.
- [41] C.K. Prier et al. *Chem. Rev.* 113 (2013) 5322–5363.
- [42] D. Wang, D. Astruc *Chem. Rev.* 114 (2014) 6949–6985.
- [43] S. Strasser et al. *Monatshefte Fur Chemie.* 146 (2015) 1143–1151.
- [44] O. Ablialimov et al. *Organometallics*. 33 (2014) 2160–2171.
- [45] C. Gunanathan, D. Milstein *Chem. Rev.* 114 (2014) 12024–12087.
- [46] J. Tönnemann et al. *Eur. J. Inorg. Chem.* 2014 (2014) 4287–4293.
- [47] E. Ivry et al. *Chem. Commun.* 51 (2015) 3870–3873.
- [48] N.E. Tokel, A.J. Bard *J. Am. Chem. Soc.* 94 (1972) 2892.
- [49] R.D. Gerardi et al. *Anal. Chim. Acta.* 378 (1999) 1–41.
- [50] W.Y. Lee *Mikrochim. Acta.* 127 (1997) 19–39.

- [51] A.M. Scott, R. Pyati *J. Phys. Chem. B.* 105 (2001) 9011–9015.
- [52] S. Workman, M.M. Richter *Anal. Chem.* 72 (2000) 5556–5561.
- [53] G.C. Fiaccabrino et al. *Anal. Chem.* 70 (1998) 4157–4161.
- [54] J.J. Wilson, S.J. Lippard *Chem. Rev.* 114 (2014) 4470–4495.
- [55] F. Trudu et al. *J. Appl. Biomed.* 13 (2015) 79–103.
- [56] V. Ramu et al. *Chem. – A Eur. J.* 21 (2015) 9185–9197.
- [57] A. Bergamo et al. *Invest. New Drugs.* 33 (2015) 53–63.
- [58] A. Valente, M.H. Garcia *Inorganics.* 2 (2014) 96–114.
- [59] F. Guidi et al. *J. Inorg. Biochem.* 118 (2013) 94–99.
- [60] K. Wu et al. *Metallomics.* 4 (2012) 139–148.
- [61] N.A. Vyas et al. *Eur. J. Med. Chem.* 75 (2014) 375–381.
- [62] L. Xiao et al. *Dye. Pigment.* 113 (2015) 165–173.
- [63] P. Chellan et al. *Dalt. Trans.* 43 (2014) 513–526.
- [64] P. Kalaivani et al. *Inorg. Chem. Front.* 1 (2014) 311–324.
- [65] D. Sun et al. *Inorg. Chem. Commun.* 56 (2015) 17–21.
- [66] A. Mishra et al. *Organometallics.* 33 (2014) 1144–1151.
- [67] F.Z. Sadafi et al. *ChemMedChem.* 9 (2014) 1660–1664.
- [68] L. He et al. *Adv. Funct. Mater.* 24 (2014) 2754–2763.
- [69] R. Pettinari et al. *Organometallics.* 33 (2014) 3709–3715.
- [70] I. Collins, A.M. Jones, *Molecules.* 19 (2014) 17221–17255.
- [71] C. Mari et al. *Chem. Sci.* 6 (2015) 2660–2686.
- [72] T. Joshi, G. Gasser, *Synlett.* 26 (2015) 275–284.
- [73] M. Dickerson et al. *Inorg. Chem.* 53 (2014) 10370–10377.
- [74] M.A. Sgambellone et al. *J. Am. Chem. Soc.* 135 (2013) 11274–11282.
- [75] R.B. Sears et al. *J. Inorg. Biochem.* 121 (2013) 77–87.
- [76] M. Frasconi et al. *J. Am. Chem. Soc.* 135 (2013) 11603–11613.
- [77] Y. Nakabayashi et al. *Inorganica Chim. Acta.* 423 (2014) 109–114.
- [78] A. Frei et al. *J. Med. Chem.* 57 (2014) 7280–7292.
- [79] J.J. Soldevila-Barreda et al. *Nat. Commun.* 6 (2015).
- [80] R.G. De Lima et al. *Molecules.* 19 (2014) 9628–9654.
- [81] A. Tahghighi, *J. Organomet. Chem.* 770 (2014) 51–60.

- [82] A.E. Friedman et al. *J. Am. Chem. Soc.* 112 (1990) 4960–4962.
- [83] A.W. McKinley et al. *Coord. Chem. Rev.* 255 (2011) 2676–2692.
- [84] J.A. Smith et al. *Coord. Chem. Rev.* 255 (2011) 2666–2675.
- [85] S. Delaney et al. *Inorg. Chem.* 41 (2002) 1966–1974.
- [86] J. Jin et al. *Nat. Commun.* 11 (2020) 1–9.
- [87] J. Zhang et al. *ACS Appl. Mater. Interfaces.* 11 (2019) 41051–41061.
- [88] S. Xu et al. *ACS Sensors.* 5 (2020) 1650–1656.
- [89] R. Ishimatsu et al. *Chem. – A Eur. J.* 22 (2016) 4889–4898.
- [90] Q. Zhang et al. *Chem. Commun.* 55 (2019) 5639–5642.
- [91] C.J. Christopherson et al. *ACS Appl. Mater. Interfaces.* 12 (2020) 20000–20011.
- [92] Y.F. Xiao et al. *Chem. Sci.* 11 (2020) 888–895.
- [93] J. Zhang et al. *Chem. Commun.* 52 (2016) 11744–11747.
- [94] Z. Liu et al. *J. Control. Release.* 310 (2019) 1–10.
- [95] A.B. Nepomnyashchii, A.J. Bard *Acc. Chem. Res.* 45 (2012) 1844–1853.
- [96] A.B. Nepomnyashchii et al. *J. Am. Chem. Soc.* 133 (2011) 8633–8645.
- [97] M. Hesari et al. *Chem. Commun.* 51 (2015) 1081–1084.
- [98] A. Venkatanarayanan et al. *Electrochem. Commun.* 21 (2012) 46–49.
- [99] A. Martin et al. *Chem. Commun.* 48 (2012) 5617–5619.
- [100] A. Venkatanarayanan et al., *Electrochem. Commun.* 31 (2013) 116–119.
- [101] D. Frath et al. *Angew. Chemie – Int. Ed.* 53 (2014) 2290–2310.
- [102] D. Zhou et al. *ACS Appl. Mater. Interfaces.* 11 (2019) 24339–24348.
- [103] G. Li et al. *ACS Appl. Mater. Interfaces.* 11 (2019) 32209–32217.
- [104] C.F.A. Gómez-Durán et al. *Chem. Commun.* 46 (2010) 5103–5105.
- [105] G. Ulrich et al. *Angew. Chemie – Int. Ed.* 47 (2008) 1184–1201.
- [106] G.A. Andrade et al. *ACS Catal.* 3 (2013) 1685–1692.
- [107] A. Khatchadourian et al. *Biochemistry.* 48 (2009) 5658–5668.
- [108] J. Rosenthal, S.J. Lippard et al. *J. Am. Chem. Soc.* 132 (2010) 5536–5537.
- [109] A. Loudet et al. *Chem. Rev.* 107 (2007) 4891–4932.
- [110] A.B. Nepomnyashchii et al. *J. Phys. Chem. C.* 114 (2010) 14453–14460.
- [111] V. Lakshmi, M. Ravikanth, *Chem. Phys. Lett.* 564 (2013) 93–97.
- [112] K. Krumova, G. Cosa *J. Am. Chem. Soc.* 132 (2010) 17560–17569.

- [113] X. Zhang et al. *Chem. Sci.* 13 (2022) 6244–6253.
- [114] A.B. Nepomnyashchii et al. *J. Am. Chem. Soc.* 133 (2011) 19498–19504.
- [115] J. Rosenthal et al. *J. Phys. Chem. C.* 115 (2011) 17993–18001.
- [116] C. Booker et al. *Angew. Chemie – Int. Ed.* 47 (2008) 7731–7735.
- [117] N.E. Tokel-Takvoryan et al. *J. Am. Chem. Soc.* 95 (1973) 6582–6589.
- [118] S. Fukuzumi et al. *J. Am. Chem. Soc.* 126 (2004) 1600–1601.
- [119] K. Rybicka-Jasińska et al. *J. Am. Chem. Soc.* 138 (2016) 15451–15458.
- [120] H. Uoyama et al. *Nature.* 492 (2012) 234–238.
- [121] J. Luo, J. Zhang *ACS Catal.* 6 (2016) 873–877.
- [122] N.T. Zhang et al. *J. Org. Chem.* 78 (2013) 2104–2110.
- [123] S. V. Jovanovic et al. *J. Phys. Chem.* 95 (1991) 10824–10827.
- [124] R. Francke, R.D. Little *J. Am. Chem. Soc.* 136 (2014) 427–435.
- [125] T. Mikysek et al. *ChemElectroChem.* 7 (2020) 1550–1557.
- [126] G. Valenti et al. *Chem. – A Eur. J.* 21 (2015) 2936–2947.
- [127] S. Kudruk et al. *Chem. Commun.* 54 (2018) 4999–5002.
- [128] H. Tanaka et al. *Chem. Commun.* 48 (2012) 11392–11394
- [129] Y. Xu et al. *Adv. Materials.* 33 (2021) 2100652.
- [130] J. Zhang et al. *ACS Appl. Mater. Interfaces* 8 (2016) 11355–11365
- [131] A. Treibs et al. *Anal. Chem.* 718 (1968) 208–223

## CHAPTER 2



**Would the use of semi-conductors for Electrochemiluminescence applications be possible?**

## 2.1 Introduction

After the analysis of the luminophores molecules in Chapter 1, it must be mentioned that in ECL applications the most important parameter is not just the dye. In this chapter we will delve into different types of semiconductors such as titanium dioxide ( $\text{TiO}_2$ ), which is the most known semiconductor. The  $\text{TiO}_2$  has made an impression on a considerable number of scientists because of its high orientation, low-cost, non-toxicity, adjustable mesopore size, high internal surface area, superior physicochemical stability and high catalytic activity [1–5]. In the field of solar cells[6],[7] or photoreactors [8],  $\text{TiO}_2$  composites have become an active research topic in recent years. In addition, some  $\text{TiO}_2$ -based electrochemiluminescence (ECL) platforms have recently been widely studied to further increase their ECL efficiency. For example, narrow-band-gap metal semiconductors, noble-metal nanoparticles and non-metal elements have been loaded onto  $\text{TiO}_2$  to improve their ECL efficiency [9–11]. However, because of the participation of toxic metals in the reaction, these sensitizers can lead to serious environmental and human health damage, which limits their widespread application.

### 2.1.1 Semiconductors

Semiconductors are a class of solids characterized by a small number of free electrons in contrast to metals that present many free electrons and insulators that have few free electrons. Another important feature is related to the values displayed by the energy gap  $E_g$  (energy gap) between the conduction and valence bands, as it is presented in figure 2.1.

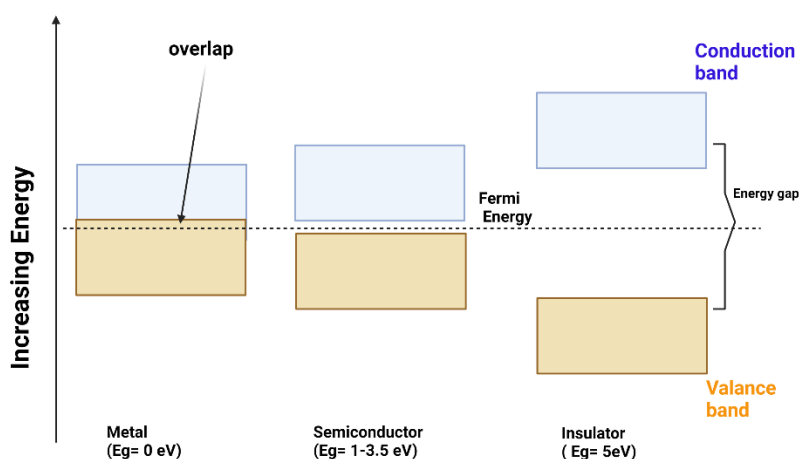
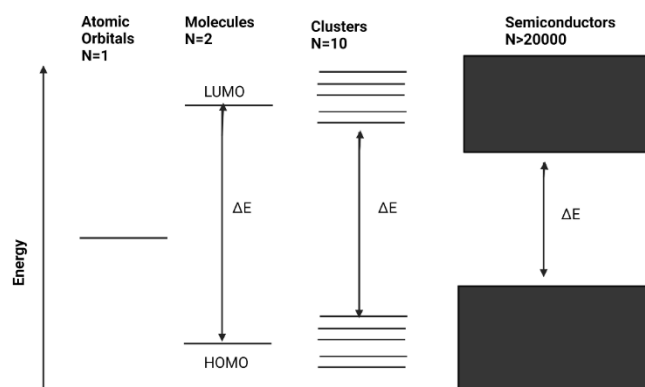


Figure 2.1: Scheme of Energy levels of metals/semiconductors/ insulators.

Figure 2.1 shows the relative position of the valence and conduction bands for the three classes of solid materials. In conductors (zero energy gap) it is easy for electrons to leap from the valence band to the conduction band. In insulators it is almost impossible for one of the valence electrons to leap into the conduction band, due to high values of  $E_g$  ( $\approx 5\text{eV}$ ). In semiconductors, however, if the valence electrons absorb energy in some way, it is possible to overcome the energy gap  $E_g$  which does not have very substantial values (1-3.5 eV)[12],[13] enter the conduction band, and become free ( $e^-$ ). The vacancies they leave in the valence band are called holes ( $h^+$ ).

### 2.1.1.1 Energy band theory

In a single atom, the electrons are around the nucleus and their energies are quantized, i.e. they can only have a certain discrete value of  $E_n$  ( $n=1,2,3,\dots$ ). In the ground state the electron energy is negative relative to the vacuum level. The allowed energy levels are distinct, separated from each other by forbidden regions and include a certain number of electronic states. The case is considered in which  $N$  atoms bond together to form a crystalline solid. As the distances between them decrease, the orbits of the valence electrons overlap, and the electrons could interact with the nucleus of neighboring atoms [14]. But Pauli's prohibitive principle, which states that in each energy level there can be only two electrons and indeed with opposite spin, dictates the separation of the energy diagram into  $N$  number of very closely spaced stations. As the distance between the atoms decreases, other inner orbitals begin to overlap and their energy levels are also split into  $N$  closely spaced levels. Each group of separate energy stations is called an energy zone. The zones are separated from each other by energy gaps, i.e. forbidden energy values in which free carriers cannot exist.



**Figure 2.2:** Change in the electronic structure of the solid as the number of monomer units increases from unit to semiconductor formation.



In each system there is a certain number of electrons that occur in the bonds where they also occupy the allowed levels of the crystal lattice. The last band that has occupied orbitals is called the valence band while the first band that does not have all the energy levels occupied is called the conduction band. Therefore, the valence band and the conduction band are separated by  $E_g$  so that the energy gap is the energy difference between the energy  $E_c$ , the bottom end of the conduction band, and the energy  $E_v$ , the top of the valence band where:

$$E_g = E_c - E_v$$

Depending on whether the last occupied level of the atoms forming the solid is fully or incompletely occupied, the last energy band will also be fully or incompletely occupied. If a band is fully occupied, its electrons cannot contribute to the conductivity of the material and they cannot take energy from an external source or electric field and move, since there are no energy states available for them close to the filled ones[15]. Thus, the conductivity of each material (electrical and thermal) is due only to the electrons of the last bands. The quantum mechanical study of the motion of electrons in the solid states that the valence electrons move through the bulk of the solid as if they were free, without colliding with the ions, due to their wave behavior [16].

### 2.1.1.2 Endogenous Semiconductors

Endogenous semiconductors are the semiconductors that do not have any impurities. The most common semiconductors in electronic devices are germanium (Ge) and silicon (Si) [17]. Consider a pure silicon semiconductor crystal, such as in figure 2.3. Each atom, as is known, will have four outer electrons, each of which participates in a bond with another electron of a neighboring atom.

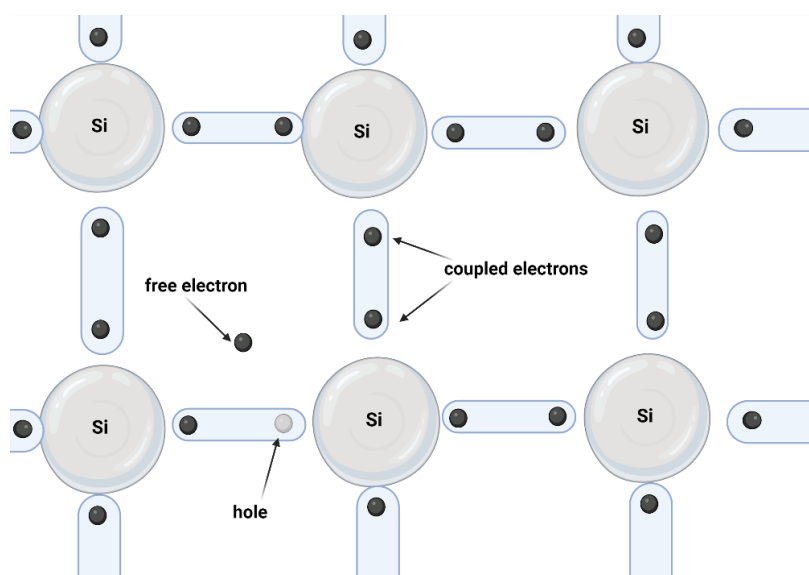


**Figure 2.3:** Crystal structure of an endogenous semiconductor.

Thus, each atom is connected by four bonds with an equal number of neighboring atoms, which implies the existence of a strong crystal lattice. In this state, all electrons are bound, resulting in no conduction in the crystal. But if, for any reason, an increased amount of energy hits one of the outer electrons of an atom, this entails the breaking of the corresponding bond and the release of the corresponding electron. The freed electron now becomes a free electron and moves randomly, like ideal gas molecules, throughout the mass of the crystal. The empty position created in this way is most likely to be occupied by a neighboring electron, thus giving the impression that it itself moved towards the position of origin of this electron. The whole phenomenon leads to the hypothesis of the existence of a separate particle, with a charge opposite to the electron, called a hole. As proved theoretically and experimentally, the hole is a particle with its own material existence[17][18].

As can be seen, inside of this semiconductor there are two kinds of free particles holding an opposite charge. The free electrons maintain a negative charge and the holes a positive charge. These particles can move under the influence of any external electric field, and both contribute greatly in the conductivity of the crystal.

### **2.1.1.3 Exogenous Semiconductors**

The second category of semiconductors are the endogenous ones. The addition of admixtures (doping) to semiconductors has an extreme effect in their conductivity. Depending on the type of doping, we can achieve an n-type semiconductor with conductivity due almost exclusively to electrons or a p-type semiconductor with hole conduction. Without this doping, semiconductors would be a curious phenomenon of the natural solid state and nothing more [19].

Considering what happens with the addition of a pure Si crystal, a small amount of a pentavalent element which belongs to group V of the periodic table such as the arsenic (As). Each atom of the doping can be surrounded by millions of silicon atoms and therefore forced to form bonds only with silicon atoms, thus preserving the crystalline structure of diamond that silicon has. For this reason, a very small amount of the dopant is added (approximately one dopant atom corresponds to one million silicon atoms). Arsenic has five valence electrons while silicon has only four. Therefore, when an As atom forms bonds with four Si atoms, one of its electrons will remain unbonded. This electron will not be able to join a bond and consequently will remain in orbit around the As atom.

The fifth valence electron can be easily released through the thermal oscillations of the Si lattice. The electron will then be free inside the semiconductor, i.e. it will be in the conduction band. The addition of the As atoms introduces localized electronic states where the As atoms are located since the fifth electron has a localized (hydrogen-like) wave function around  $As^+$ . Thermal excitation due to lattice oscillations at room temperature is sufficient to ionize the As atom, i.e. to incite an electron and move it into the conduction band. Because the As atom donates an electron to the conduction band we say it acts as a donor [20].

When a trivalent atom, such as boron, is added to a Si crystal (B) the final product will be a p-type Si crystal. As B has only three valence electrons, when shared with four neighboring Si atoms, one of the bonds will have one less electron, which is equivalent to having a hole. It is possible for a neighboring electron to tunnel into the position of this hole. This way the hole essentially moves away from the B atom. As the hole moves away it is simultaneously attracted by the negative charge left on the B atom and ends up rotating around the boron ion  $B^-$ . The binding energy of the hole to the  $B^-$  ion is very small (about 0.05 eV), so at room temperature the thermal lattice vibrations have sufficient energy to dislodge the hole from the  $B^-$  ion region. Hole detachment involves the capture of an electron from a neighboring Si-Si bond in the valence band. As a result, the hole moves away from the  $B^-$  ion and moves into the valence band [21][22]. Then the B atom introduced into the Si crystal acts as an electron acceptor and is thus called an acceptor impurity. The electron bound by the B atom comes from a neighboring bond. Consequently, when adulterating a Si crystal with a trivalent doping, a p-type material is created. Since the negatively charged B atoms are immobile and cannot contribute to electrical conductivity, the transfer of electricity happens mainly by holes rather than electrons. If a semiconductor is n-type, then the Fermi energy level is placed below the conduction band and just above the donor energy level, while correspondingly for p-type the exact opposite occurs [23].

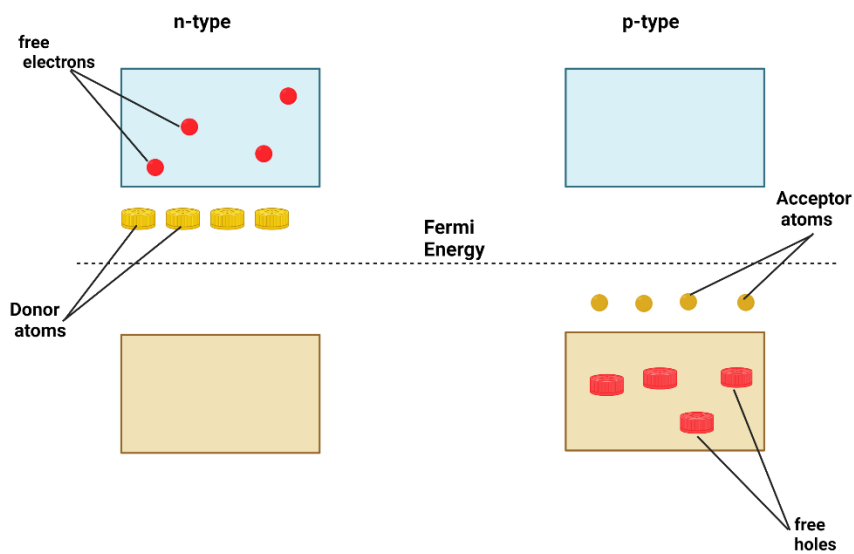


**Figure 2.4:** Scheme for the conduction and valance band for the n and p type semiconductors.

### 2.1.2 Titanium Dioxide ( $TiO_2$ )

Titanium dioxide ( $TiO_2$ ) or titania is a material with a wide range of common applications as well as high-tech applications. It is cheap, non-toxic, chemically stable and biocompatible. Among semiconductors,  $TiO_2$  occupies a special place. With an annual production of approximately three million tons, the  $TiO_2$  industry is valued at over \$5.5 billion. Typical uses of  $TiO_2$  are in heterogeneous catalysis[24], in the photocatalysis of mainly gaseous pollutants[25], in the production of hydrogen and

electricity in solar cells[26], as a gas sensor[27], as a dyestuff due to its high light scattering index, as an anti-corrosion coating, in bone implants, in electronic devices (varistor, Mosfet), in electrochromic devices and finally in lithium-ion batteries[28]. It is a very popular material because it can be easily prepared by sputtering and annealing. Finally in this chapter the use of TiO<sub>2</sub> material in electrochemiluminescence will be analyzed, as it has already been investigated for electrochemistry applications [25].

### **2.1.2.1 Electronic structure of TiO<sub>2</sub>**

Titanium dioxide is divided in three crystalline phases (brookite, rutile and anatase). The most important are rutile and anatase structure. Rutile is characterized as a direct band gap semiconductor with an energy gap of 3 eV, while anatase is characterized as an indirect band gap with an energy gap of 3.2 eV. The lower part of the valence band consists of O<sub>2s</sub> orbitals, while the upper part consists of O<sub>2p</sub> orbitals and has a total range of 6.22 eV. The lowest energy levels of the conduction band consist of two bands of Ti<sub>3d</sub> orbitals, with a range of 5.9 eV[29–31].

### **2.1.2.2 Uses and advantages of TiO<sub>2</sub>**

As the most known metal oxide (Mox) material, TiO<sub>2</sub> has been used for several uses, owing different nanostructures. The uses of TiO<sub>2</sub> nanomorphologies as nanosheets [32], nanopillars[33], nanoarrays [34], nanoparticles [35], nanorods [36], nanowires [37], nanoneedles[38], nanoflowers [39], nanocubes [40] and mesocrystals [41],[42] have been reported for bioanalytical uses. On the other hand, on ECL field TiO<sub>2</sub> has been used for the enhancement of ECL signal combined with other carbon materials in a standard system of ruthenium complex and TPA[38],[43]. All of these researches have been based on some advantages of TiO<sub>2</sub> such as:

1. Homogeneous distribution of pores. Pore size 25-45 nm.
2. Large active surface with complex morphology, high roughness factor and very large surface development. It essentially acts as an ideal substrate that absorbs large concentrations of protein molecules.
3. An n-type semiconductor with an energy gap of ~3.23 eV allows the study of redox reactions.
4. The isoelectric point of TiO<sub>2</sub> (4.9-5.2) makes it easy to immobilize positively charged proteins such as cytochrome c and hemoglobin.

5. Optically transparent material in the visible light (390-800 nm), the absorption spectrum of  $\text{TiO}_2$  does not coincide with the absorption spectrum of the protein, so it is easy to monitor the immobilization.
6. Their preparation is easy and low-cost.

### 2.1.3 Zirconium dioxide ( $\text{ZrO}_2$ )

Zirconium dioxide ( $\text{ZrO}_2$ ) is a white crystalline solid which occurs naturally in the form of mineral, baddeleyite, having a monoclinic structure. It is a very interesting material and is receiving growing attention as a result of its wide use as a catalyst, as a refractory, an insulator in transistors in future nano-electronic devices, in oxygen sensors, fuel cells, orthopedic implants and prosthetic dentistry for the fabrication of crowns and fixed partial dentures [46]. The three well-defined polymorphs of Zirconia under normal atmosphere and at different temperatures are cubic (c- $\text{ZrO}_2$ ), tetragonal (t- $\text{ZrO}_2$ ), and monoclinic (m- $\text{ZrO}_2$ ) [47-50]. Also, zirconium oxide is a wide bandgap (5.0 eV) semiconductor material [17, 18] with high thermal stability, high surface area. Hence, solid  $\text{ZrO}_2$  be able to conduct certain amount of electricity and it is considered as p-type semiconductor.

Some advantages of nanostructured  $\text{ZrO}_2$  such as biomedical applications due to affordable, scalable production, easy surface modifications, tunable surface morphology, multiphase stability, and acceptability by biological features such as biocompatibility, viability for bioactive, and a high isoelectric point of 9.5. Zr-nanoparticles demonstrate notable high performance to develop next-generation biosensors, implanted materials, and bioelectronics. This is an important fact that make them one of the most important Mox in the field of electrochemistry.

## 2.2 Electrochemical characterization of Mox materials using ECL

Fluorine doped tin-oxide (FTO) has been chosen as the electrochemical platform which will host the Mox. Two different Mox was selected for the ECL analysis  $\text{TiO}_2$  and zirconium dioxide ( $\text{ZrO}_2$ ) as a more transparent Mox material. The selection of the anatase structure of  $\text{TiO}_2$  presents higher conductivity and stability instead of the rutile and brookite). Furthermore, some important advantages have been considered as they are mentioned in chapter 1.1.2.1 and 1.1.2.2; on the other hand,  $\text{ZrO}_2$  is also an important Mox with larger band gap (5 eV) and more transparent than the  $\text{TiO}_2$ . In this case the selection of  $\text{ZrO}_2$  was based on its band gap and because of its transparency, since a more transparent material would be better for the detection of the light emission during ECL process. Moreover, two different thicknesses (T:  $10\mu\text{m}$  of  $\text{TiO}_2$  and TAO:  $10\mu\text{m}$  of  $\text{TiO}_2$  and  $5\mu\text{m}$  of opaque  $\text{TiO}_2$ ) of  $\text{TiO}_2$  (Table 2.1) were used in ECL process (figure 2.5); to do so, a standard solution of  $30\mu\text{M}$   $\text{Ru}(\text{bpy})_3^{+2}$  with

200mM TPA was prepared in Phosphate buffer (PB) 0.2M pH 6.8; in scan rate 0.1 V/s. For the detection of light emission, a photomultiplier (PMT) has been used, which is placed in a dark box with an applied voltage of 750V, as described in chapter 1.

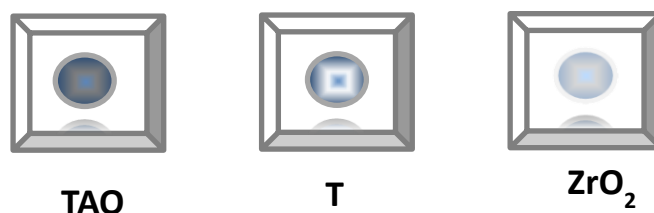


**Figure 2.5:** Top view of Mox electrodes for ECL applications.

**Table T2.1:** Mox electrodes' specification.

Name	Characteristics
<b>TAO:</b> Titanium dioxide electrode	Double layer of TiO <sub>2</sub> of 10μm and addition of 5μm opaque layer onto FTO
<b>T:</b> Titanium dioxide electrode	TiO <sub>2</sub> 10μm thickness onto FTO
<b>ZrO<sub>2</sub>:</b> Zirconium dioxide	5μm thickness onto FTO

### 2.2.1 Electrochemical performance for Mox

After the preparation of the samples in collaboration with Prof. A. Licciardelo from the University of Catania, an individual experiment of cyclic voltammetry (CV) has been performed in a solution of 30mM of TPA in PB 0.2M pH 6.8. This process was used for the investigation of TPA's oxidation using four different electrode materials (a bare FTO, a TAO, a T and a ZrO<sub>2</sub>).

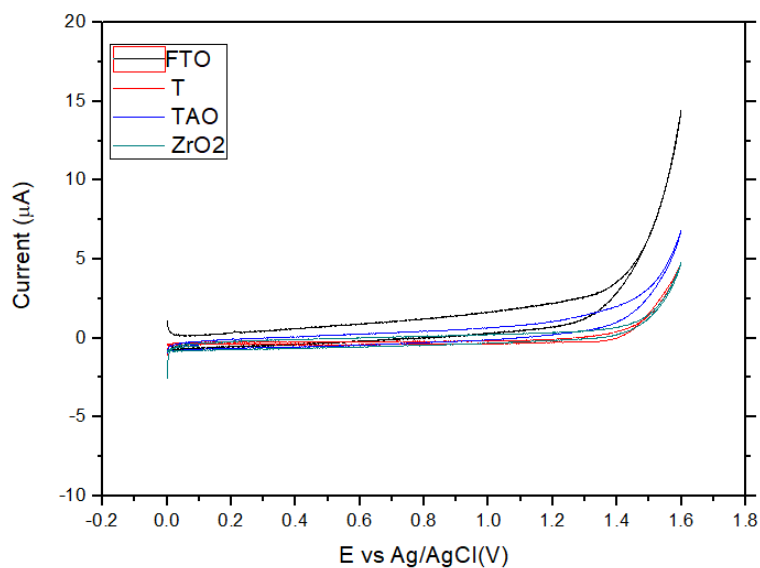


**Figure 2.6:** Electrochemical response of four electrodes in 30mM TPA/PB 0.2M pH 6.8 solution.

Figure 2.6 presents the anodic biases of each material in a range from 0 to +1.6V. Even if the Mox in this range are insulators, small differences are observed at +0.9V; in which occurs the oxidation potential of TPA. Among the nanostructured electrodes no differences are observed, through the currents remain constant owing a value of 1-2  $\mu\text{A}$ . The best electrochemical response has obtained from the bare FTO electrode, a possible explanation in this phenomenon would be the blocking of electron-proton transfer from the FTO surface to TPA. A bare FTO can oxidize easier the TPA molecules when they are in the solution, thus when the addition of a layer of nanostructured materials had been used, this process had slowed down.

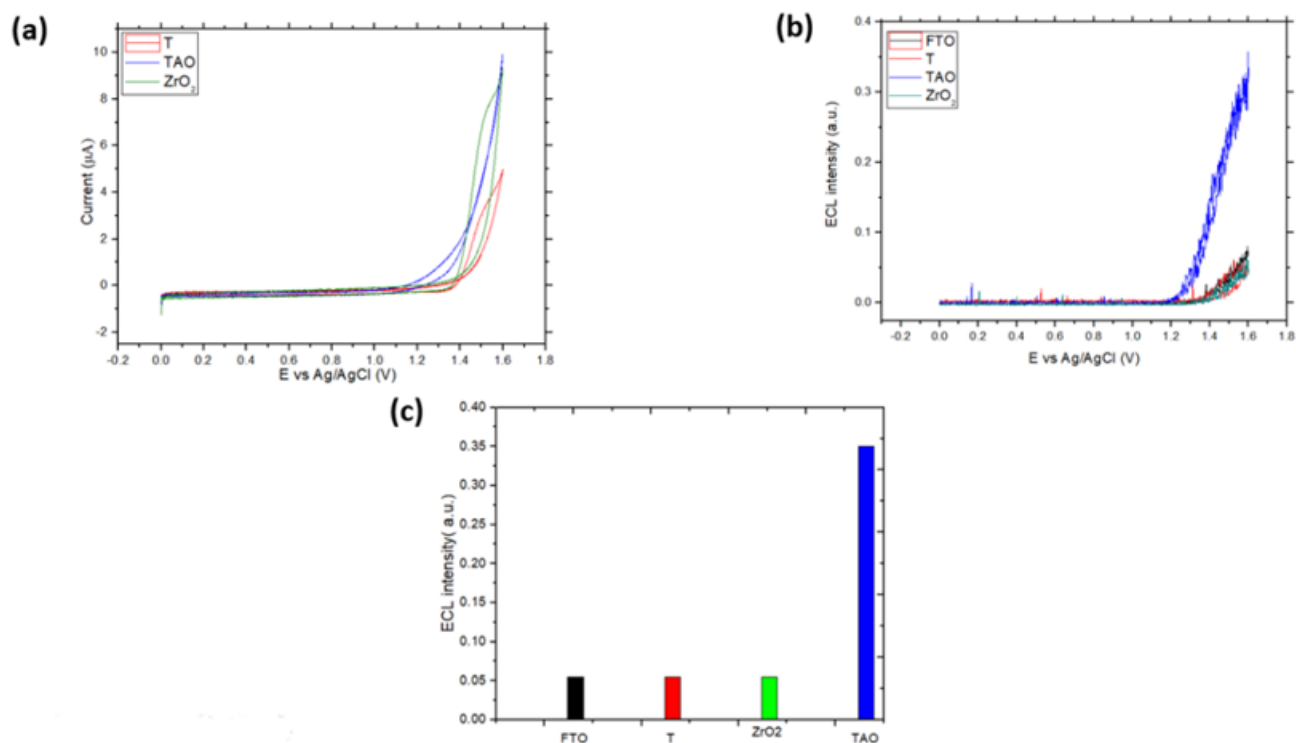


**Figure 2.7:** (a) CV of Mox/FTO electrodes in PB 0.2M pH 6.8 with 200mM of TPA (b) ECL intensity vs potential for the Mox/FTO electrodes and a bare FTO electrode. Reference electrode Ag/AgCl (V) with scan rate  $0.1 \text{ V s}^{-1}$ , in PB 0.2M pH6.8 with  $30 \mu\text{M Ru}(\text{bpy})_3^{+2}$  200mM of TPA. PMT bias of 750 V; amplification  $00.0 \mu\text{A}$ . (c) ECL intensity of each electrode.

As no curves changes are observed using a solution of PB 0.2M pH 6.8 with 30mM of TPA, the next step contains the analysis of Mox in a more concentrated solution of TPA (200mM), by investigating the differences of the anodic currents. Figure 2.7a exhibits the anodic currents of each Mox/FTO electrode in the presence of 200mM TPA, in which the highest anodic currents are presented by the TAO and ZrO<sub>2</sub> electrodes. On the other hand, T electrode obtains the lower anodic current value, thus it was tested in the same range of potentials. A possible explanation would be the TAO electrode is capable to receive electrons (from the TPA oxidation) much faster than the rest of the electrodes, which is confirmed by the potential (Figure2.7a), thus the oxidation reaction starts (+1.15V). In this case we suppose that TAO may also present a high ECL intensity.

Progressively, the use of both coreactant and luminophores in PB 0.2M pH6.8 with  $30 \mu\text{M Ru}(\text{bpy})_3^{+2}$  and 200mM of TPA arises. According to the mechanism in the homogeneous phase of coreactant and luminophores (see Introduction Chapter Figure I.1), the ECL intensity of Mox/FTO electrodes is investigated (figure 2.7b) during a CV process of each electrode under the same experimental conditions.

The blue line TAO electrode shows the highest ECL intensity (0.35a.u.) among the rest of the electrodes; on the other hand, the rest of them exhibit an ECL intensity around 0.05a.u. This ECL behavior, as mentioned above, is expected by the double layer of



TiO<sub>2</sub> material. What renders the TAO electrode capable for further investigation is not only the value of ECL intensity, but also the potential of starting the chemical reaction. In general, the oxidation potential of TPA ensues at +0.9V, this way the radical cations are created. According to figure 2.7a, b at +0.9V no current changes are observed. Consequently, TAO's ECL intensity starts to increase at +1.2V, which means that the radical cations react with the Ru(bpy)<sub>3</sub><sup>+3</sup> and the light emission occurs.

On the contrary, for the rest of the electrodes, more energy (+1.35V) has been needed to stimulate the reaction and as result the light emission. In conclusion, the double layer of TiO<sub>2</sub> (transparent and opaque layer), may assist the faster reaction between luminophores and coreactant and the light emission could occur much faster than in the other cases. The ECL intensity differences of every Mox/FTO electrode are presented in the figure 2.7c; therefore, TAO is about an order of magnitude more efficient than the other electrode materials.

### **2.2.2 Ruthenium complex immobilized in Mox/FTO electrodes in different thicknesses.**

In the chapter 2.2.1 the ECL intensity of three different nanostructured electrodes in homogenous phase has been tested. The TAO electrode was the one which presented the best ECL intensity, so further investigation has been performed focused on this nanostructured material. In this chapter, in our system, the luminophore is immobilized within the outer layer of the TiO<sub>2</sub> film (figure 2.8) at sufficiently large distances (>> tunneling distance) from the electrode surface to impede its oxidation. To achieve that functionalized 3D nanostructured electrodes have been developed, based on the Zr-P priming methodology. On the Zr-modified region was then selectively bounded a Ru(bpy)<sub>3</sub><sup>2+</sup> luminophore (in this present case carrying phosphonic groups). Such a methodology involves the growth, within the pores of the nanostructured film, of a zirconium phosphate monolayer acting as a platform for the anchoring, through a very robust phosphate-zirconium- phosphonate structure, of any organic molecule bearing a phosphonic group. Titania nanostructured films were hence modified to obtain electrodes with a "graded" composition where the thickness of the Zr-phosphate-modified layer was varied from a few nm (the outer part of the nanostructured TiO<sub>2</sub> film) down to the whole film thickness. This happens to control the oxidation of both luminophores and coreactant or only the coreactant on the working mechanism (figure 2.8).

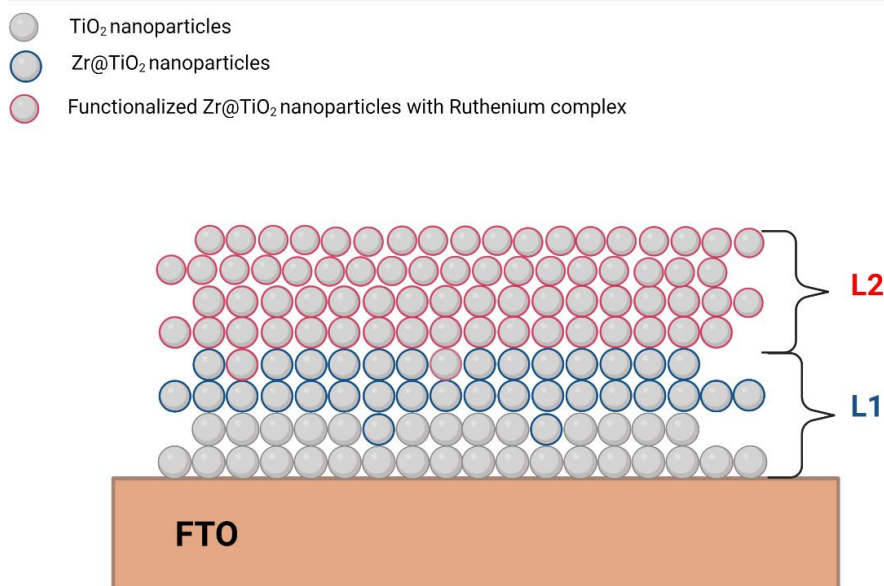


**Figure 2.8:** Structural parameters of the 3D nanostructured  $\text{TiO}_2$  film owing a distance of immobilized ruthenium complex. (L1 the distance between FTO and the first layer of functionalized  $\text{Zr@TiO}_2$  nanoparticles, and L2 the thickness of the  $\text{Ru@Zr@TiO}_2$ .)

According to the thickness of the film, three different mechanisms for the light emission are presented in figure 2.9. First both coreactant and luminophorous are oxidised in the surface of the electrode, the oxidised ruthenium interacts with the TPA's radical and the final result is the creation of the Ru's excited state and light emission. In such a case, in fact, ECL is mainly generated through the classical highly efficient oxidative-reduction or catalytic routes (figures 2.9a and 2.9b), both involving the direct anodic oxidation of the luminophore ( $\text{Ru}(\text{bpy})_3^{2+}$ ). Intense emission may therefore also occur from underneath the mitochondrion hence lowering the achievable contrast. In fact, the sole remaining route for ECL generation operating in our system is the so-called "remote ECL" mechanism (figure 2.9c), which involves the TPA radicals and radical cations. The species generated at the electrode surface is  $\text{TPA}^+$ : it has a limited lifetime (namely  $200\mu\text{s}$ ) [44],[45] and spontaneously deprotonates to the radical TPA while diffusing across the  $\text{TiO}_2$  film. The "remote ECL" mechanism is intrinsically less efficient than the previous ones and this allows, in our system, to strictly control the intensity and vertical profile of the ECL emission by acting on two intrinsic factors, i.e., the thickness of the Ru-bearing  $\text{TiO}_2$  outer layer (L2 in figure 2.8) and the distance of such layer from the underlying TCO (ITO or FTO) electrode (L1 in figure 2.8).

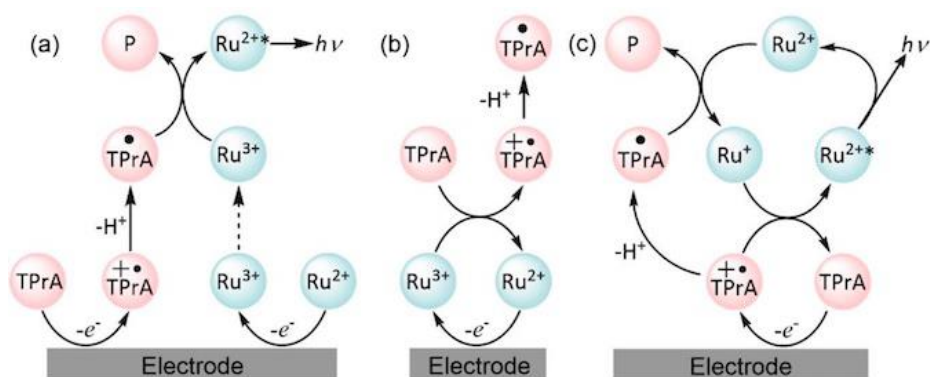


**Figure 2.9:** The three canonical mechanisms of ECL generation: (a) the oxidative-reduction route (b) the catalytic route and (c) the “remote” ECL route. In the latter, at variance with (a) and (b), TPA radicals are only involved, and it can be operative when the luminophores cannot interact with the electrode.

Firstly, three 3D nanostructured electrodes with different L1 thickness, were checked in a PB 0.2M/TPA 180mM, pH 6.78 solution. Table 2.2 presents the features of the thickness of each case. Figure 2.10a exhibits the electrochemical behaviour of the TPA and Ruthenium oxidation of each electrodes. A wide oxidation peak is presented around +1.2V for the CT-AD electrode; instead for the rest of the electrodes (XL-A and XL-C) an increase of the anodic biases is presented. In the case of CT-AD where the distance between luminophorous and electrode is 0 $\mu$ m, we can trigger easier both the oxidation of TPA and Ruthenium (see figure 2.9a). On the other hand, when the L1 distance is 2.7 and 3.75  $\mu$ m ( electrodes XL-A and XL-C), the ruthenium is not oxidised directly in the surface of the electrode; thus the wide oxidation peak is not presented. In blue line a meager increase of current is observed due to a cramped distance L1 in contrast in the case of XL-C electrode.

**Table 2.2:** Different L1 values of each electrode

Electrodes name	L1 thickness ( $\mu$ m)	Total thickness ( $\mu$ m)
CT-AD	0	6
XL-A	2.7	6
XL-C	3.75	6

By suitably choosing such factors, and the coreactant (TPA) concentration, a narrow control over the intensity and the ECL vertical profile may be achieved, spatially confining the emission more or less close to the TiO<sub>2</sub> outer surface. The proper selection of the above intrinsic (i.e., structural) and extrinsic (i.e., chemical) parameters will have important impact on the resolving power of the imaging tool: (a) thick emitting layers (large L2) located at short distance from the TCO electrode (small L1), and large TPA concentrations will in general produce a very intense ECL emission from the entire Ru@TiO<sub>2</sub> layer suitable, e.g., to obtain clear and low resolution shadow images of relatively large objects while (b) small objects, like, e.g., subcellular components, would instead be better resolved by a relatively fainter but more focused radiation coming from a thin emitting layer (small L2) located at larger distances from the TCO electrode (large L1) (and with low TPA concentrations). Fine tuning of the

resolutive power for all intermediate cases would in general be obtained by suitable choice of the L1, L2 and [TPA] parameters.

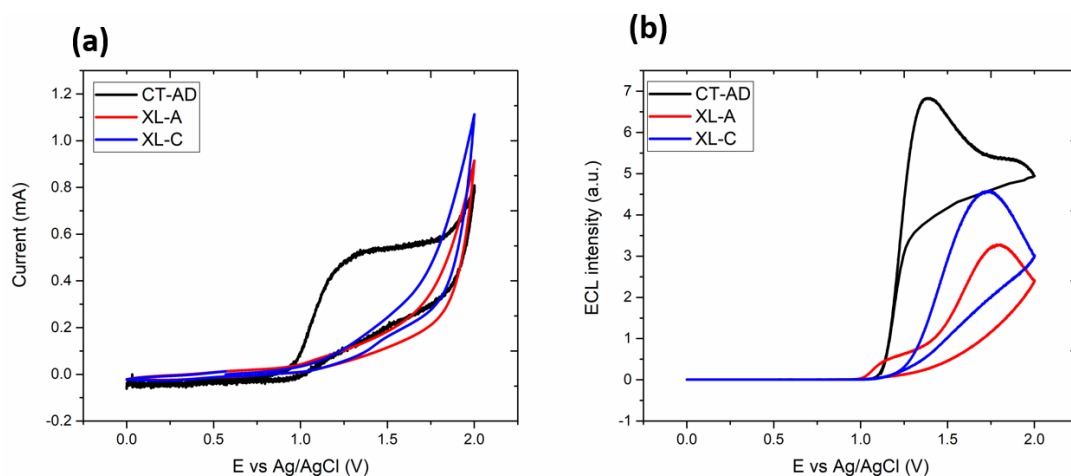


**Figure 2.10:** (a) Electrochemical behaviour of 3D nanostructured electrodes (b) ECL response as a function of the L1 structural parameter (ECL-potential curves in 180 mM TPA in 0.2 M PB solution,  $\text{TiO}_2$  film thickness:  $6\ \mu\text{m}$ ); Reference electrode Ag/AgCl (V), PMT bias of 750 V; amplification 00.0 $\mu\text{A}$ .

The resulting 3D nanostructured electrodes were also checked for their ECL properties, shown in Figure 2.10b, which highlighted interesting effects on both ECL intensity ECL generation dynamics obtained by modification of the structural characteristics of the 3D nanostructured  $\text{TiO}_2$  film, and in particular of thickness of the Ru-bearing layer and its position with respect to the TCO electrode.

Analytically, when the ruthenium complex is located closer to the FTO's surface ( $L1=0\ \mu\text{m}$ ), the electron transfer between the electrode's surface and the luminophorous is getting higher and a strong ECL emission with a width peak is presented in +1.2V (figure 2.9a). A second weak peak is presented at +1.8V, when the ruthenium complex is located far away from the FTO's surface ( $L1= 3.75\ \mu\text{m}$ ), such in this phenomenon occurs both mechanisms which are presented in figure 2.9a,c.

In both presented peaks TPA and ruthenium can be oxidised but in the second peak only TPA can do that. In the second case, TPA can produce continuously radical which can trigger the "remote ECL mechanism". Based on this theory, CT-AD electrode presents a strong ECL Emission only in +1.2V; as follows, a sickly peak at +1.8V verify the presence of the ECL remote mechanism. On the other hand, XL-A and XL-C nanostructured electrodes, obtains a strong ECL emission at +1.8V which means that only TPA is oxidised on the surface and at the same time triggers the ECL remote mechanism. Only in XL-A electrode case is displayed a weak peak at +1.2V something which means that the mechanism in figure 2.9a also occurs.

## 2.3 Conclusions

In summary, we tested three different Mox/FTO 3D nanostructured electrodes for ECL applications. Our method exploits the investigation of alternative electrode materials for the substitution of the commercial ones. Initially, such the thickness of the films as the nature of material have been checked. By combining the commercially available paste of TiO<sub>2</sub> with the opaque one the ECL signal was enhanced than the pure TiO<sub>2</sub> or ZrO<sub>2</sub> nanostructured electrodes. In homogeneous phase the TAO electrode presented the highest ECL emission and by choosing of this Mox material, the distance between luminophores and FTO surface has been also tested. This approach may be performed in an extremely simple controllable way; therefore, the ruthenium may have a distance of 0-3.75 μm from the FTO's surface. In every case where the ECL behavior changes, such ruthenium can be oxidized on the electrode's surface and triggered by the TPA radicals. In this case we can obtain two ECL mechanisms in the same system by only changing the distance of the luminophores. Indeed, we achieved the replacement of commercial electrodes and at the same time the investigation of both mechanisms at once. Ongoing research is going to be performed in our laboratories for other luminophores' distances and the application of this system for the development of an ECL sensor.

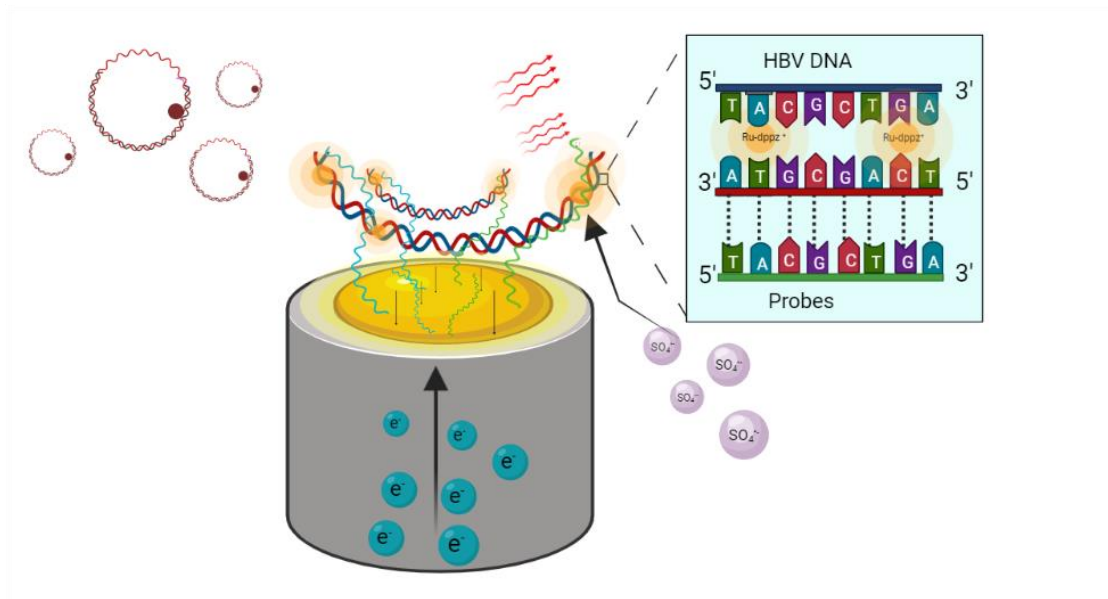
## References

- [1] M. Abdullah et al. *Renew. Sustain. Energy Rev.* 76 (2017) 212–225.
- [2] Y. Liu et al. *Appl. Phys. A Mater. Sci. Process.* 102 (2011) 127–130.
- [3] I. Paramasivam et al, *Small.* 8 (2012) 3073–3103.
- [4] Y. Jun et al. *Chem. Commun.* 48 (2012) 6456–6471.
- [5] K. Huo et al. *RSC Adv.* 4 (2014) 17300–17324.
- [6] H. Jen et al. *Appl. Mater. Interfaces.* (2013) 0–6.
- [7] K. Shankar et al. *Nano Lett.* 8 (2008) 1654–1659.
- [8] D. Wang et al. *Chem. Mater.* 21 (2009) 1198–1206.
- [9] C.Y. Tian et al. *Chem. Commun.* 48 (2012) 8234–8236.
- [10] C.Y. Tian et al. *Analyst.* 137 (2012) 3070–3075.
- [11] J. Li et al. *Anal. Chem.* 82 (2010) 7357–7361.
- [12] N.M. Ravindra et al. *Infrared Phys. Technol.* 50 (2007) 21–29.
- [13] S.K. Tripathy *Opt. Mater.* 46 (2015) 240–246.
- [14] W.R. Frensley et al. *Phys. Rev. B.* 16 (1977) 2642–2652.

- [15] R.J. Elliott *Phys. Rev.* 96 (1954) 266–279.
- [16] H. Hsu *Proc. IEEE.* 51 (1963) 359.
- [17] M.A. Correa-Duarte et al. *Chem. Phys. Lett.* 286 (1998) 497–501.
- [18] S. Chaudhuri et al. *J. Phys. Chem. A.* 119 (2015) 4162–4169.
- [19] B.L. Smith et al. *Solid State Electron.* 14 (1971) 71–75.
- [20] F. Odobel et al. *Acc. Chem. Res.* 43 (2010) 1063–1071.
- [21] A. Ur Rehman et al. *Sci. World J.* 2013 (2013).
- [22] Lay-Lay Chua et al. *Nature.* 434 (2005) 192–194.
- [23] H.J. Kim et al. *Sensors Actuators, B Chem.* 192 (2014) 607–627.
- [24] V.D.B.C. Dasireddy et al. *J. Taiwan Inst. Chem. Eng.* 82 (2018) 331–341.
- [25] P. Nikolaou et al. *Mater. Chem. Front.* 2 (2018) 730–740.
- [26] W.M. Campbell et al. *Coord. Chem. Rev.* 248 (2004) 1363–1379.
- [27] Z. Li, Z.J. Yao et al. *Int. J. Hydrogen Energy.* 43 (2018) 21114–21132.
- [28] J.S. Chen et al. *Mater. Today.* 15 (2012) 246–254.
- [29] H. Gao et al., *Chem. Eng. Technol.* 32 (2009) 867–872.
- [30] Z. Zhao et al. *J. Phys. Condens. Matter.* 22 (2010).
- [31] Z. Zhao et al. *J. Phys. D. Appl. Phys.* 41 (2008).
- [32] H.G. Yang et al. *J. Am. Chem. Soc.* 131 (2009) 4078–4083.
- [33] X. Pang et al. *Biosens. Bioelectron.* 91 (2017) 456–464.
- [34] L. Yang et al. *Biosens. Bioelectron.* 142 (2019) 111487.
- [35] J. Shu et al. *ACS Appl. Mater. Interfaces.* 7 (2015) 23812–23818.
- [36] X. Liu et al. *Electrochim. Acta.* 242 (2017) 327–336.
- [37] P. Da et al. *Anal. Chem.* 86 (2014) 6633–6639.
- [38] R. Zhang et al. *Anal. Chem.* 91 (2019) 3681–3686.
- [39] Y. Zhou et al. *Anal. Chem.* 89 (2017) 3732–3738.
- [40] Y. Tang et al. *Nanoscale.* 11 (2019) 9115–9124.
- [41] H. Dai et al. *Chem. Commun.* 51 (2015) 7697–7700.
- [42] N. Liu et al. *New J. Chem.* 41 (2017) 3380–3386.
- [43] P. Dai et al. *Anal. Chem.* 87 (2015) 12372–12379.
- [44] M. Sentic et al. *Chem. Sci.* 5 (2014) 2568–2572.
- [45] S. Voci et al. *Anal. Bioanal. Chem.* 412 (2020) 4067–4075.

- [46] P. Papaspyridakos et al. *J. Prosthetic Dentistry* 100 (2008) 165- 172.
- [47] M.H. Habibi et al. *Corros. Sci.* 75 (2013).
- [48] S. López-Romero et al. *World J Condens. Matter Phys.* 3 (2013) 173.
- [49] J.D. Fidelus et al. *IEEE Sensors* 9 (2013) 1268.
- [50] W. Reiter et al. U.S. Patent No. 2016/0161441 A1. Washington, DC: U.S. Patent and Trademark Ofce (2016).

# CHAPTER 3



**Can we develop an ultra-sensitive biosensor without any sequence and/or signal amplification?**



### 3.1 Introduction

The detection of nucleic acids is nowadays of extreme importance in many medical fields for early and accurate diagnosis, personalized therapy, and preventive screening. In this context, DNA identification and quantification through molecular methods provides relevant clinical advantages with respect to the traditional laboratory methods, such as bacterial cultures or antibody detection, being much faster (hours versus days for bacterial cultures), specific (allowing the detection of genotypes), sensitive (few copies of pathogens in a sample) and accurate (able to detect different microorganisms through the specific molecular markers, but also their vitality through the mRNA monitoring).

However, molecular methods typically need an amplification step achieved through the well-known Polymerase Chain Reaction (PCR) that is intrinsically quite laborious because it involves a multi-step and expensive process (about \$15–80 per sample) thus limiting its utilization to specialized laboratories [1].

Therefore, although current PCR-based methods are well-established and consolidated, they are not suitable to be used by unskilled personnel near the patient at competitive costs. This represents a strong limitation for its massive use, limiting the potential of genome analysis for human health. This is proved by the diffused difficulty to perform massive and real time diagnosis of coronavirus disease 2019 (COVID-19) for prompt infection management and prevention which is stimulating new approaches and methodologies for molecular detection [2–4]. In addition, it has become evident that COVID-19 antigen rapid diagnostic tests, although being fast and relatively cheap, yield a high percentage of false negative results. Therefore, the development of new molecular methods allowing rapid, sensitive, and simple detection of pathogens would be a significant breakthrough in molecular diagnostics opening new technological frontiers in the genome detection, as represented by the Genetic Point of Care (G-PoC) testing [5][6]. G-PoC sensors indeed would present some unique advantages, such as a simple operation (performable by untrained personnel), rapid results, low power supply and use of reagents, and convenience of use specifically in areas where resources are limited [7] (Figure 3.1).

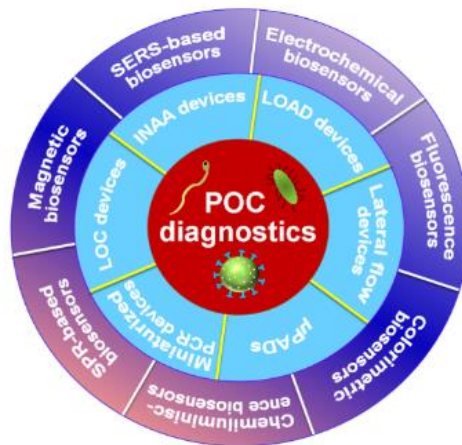


**Figure 3.1:** Schematic illustration of point-of-care diagnostics for infectious diseases. With the permission of [6].

In this scenario, PCR-free approaches are extremely appealing because they do not require any analyte-amplification reactions significantly simplifying the instrumentation needed and thus lowering costs. However, these approaches are extremely challenging since detection of whole genome sequences has to be achieved at lower concentrations. This is particularly true in the case of infectious diseases where the concentration of bacterial or viral genome can be few copies in few microliters of sample. For these reasons, only very few examples of PCR-free methods have been reported in the literature so far and, consequently, a limited number of devices has been proposed [8]. Furthermore, most of them use indirect strategies that target analytes different from the chased viral or bacterial genomes [9] and, in case of pathogens, they do not fulfil the Limit of Detection (LoD) requirements (10 copies of target-genome/reaction) [10] or use complex instrumentation [11]. Additionally, all the reported methods need pre-treatment or labelling of the sample, adding a further degree of complexity.

### 3.1.1 Hepatitis B Virus (HBV)

Hepatitis B type Virus (HBV) is a blood borne pathogen that causes hepatitis, liver cirrhosis and hepatocellular carcinoma (HCC). According to world health organization (WHO) in 2015 has been estimated 257 million people where living with chronic HBV infection and that 887.000 deaths yearly are caused by the subsequent occurrence of HCC [12]. HBV in one of the few viruses known to be involved in a human cancer. HBV belongs to the group of animal viruses known as the *hepadna viridae*. The other members of this group are the woodchuck hepatitis virus (WHV)[13], the beechey ground squirrel hepatitis virus (GSHV) [14] and the Pekin duck hepatitis B virus (DHBV) [15]. All these viruses have a common structure. They are mainly hepatotropic and lead to persistent virus infection. Only HBV and WHV cause chronic active hepatitis and HCC.

The structure of HBV contains a host-delivered lipid full of surface proteins and an inner protein capsid that contains the genome of HBV (figure 3.2). The capsid is a polypeptide chain with a molecular weight 20kDa [16]. The HBV genome encodes four partially overlapped open reading frames (ORF): the surface (preS1, preS2, S), core (75onvers, core), polymerase and the 'x' genes, respectively. High genetic variability is a characteristic feature of the HBV 's'the viral polymerase lacks proof-reading activity and uses an RNA intermediate during its replication [17].

According to Sakai [18], hepatitis B virus is made up of three different structures: the Dane (42 nm), filamentous (22 nm) and spherical (20 nm) particles which are often observed in serum of HBV-infected patients. All the three particles possessed a similar hepatitis B surface antigen (HbsAg) on their surface. However, added that the filamentous and spherical particles are non-infectious because even though both possessed HbsAg and host-derived lipids, they are without HBV genomes. This further reveals that the Dane particle; a 42 nm sphere is the complete infectious HBV virion with its core region being small, partially double stranded, circular DNA molecule and viral DNA polymerase that is surrounded by nucleocapsid [19].

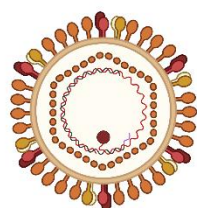


**Figure 3.2:** Structure of Hepatitis B Virus.

The mode of transmission of the disease is largely through unprotected sex, mother-to-child transmission (MTCT), contaminated blood and blood products and use of contaminated objects or instruments [20]. Maternal HBV transmission is a risk factor in the development of liver cirrhosis and hepatocellular carcinoma among young adults [21]. This means that infancy-related HBV infections that often result to chronic cases usually lead to liver cirrhosis and hepatocellular carcinoma; thus prompting the need for urgent prevention of mother to child transmission. Therefore, is necessary the development of sensitive, rapid and simple methods for the determination of HBV genome and proteins.

### **3.1.1.1 PCR and PCR-free methods for the diagnosis of HBV**

Particularly interesting and studied are the biosensors aimed at the detection of DNA thanks to its versatility and various functions. First, the DNA contains the genetic

information of an organism for this is a biomarker for medical diagnosis, in addition, the use of aptamers, nucleic acids capable of binding to specific molecules, has extended the recognition also of proteins, ions, etc., finally some types of DNA have a catalytic function, therefore they can be exploited for the quantification of metal ions. In this context, DNA represents an ideal building block for applications in biosensor especially for the additional advantages that this show:

- are very stable and flexible,
- DNA is easy to synthesize and modify with some functional groups it also possesses a conformation that can change according to external conditions
- By exploiting the basic-pairing rules it is easy to know its secondary structure

The new DNA recognition devices have provided revolutionary improvements for human health allowing the development of innovative and useful methods for diagnosis in addition to personalized therapies that are now crucial in pharmaceuticals, clinical diagnostics and forensic [26]. Research, therefore, is active in the development of the so-called “genetic Point-of-Care” device (G-PoC) “identified by the National Institute of Health (NIH) as one of the highest priorities for the diagnosis of viral infections. G-PoC devices would have a relevant impact around the world by helping decentralization of diagnostic locations hospital laboratories to medical offices. This would allow for massive diagnostic screening and better ways of dealing with pandemic threats. Based on these considerations, multidisciplinary research groups from around the world are active in the development of technologies innovative and novel chemical strategies for the detection of viral pathogens such as Hepatitis B virus (HBV)[10]. For example, microRNAs (miRNAs), small fragments of RNA (approximately 22 nucleotides) non-coding that control gene expression at the post-transcriptional level, can be used for the construction of hybridization probes combinable with different methods of detection in order to obtain biosensors also used for the diagnosis of Hepatitis B virus (HBV). In fact, human miRNAs have been shown to originate as a defense mechanism immune against viral infections [27]. All devices currently available for the quantification of the HBV viral genome are based on the amplification of the analyte target, exploiting the Polymerase Chain Reaction (PCR) or the generated signal [28]. However, the recognition of a viral genome at the interface between an electrode and a solution shows additional benefits due to easy integration with miniaturized devices, reduced analysis times, lower costs[10] and superior sensitivity to PCR.

### **3.1.2 Sars-CoV-2 (COVID-19)**

SARS-CoV-2 is a betacoronavirus responsible for the COVID-19 pandemic. Although the SARS-CoV-2 genome was reported recently, its transcriptomic architecture is

unknown. Utilizing two complementary sequencing techniques, we present a high-resolution map of the SARS-CoV-2 transcriptome and epitranscriptome. DNA nanoball sequencing shows that the transcriptome is highly complex owing to numerous discontinuous transcription events. In addition to the canonical genomic and 9 subgenomic RNAs, SARS-CoV-2 produces transcripts encoding unknown ORFs with fusion, deletion, and/or frameshift. Using nanopore direct RNA sequencing, we further find at least 41 RNA modification sites on viral transcripts, with the most frequent motif, AAGAA. Modified RNAs have shorter poly(A) tails than unmodified RNAs, suggesting a link between the modification and the 3' tail. Functional investigation of the unknown transcripts and RNA modifications discovered in this study will open new directions to our understanding of the life cycle and pathogenicity of SARS-CoV-2. Like other coronaviruses (order Nidovirales, family Coronaviridae, subfamily *Coronavirinae*), SARS-CoV-2 is an enveloped virus with a positive-sense, single-stranded RNA genome of ~30 kb. SARS-CoV-2 belongs to the genus betacoronavirus, together with SARS-CoV and Middle East respiratory syndrome coronavirus (MERS-CoV) (with 80% and 50% homology, respectively) [22],[23] Coronaviruses (CoVs) were thought to primarily cause enzootic infections in birds and mammals. However, the recurring outbreaks of SARS, MERS, and now COVID-19 have clearly demonstrated the remarkable ability of CoVs to cross species barriers and transmit between humans[24].

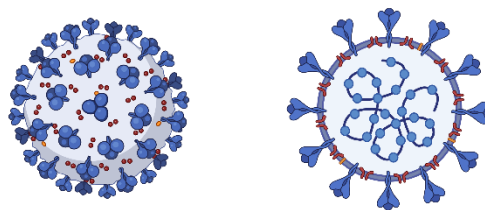


**Figure 3.3:** Sars-CoV-2 structure.

Among RNA viruses, CoVs have some of the largest genomes (26-32kb) each viral transcript has a 5'-cap structure and a 3' poly(A) tail [25]. The genomic RNA (gRNA). Is packaged by the structural proteins to assemble progeny virions. Shorter sgRNAs encode conserved structural proteins (spike protein [S], envelope protein [E], membrane protein [M], and nucleocapsid protein [N]), and several accessory proteins (figure 3.3). SARS-CoV-2 is known to have at least six accessory proteins (3a, 6, 7a, 7b, 8, and 10) according to the current annotation (GenBank: NC\_045512.2).

### 3.1.3 Polymerase Chain Reaction (PCR)

The technique mainly used for the quantification of a viral genome is the Polymerase Chain Reaction (PCR) which is based on the amplification of specific regions of the genome of the patient in which there is information on the viral agent, specifically, currently the so-called end point PCR (CAHBM) is exploited which, however, shows limited intervals dynamic thus influencing the quantification of moderate and high viral levels [29]. Innovative methods for the quantification of nucleic acids they are based on Real-time PCR and show high wider sensitivity and dynamic ranges. The common goal of all methodologies so far developed concerns the improvement of the extraction phase of the viral genome from the samples biological and preparation of the samples themselves, usually difficult phases from the point of technical point of view as well as being potential causes of variability and contamination. In such a scenario, the demand for automated methods for sample preparation is growing strongly to quantify nucleic acids as accurately as possible by increasing their more and more diffusion in the clinical field. The problem related to Hepatitis infections is so strong B virus (HBV), specific methods based on Real-time PCR have been developed aimed at quantification of this analyte which can be compared with the technique currently used based on end point PCR (CAHBM). The CAHBM system provides for extraction manual of the HBV viral genome from plasma samples and the amplification of the region 78onvers or core of the virus specific gene useful for quantification. The sensitivity of this methodology is 200 copies / mL (74 international units / mL) with a linear range greater than 200,000 copies / mL (for this system there is 78onversionn factor of 2.7 copies / IU) [30]. Among other optimized technologies, of particular interest is Real time PCR fully automated and based on the use of TaqMan (CAP-CTM; Roche Molecular Systems, Inc., Branchburg, NJ) which can be correlated, by linear regression, with the classic procedure just described (CAHBM) for the evaluation of the change of the viral load in HbsAg positive patients with chronic hepatitis. From the analyzes carried out, it is possible to state that in patients with chronic Hepatitis B virus (HBV), the CAP-CTM is more sensitive than CAHBM managing to detect 10% more of virus. Therefore, the development of increasingly accurate methods based on Real-time PCR, rapid and sensitive would ensure confirmation of the effectiveness of antiviral therapies developed for those patients suffering from chronic and specific forms of Hepatitis B virus (HBV).

#### 3.1.3.1 Polymerase chain reaction free (PCR free)

Recently, an intriguing PCR-free method has been introduced in this context for quantification of the entire genome of Hepatitis B virus (HBV) on the surface of an electrode. Systems developed for the recognition of single-stranded DNA (ssDNA) or double-stranded DNA (ds-DNA) occurs from individual and specific strands of a portion of the genome viral guaranteeing the formation of structures, respectively, duplex

DNA or triplex DNA. In Figure 3.4 shows a representation of the formation of a triplex DNA structure [31]. This strategy can be combined with several transduction methods:

- UV-visible spectrophotometry, measures the intensity of light
- Capacitive, measures the Cdl capacity
- Piezoelectric, measures the change in mass
- Electrochemistry, measures the electric current

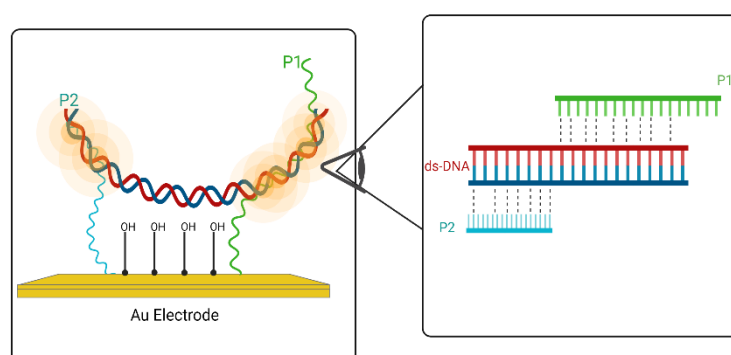


**Figure 3.4:** Molecular interaction between the duplex structure of HBV DNA and two specific Probes P1 and P2.

## 3.2 Electrochemical platform preparation for HBV whole genome detection

Gold electrodes were polished with 0.3 and 0.05  $\mu\text{m}$  alumina slurry in order to obtain a mirror surface and then washed by sonication in a 50:50 ethanol and deionized water for 5 min. Furthermore, electrodes were cleaned electrochemically through cyclic voltammetry in 0.5 M  $\text{H}_2\text{SO}_4$  scanning from  $-1$  to  $1$  V (10 scans and  $0.1 \text{ V s}^{-1}$ ). Finally, they were dried with Ar gas. Next, P1 and P2 thiol 5'-terminated probes were dissolved in PBS 0.01 M (pH 7.4) buffer at a concentration of  $10 \mu\text{M}$  and immobilized on the surface according to the following procedure: electrodes were kept at "Room Temperature (RT)" for 4 h immersed in the solution containing the thiol-terminated probes (figure 3.5a). Afterwards, they were gently washed with PBS 0.01 M (pH 7.4) followed by an overnight blocking procedure with  $10 \mu\text{M}$  of  $\text{C}_6\text{H}_{14}\text{OS}$  dissolved in PBS

0.01 M (pH 7.4) to stabilize the assembled layer of P1 and P2 specific probes (figure 3.5b). Synthetic HBV genome (SG ds-HBV) samples (1, 5, 10, 100, 1000, 10000 cps  $\mu\text{L}^{-1}$ ) were prepared by diluting the starting clone solution ( $10^6$  cps  $\mu\text{L}^{-1}$ ) in PBS 0.01 M at pH 5.5. P1/P2 modified electrodes were immersed in 1 mL of SG ds-HBV solutions at 50 °C in a chamber for 3 h (figure3.5c). To intercalate  $[\text{Ru}(\text{phen})_2\text{dppz}]^{2+}$  in the anchored HBV genome, electrodes were immersed in a solution containing 14  $\mu\text{M}$  of  $[\text{Ru}(\text{phen})_2\text{dppz}]^{2+}$  in PBS 0.01M at pH 5.5 and incubated for 2 h until the intercalation was completed (figure3.5d).

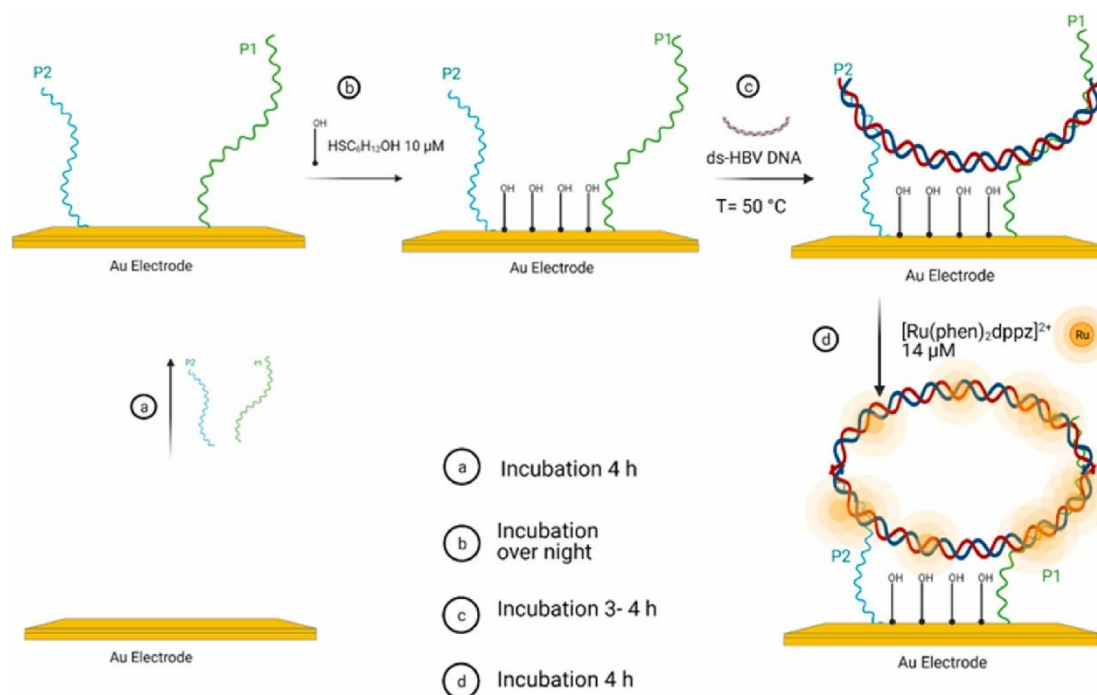


**Figure 3.5:** Scheme of ECL-PCR-free strategy: (a) Immobilization of specific probes P1 and P2 and of (b) 6-Mercapto-1-hexanol on the surface of a gold electrode; (c) recognition of ds-HBV by surface cooperative hybridization and (d) intercalation of  $[\text{Ru}(\text{phen})_2\text{dppz}]^{2+}$  and HBV whole genome detection.

### 3.2.1 Analytical procedure

After the preparation of the electrochemical platform the Au electrode was then ready for the ECL procedure. The electrochemical cell was fixed in front of a Photomultiplier (PMT) tube in order to always keep a 0.5 cm space between the cell and the PMT input window. The transparent nature of the cell allows the photocurrent emission, produced by  $[\text{Ru}(\text{phen})_2\text{dppz}]^{2+}$  complex, to be detected and amplified by the PMT tube. For real sample analysis, 0–0.75 copies  $\mu\text{L}^{-1}$  of EG ds-HBV (extracted from real samples) diluted in PBS pH 5.5 from the starting solution ( $12 \times 10^3$  IU/mL) were used. For the biological fluid simulation testing, SG ds-HBV ( $10^6$  cps  $\mu\text{L}^{-1}$ ) has been diluted into 1 mL Fetal Bovine Serum (FBS) to a final concentration of 100, 1000 and 10000 cps  $\mu\text{L}^{-1}$ , then the modified P1/P2 electrodes were immersed in these solutions, and



we repeated the same procedure as it is described above. Standard deviations were obtained by repeating the experiment with 5 independent samples.

### 3.3 Thermodynamic studies

The typical surface hybridization implies specific interactions, leading to a thermodynamic equilibrium between hybridized and unhybridized DNA, of immobilized single strain DNA probe with the target DNA. In the case of cooperative hybridization, instead, two NA probes (P1 and P2) – designed to recognize specific and different sequences on both parallel and anti-parallel strands of the ds-HBV – were immobilized on a gold electrode surface (figure 3.5b). The ds-HBV DNA is recognized by the two surface probes that independently hybridize two complementary filaments of the ds-HBV DNA and anchor it on the electrode surface. This leads to an effective DNA recognition reaction endowed with higher affinity, as confirmed by the comparison of the two individual probes performances.

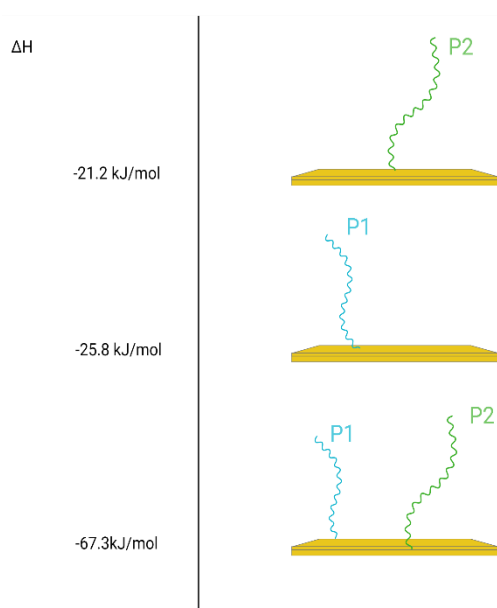


**Figure 3.6:** Enthalpy energy for each immobilized probe.

This leads to an effective DNA recognition reaction endowed with higher affinity, as confirmed by the comparison of the two individual probes performances (figure 3.6) and by a previous molecular dynamic investigation showing higher binding enthalpy for ds-HBV DNA – P1/P2 interaction ( $-67.3 \text{ kJ mol}^{-1}$ ) than the sum of the individual single probes interactions ( $-47.0 \text{ kJ mol}^{-1}$ )[26]. This theory has also confirmed. A sequence gap in the target of 138 bps between the two regions recognized by the two probes was proved to be effective in minimizing the steric hindrance. To confirm this theory, we perform additional ECL experiment for both probes (P1/P2) and for each

case separately. As it is presented in figure 3.7, only when two probes are immobilized onto Au electrode our system obtains the higher ECL intensity. On the other point of view, if the sum of ECL intensity of these two probes is higher that the ECL intensity of an individual measurement.

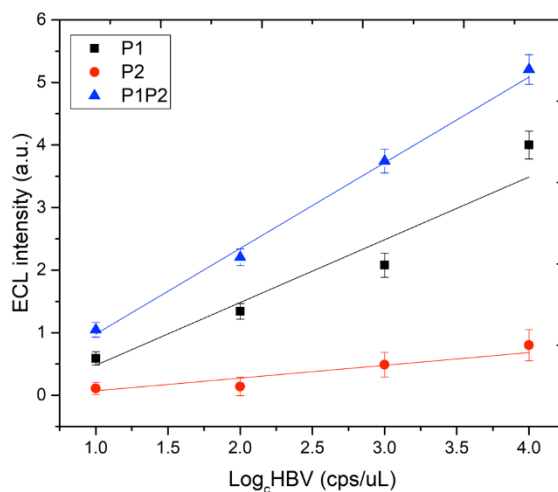


**Figure 3.7:** Correlation between P1 and P2 probes. ECL intensity vs Log<sub>10</sub> HBV concentration of HBV (10-10000 cps/μL), using: P1 probe (black line/spots), P2 probes (red line/spots), and combination of P1P2 (blue line/spots); in PBS 0.1 M, 14μM intercalated [Ru(phen)<sub>2</sub>dppz]<sup>2+</sup> and 50 mM K<sub>2</sub>S<sub>2</sub>O<sub>8</sub>. Working Au electrode with P1 and P2 formation vs Ag/AgCl reference electrode with scan rate 0.3 V s<sup>-1</sup>. PMT bias of 750V.

### 3.3.1 Surface electrochemical characterisation using electrochemistry

The first part of this work was focused on the optimization of the chemical treatment of the surface of gold electrode for the effective anchoring of P1 and P2 probes. The surface of the electrode which was used for the ECL biosensing was characterized by Electrochemical Impedance Spectroscopy (EIS). Figure 3.8 demonstrates the Nyquist plots of the EIS collected with a unique electrode in 5 mM [Fe(CN)<sub>6</sub>]<sup>3-/4-</sup>. An equivalent circuit system (inset in figure 3.8) was used to fit the experimental EIS results. This circuit contains the ohmic resistance of electrolyte (R1), the Warburg impedance (Wd2), the charge-transfer resistance (R2), and the double layer capacitance (Q2). The fitting shows that the simulated line (dots) is in good agreement with the experimental impedance data (solid lines), as demonstrated in the selected circuit. In figure 3.8 is represented the bare gold electrode which exhibits a low charge electron transfer resistance with a value of 4.7 kΩ cm<sup>-2</sup> (figure 3.8 line a). After probes immobilization, a blocking step was performed in order to ensure a good stability of the probes and, at the same time, increasing the resistance of the double layer[10]. EIS analysis showed an increased resistance R2 (8.8 kΩ cm<sup>-2</sup>, figure 3.8 line b) after the immobilization of the P1 and P2 probes. This is probably a result of the electrostatic

repulsion between the negatively charged DNA and the redox mediator.[32] The blocking procedure and the thiol deposition on the electrode surface, further increased the resistance (to  $12.6 \text{ k}\Omega \text{ cm}^{-2}$ ) as a result of the double layer created by thiols which hinder the electron transfer (figure 3.8 line c). Moreover, also the value of the double layer capacitance Q2 increased in all these three steps, since more molecules were deposited in the surface of the gold electrode, as it is presented in table T3.1.

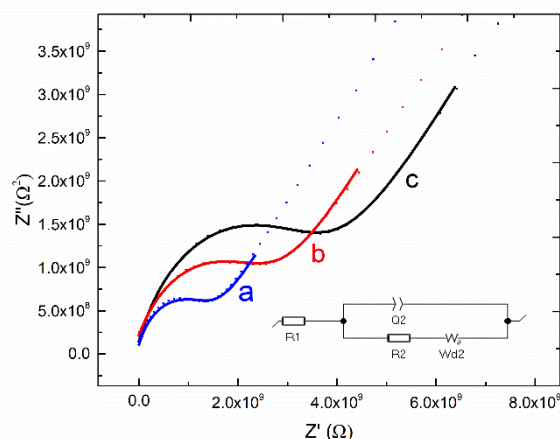


**Figure 3.8:** EIS of (a) bare gold electrode (b) gold electrode with immobilized P1 and P2 and (c) gold electrode with immobilized P1, P2 and thiol immersed in a solution containing  $5.0 \text{ mM } [\text{Fe}(\text{CN})_6]^{3-/4-}$ .

**Table T3.1:** Modified electrodes with different values of charge-transfer resistance (R2) and double-layer capacitance (Q2).

Electrodes	R2 ( $\text{k}\Omega \text{ cm}^{-2}$ )	Q2 ( $\mu\text{F cm}^{-2}$ )
Au	4.7	82.7
Au_P1P2	8.8	140.3
Au_P1P2_tiol	12.6	166.1

### 3.3.2 Detection of whole synthetic genome of HBV

To detect the whole genome recognition event occurring at the electrode surface, an ECL-active complex –  $[\text{Ru}(\text{phen})_2\text{dppz}]^{2+}$  – was used as efficient intercalating dye in the final step of our PCR-free detection strategy. Intercalation methods are appealing since they do not require any extra chemical labelling step of target or probes[33],[34]; in addition, since hundreds of complexes can intercalate in the whole viral genome, a strong signal amplification can be obtained. Moreover,  $[\text{Ru}(\text{phen})_2\text{dppz}]^{2+}$  shows an intense luminescence at 600–650 nm when intercalated with a double-strand DNA genome[35],[36], while in aqueous solution the emission is dramatically quenched, increasing even more the signal-to-noise ratio. This behaviour

results from a differential population of two close-lying dppz-localized excited states, the non-emissive state being favoured in polar and H-bonding solvents[37]. Therefore, once  $[\text{Ru}(\text{phen})_2\text{dppz}]^{2+}$  was intercalated to the HBV-SG anchored at the electrode surface, light emission at 600–650 nm was recorded at  $-0.8$  V (figure 3.9), upon (vs Ag/AgCl reference electrode), *i.e.* upon the reduction of the  $\text{S}_2\text{O}_8^{2-}$  coreactant which ignites the ECL process.

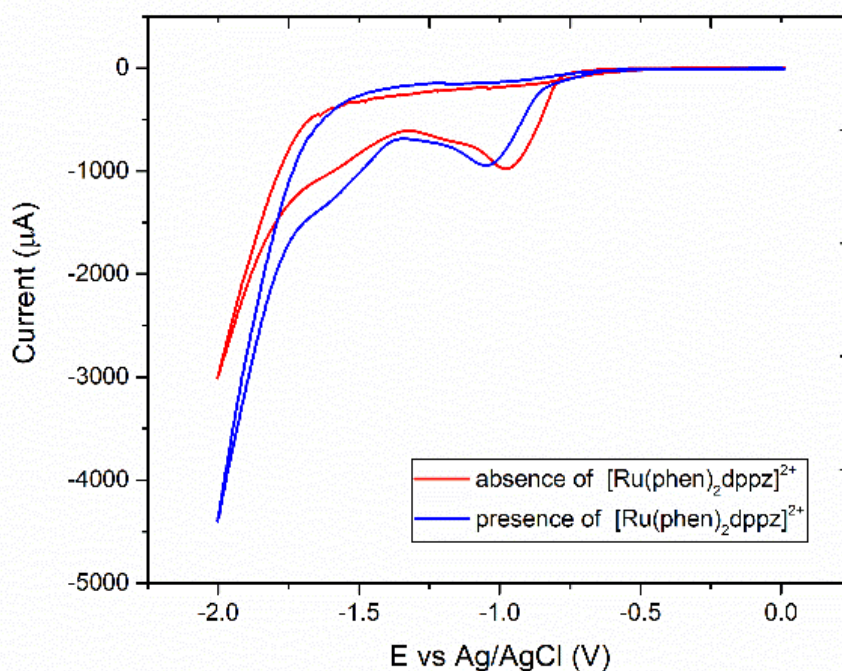


**Figure 3.9:** Current vs potential for SG ds-HBV ( $100 \text{ cps } \mu\text{L}^{-1}$ ) in absence (red line) and presence (blue line) of  $14 \mu\text{M}$  intercalated  $[\text{Ru}(\text{phen})_2\text{dppz}]^{2+}$ , in  $50 \text{ mM K}_2\text{S}_2\text{O}_8$  in PBS  $0.1 \text{ M}$ . Working Au electrode with P1 and P2 formation vs Ag/AgCl reference electrode with scan rate  $0.3 \text{ V s}^{-1}$ . PMT bias of  $750 \text{ V}$ .

Figure 3.10a reports the ECL intensities vs electrode potential measured in SG ds-HBV solutions at different concentrations ( $0$ – $10000 \text{ cps } \mu\text{L}^{-1}$ ). Figure 3.10a suggests a logarithmic dependence of ECL intensities on HBV genome concentration and a recordable signal is still detected with few copies of HBV genome ( $5 \text{ cps } \mu\text{L}^{-1}$ ), noteworthy without any analyte-amplification process. To assess the analytical performance of the method, ECL intensity vs the logarithm of the ds-HBV concentration was plotted. Figure 3.10b displays a good linear behavior in the  $5$  and  $10000 \text{ cps } \mu\text{L}^{-1}$  range with a correlation coefficient of  $0.987$  with a good reproducibility; thus, the increase of the cathodic current held at  $-0.8 \text{ V}$  with and without the presence of  $[\text{Ru}(\text{phen})_2\text{dppz}]^{2+}$  (see figure 3.9). The calculated LoD ( $S/N = 3.3$ ) was  $2.4 \text{ cps } \mu\text{L}^{-1}$  (*i.e.*  $4.5 \text{ aM}$ ) with a sensitivity (slope of the curve) of  $1.35 \text{ a.u./decade}$ .

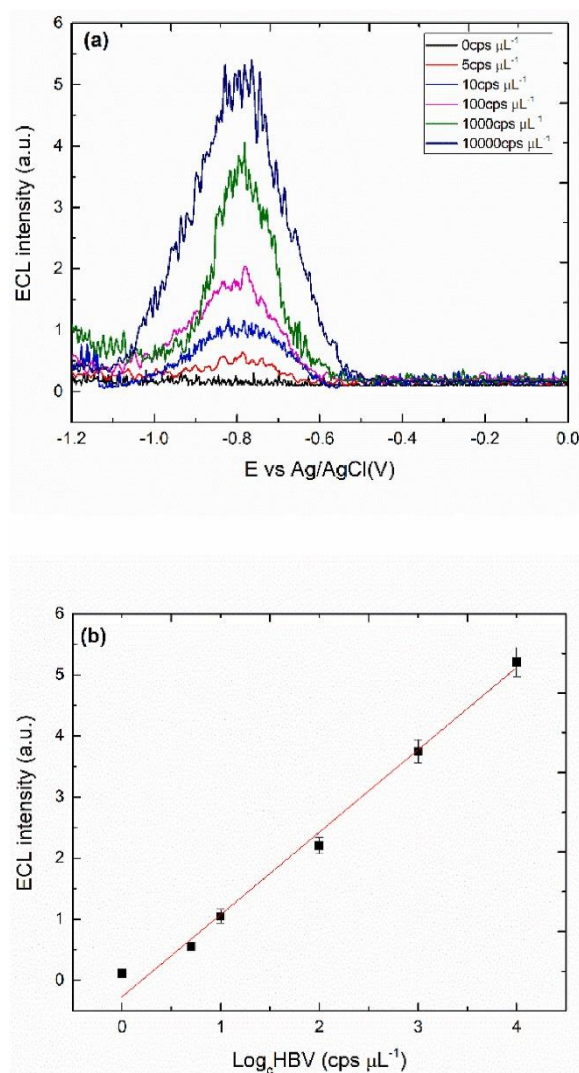


**Figure 3.10:** (a) ECL intensity vs potential for different SG ds-HBV concentrations (0–10000 cps  $\mu\text{L}^{-1}$ ), (b) Calibration plot analysis and dependence of the response of the electrode on concentration of SG ds-HBV with standard deviation of  $\pm 0.08$ – $0.32$ , in 50 mM  $\text{K}_2\text{S}_2\text{O}_8$  in PBS 0.1 M. Working Au electrode with P1 and P2 formation vs Ag/AgCl reference electrode with scan rate  $0.3 \text{ V s}^{-1}$ . PMT bias of 750 V. The error bar shows the standard deviation ( $n = 5$ ).

### 3.3.2.1 Detection of HBV Extracted genome

To further validate the high sensitivity of the method, extracted genome of HBV (EG ds-HBV) from real samples was used. Noteworthy, much lower concentrations than those tested for SG ds-HBV could be detected. Figure 3.11a reports the ECL curves obtained for EG ds-HBV at concentrations below  $0.75 \text{ cps } \mu\text{L}^{-1}$  and a signal was still detected at  $0.06 \text{ cps } \mu\text{L}^{-1}$ . The calibration curve shows a good linear correlation (figure 3.11b) with a LoD ( $S/N = 3.3$ ) of  $0.06 \text{ cps } \mu\text{L}^{-1}$  (i.e. 0.1 aM).

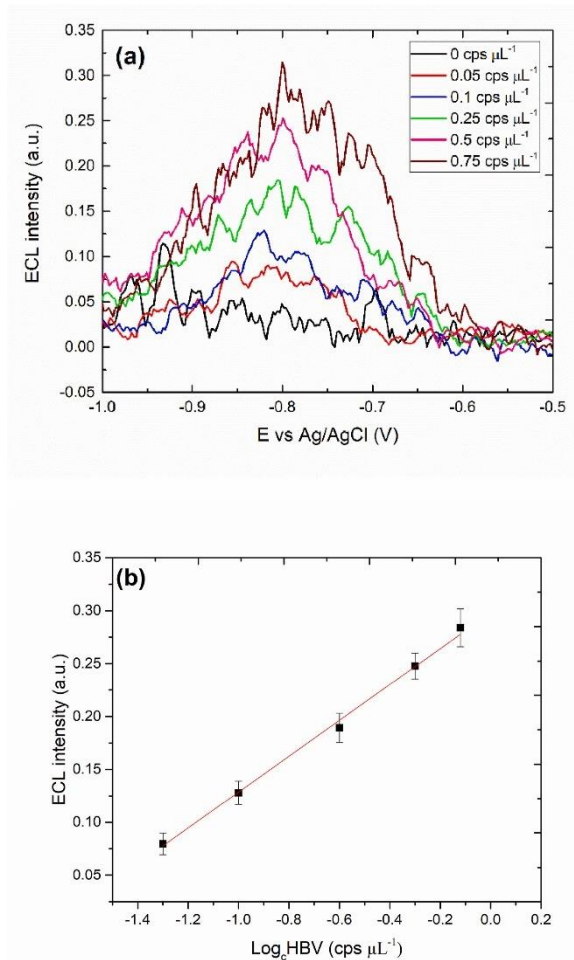


**Figure 3.11:** (a) ECL intensity vs potential for different concentration of EG ds-HBV (0–0.75 cps  $\mu\text{L}^{-1}$ ); (b) calibration curve of ECL intensity vs LogC HBV concentration with standard deviation of  $\pm 0.011$ – $0.017$ . In PBS 0.1 M, 14  $\mu\text{M}$  intercalated  $[\text{Ru}(\text{phen})_2\text{dppz}]^{2+}$  and 50 mM  $\text{K}_2\text{S}_2\text{O}_8$ . Working Au electrode with P1 and P2 formation vs Ag/AgCl reference electrode with scan rate  $0.3 \text{ V s}^{-1}$ . PMT bias of 750V. The error bar shows the standard deviation ( $n = 5$ ).

### 3.3.2.2 Analytical differences between extracted and synthetic genome of HBV

The different sensitivity between the synthetic (SG-dsHBV) (1.35 a.u./LogC) and the extracted real (EG-ds HBV) genomes (0.18 a.u./LogC) can be imputed to the different structure of the two macromolecules. Actually, the former consists of the HBV genome (3.2 kbps) inserted into plasmid PBR322 vector of 3.8 kbps leading to a circular genome of about 7.0 kbps [10]. On the contrary, the latter is a real extracted HBV genome consisting in an unusual genome partially ds-DNA of about 3.2 kbps. Such a difference may be responsible for a change in the genome surface conformation and distribution of the ECL luminophore which in turn would affect the efficiency of the ECL generating mechanism [38]. The above data confirm the higher sensitivity of our method compared to standard Real time-PCR (RT-PCR) also for the real sample

composed by extracted genome (LoD: 10 cps/ $\mu$ L with sensitivity 20 IU/mL See figure.3.12) [30].

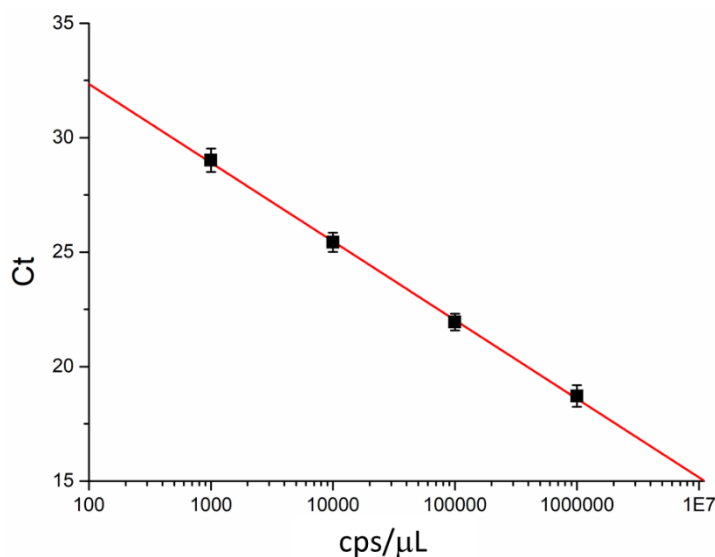
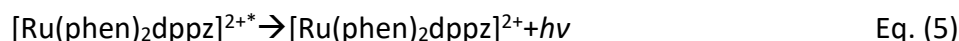
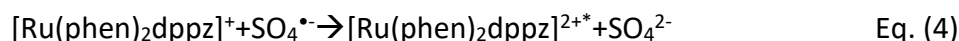
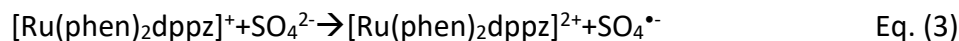


**Figure 3.12:** Calibration Curve of SG-ds HBV with RT-PCR ( $R^2 = 0.999$ ; Slope =  $-3.44 \pm 0.06$ ; Intercept =  $39.2 \pm 0.3$ )

### 3.3.3 Mechanism of the reaction

At the heart of the transduction mechanism, the processes leading to light emission are described by equations (Eq. 1-5) by applying  $-0.80V$  [39], both the reduction of peroxydisulfate (Eq. (1)) and  $[\text{Ru}(\text{phen})_2\text{dppz}]^{2+}$  (Eq. (2)) [40–42] take place, thus making the sequence of processes outlined by Eqs (3), (4), (5) possible. In particular, peroxydisulfate ( $\text{S}_2\text{O}_8^{2-}$ ) is reduced to generate a sulphate anion ( $\text{SO}_4^{2-}$ ) and a sulphate radical anion ( $\text{SO}_4^{\bullet-}$ ) (Eq. (1)), the latter also being indirectly obtained by the mediation of  $[\text{Ru}(\text{phen})_2\text{dppz}]^+$  (Eq. (3)).



The reaction between  $[\text{Ru}(\text{phen})_2\text{dppz}]^+$  and the sulphate anion radical generates the  $[\text{Ru}(\text{phen})_2\text{dppz}]^{2+}$  excited state (Eq. (4)) which emits light (Eq. (5)). The analytical system is presented in the figure below (figure 3.13).



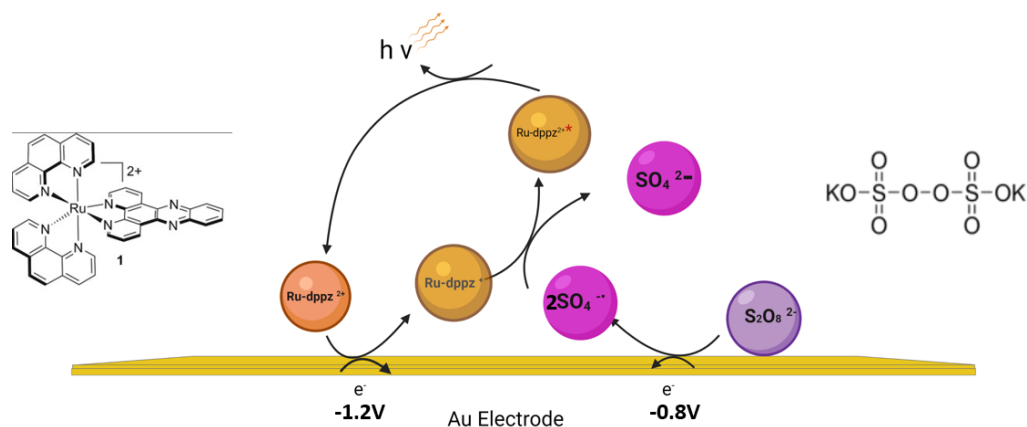


**Figure 3.13:** Scheme of ECL mechanism between  $[\text{Ru}(\text{phen})_2\text{dppz}]^{2+}$  and  $\text{K}_2\text{S}_2\text{O}_8$  for the detection of the whole genome of HBV.

### 3.3.4 pH effect

The effectiveness of the molecular recognition mechanism and the analytical performances of the above detection strategy were firstly tested at different pH values (from 5.5 to 7.4), using the SG ds-HBV concentration of  $100 \text{ cps } \mu\text{L}^{-1}$  (figure 3.14). In fact, the use of acid hybridization buffer (pH = 5.5) may lead to protonation of the -G and -C groups of DNA which promotes a stronger bonding with probes [26,43,44]. However, at pH < 7.4 unwanted reactions involving electrochemically generated  $\text{SO}_4^{\bullet-}$  take place leading to a decreasing of the ECL signal [45]. At pH = 7.4 we observed the highest ECL value intensity in agreement with previous results [46]. Finally, at pH > 7.4 the ECL intensity is strongly reduced due to the decreasing of the SG ds-HBV recognition efficiency by the P1 and P2 probes at the surface.

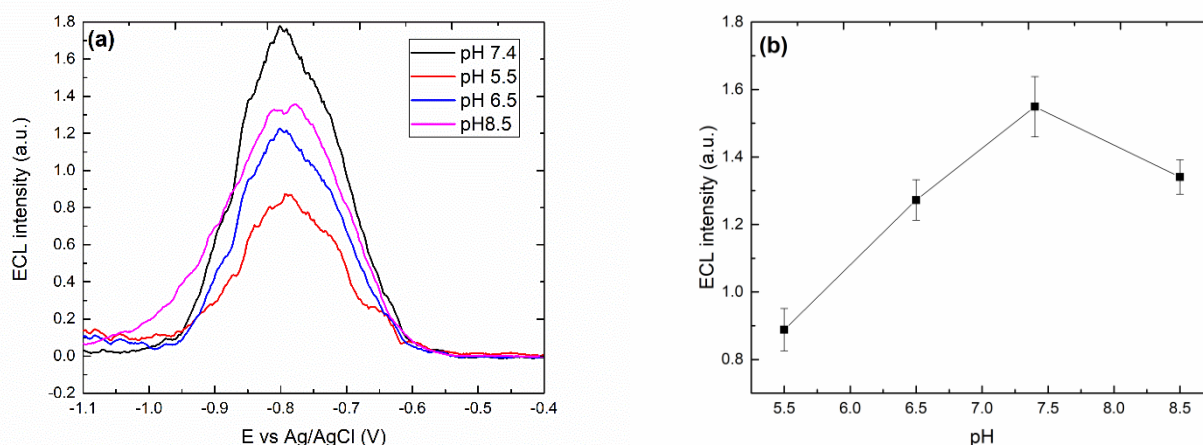


**Figure 3.14:** (a) ECL intensity vs Potential of different pH (b) ECL intensity vs different pHs values.



### 3.3.5 Applicability in biological matrixes and selectivity

An important factor in the electrically stimulated sensors is the applicability in biological fluids that can interfere with the electrical signal. The effect of biological matrixes on the modified gold electrodes was tested according to the experimental conditions described in section 3.2. To simulate the biological matrix, PBS was replaced by Fetal Bovin Serum (FBS) in the last step of triplex formation of our experimental procedure, and three different SG ds-HBV concentrations (100, 1000, and 10000 cps  $\mu\text{L}^{-1}$ ) were examined. ECL intensities measured in FBS are consistent with the one observed in PBS solution (figure 3.15). The matrix effect was evaluated by calculating the recovery amount percentage (R%) between FBS and PBS (Table T3.2), showing a satisfactory detection of SG ds-HBV in the range of 83–104%, thus confirming the efficient applicability of the proposed electrochemical DNA sensor in complex fluids without detectable interferences. These results are very promising for future application in real human complex matrixes such as plasma or blood.

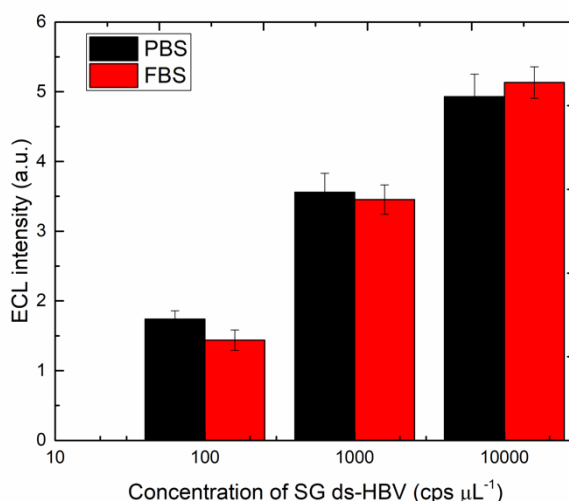


**Figure 3.15:** Comparison diagram of ECL intensity versus concentration of SG ds-HBV of 100-1000-10000 cps  $\mu\text{L}^{-1}$  in FBS/PBS 0.1M and 50 mM  $\text{K}_2\text{S}_2\text{O}_8$ . Working Au electrode with P1 and P2 formation vs Ag/AgCl reference electrode with scan rate 0.3 V/s. PMT bias of 750 V.

**Table T3.2:** Different concentrations of SG ds-HBV in PBS and FBS with RSD percent.

Concentration of HBV in PBS/FBS (cps $\mu\text{L}^{-1}$ )	Recovery amount percentage (R%)
100	82.7%
1000	97.1%
10000	104.1%

In order to evaluate its selectivity, the method was tested towards an unspecific target. Mycobacterium tuberculosis (MTB) synthetic clone at three different

concentrations (10-100-1000 cps  $\mu\text{L}^{-1}$ ) was tested resulting in the absence of any ECL emission (figure 3.16 a-c), evidencing the high selectivity of P1 and P2 probes for SG ds-HBV.

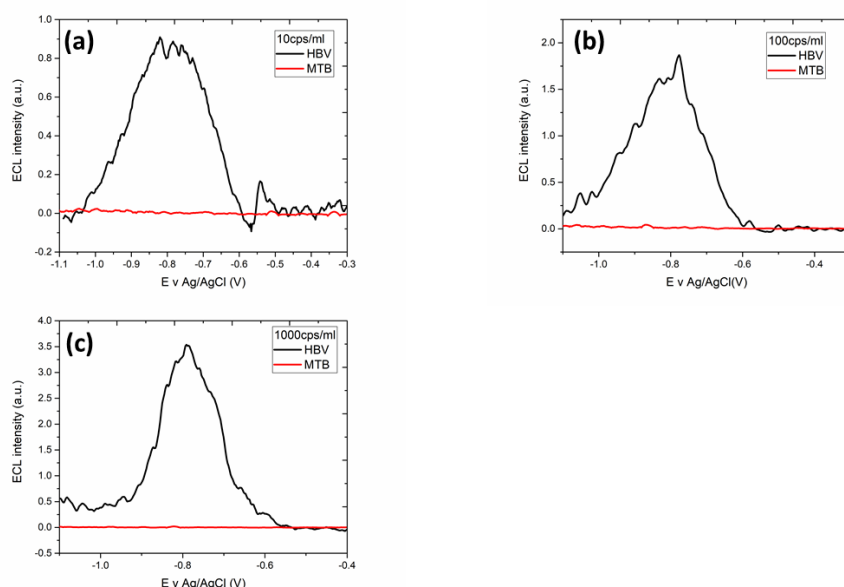


**Figure 3.16:** (a,b,c) ECL intensity vs Potential in different concentration of SG ds-HBV and MTB.

In every case that HBV was tested, it was observed a high ECL intensity (black line) instead on the MTB case (red line). According to figure 3.16 our system and specially our DNA sequences (P1/P2) are capable and selective to detect only the genome of HBV.

## 3.4 Detection of whole genome of COVID-19

### 3.4.1 COVID-19 synthetic genome quantification

Based on the previous chapters and following the same protocol for the determination of HBV genome, but only changing the specific DNA sequences probes we can determinate several viruses such as COVID-19. According to the pandemic on 2019, we need accurate and fast development of sensors for the determination of COVID-19. We have already proved that our technique is a PCR-free technique in which the amplification of signal and genome is not needed. The main difference between COVID-19 and HBV viruses is their genome, which is RNA and DNA respectively. The main difference of RNA's bases is an additional hydroxyl group on the aromatic ring which make RNA much more sensible than DNA and according to that the is kept under low temperature ( $-40^{\circ}\text{C}$ ); and a second one is the presence of uracil instead of thymine.

In the case of COVID-19 has been used three different sequences for the creation of duplex formation onto gold electrodes, as it is presented in figure 3.17.

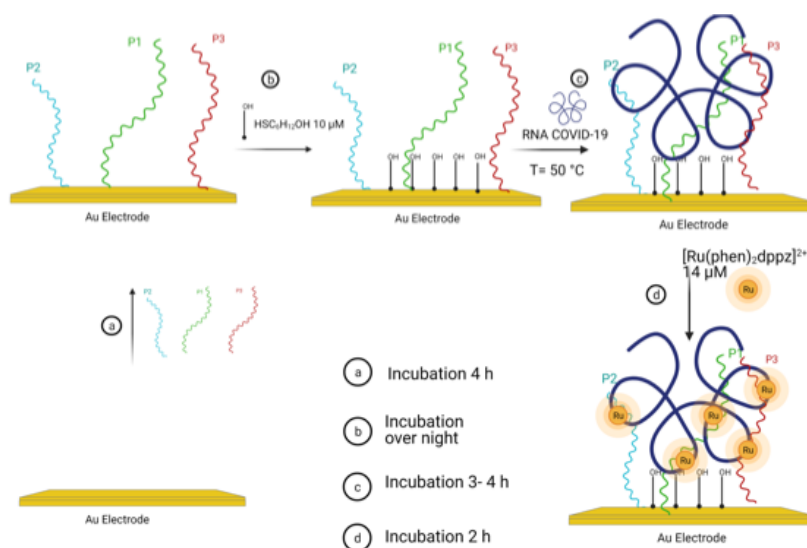


**Figure 3.17:** Scheme of ECL-PCR-free strategy: (a) Immobilization of specific probes P1 ,P2 and P3 and of (b) 6-Mercapto-1-hexanol on the surface of a gold electrode; (c) recognition of COVID-19 RNA by surface cooperative hybridization and (d) intercalation of [Ru(phen)<sub>2</sub>dppz]<sup>2+</sup> and COVID-19 whole genome detection.

The rest of our protocol's conditions remain the same (incubation time, concentration). The main reason we use three different probe sequences is because we want to create much more duplex systems onto gold electrode such the ligand - dppz ligand of ruthenium can intercalated only in duplex/triplex systems.

Based on chapter 3.3.2, initially we use synthetic COVID-19 genome (SG-COVID-19) which is commercially available and different concentration of virus have been examine in a range of 140-350000 cps/mL. Figure 3.18 presents the ECL signal response versus the potential for different concentrations (figure 3.18a).

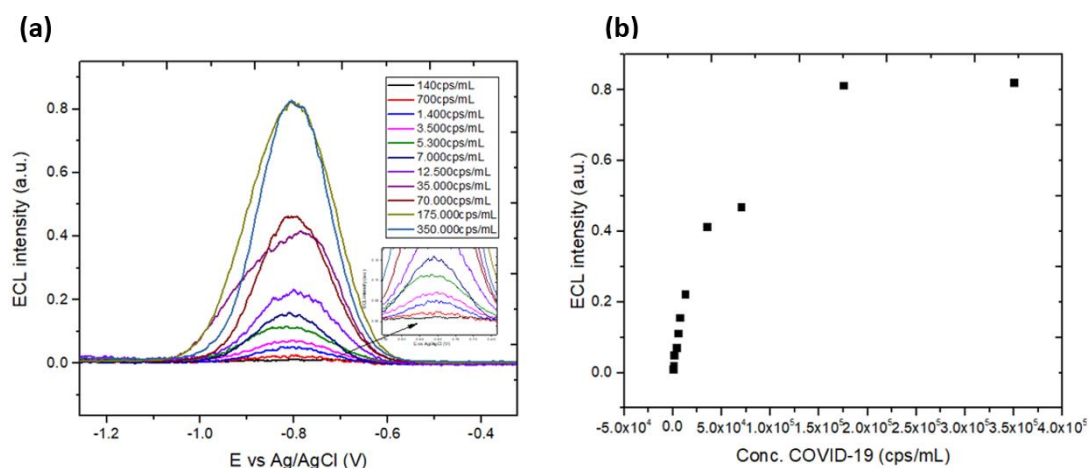


**Figure 3.18:** (a) ECL intensity vs potential for different concentration of SG COVID-19 (140–350000 cps mL<sup>-1</sup>); (b) calibration curve of ECL intensity vs COVID-19 concentration with standard deviation of  $\pm 0.022$ – $0.027$ . In PBS 0.1 M, 14  $\mu$ M intercalated [Ru(phen)<sub>2</sub>dppz]<sup>2+</sup> and 50 mM K<sub>2</sub>S<sub>2</sub>O<sub>8</sub>. Working Au electrode with P1,P2 and P3 formation vs Ag/AgCl reference electrode with scan rate 0.3 V s<sup>-1</sup>. PMT bias of 750V.

On the other hand, the behaviour of our system according to ECL emission that come from the intercalated Ruthenium complex, is linear from 140-12500 cps/mL and over this range the ECL signal is not regulable. This happens because the gold electrode's surface is saturated of several duplex systems; thus over 35000cps/mL a plateau level is observed. For the calculation of the sensitivity (LoD) 5 independent experiments has been performed for the calculation of 5 blanks and 5 standard concentrations. According to, the methodology which has been described above (chapter 3.3.2) for the SG-HBV genome, in this case the LoD is calculated to be 0.7 cps/ $\mu$ L owing an RSD value of 3.2% of each measurement.

### 3.4.2 Point of care-based sensor for the determination of extracted COVID-19 genome

After the quantification of SG-COVID-19 and based on the importance of G-PoC for the diagnosis, we developed a G-PoC sensor for the extracted genome of COVID-19 (EG-COVID-19). This chapter is a challenge topic because the detected signal is not going to be amplified with the use of PCR, on the other hand we will use PCR to know the concentration of each sample. The detection of EG-COVID-19 will be held on without the use of PMT, such it has been done for the case of EG-HBV. To do so, the use of another type of photodiode is necessary, a homemade silica photodiode (SIMP) will be used for the determination of ECL signal. The ECL signal can be transform to analogue information using a homemade software. For the determination of EG-COVID-19 four individual experiments have been performed using four different concentrations and four different approaches.

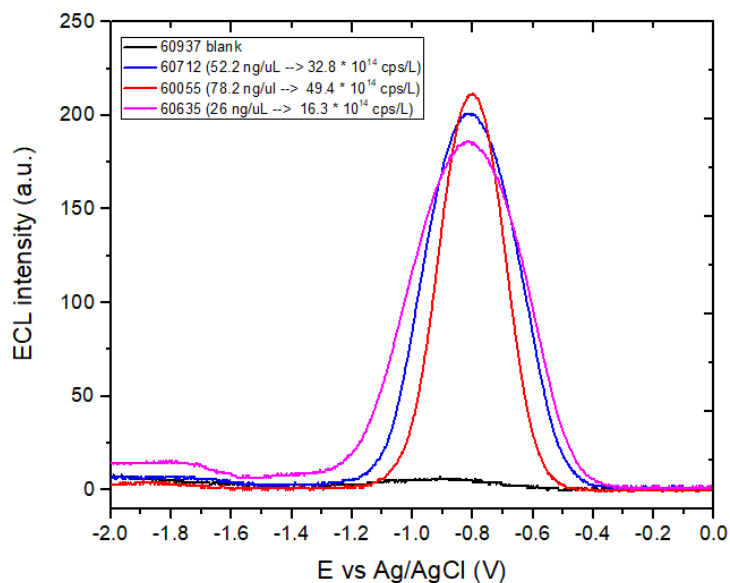


**Figure 3.19:** ECL intensity vs potential for different concentration of EG-COVID-19 (0-78.2 ng/ $\mu$ L). In PBS 0.1 M, 14  $\mu$ M intercalated  $[\text{Ru}(\text{phen})_2\text{dppz}]^{2+}$  and 50 mM  $\text{K}_2\text{S}_2\text{O}_8$ . Working Au electrode with P1,P2 and P3 formation vs Ag/AgCl reference electrode with scan rate 0.3 V  $\text{s}^{-1}$ . PMT bias of 750V.

**Table T3.3:** Different samples of EG-COVID-19

Sample	COVID RT-PCR	Cycle Threshold (Ct)	RNA concentration
60937	Neg	NA	23.5
60712	Pos	16.44	52.2
60055	Pos	19.35	78.2
60635	Pos	15.34	26.0

In the figure 3.19 is presented the ECL signal of four real samples in which the characteristics are presented in the table T3.3. The samples are obtained from three positive patients and one negative. Three of these samples are positive owing a different number of PCR cycle threshold (Ct); thus in every case the concentration of viral charge is changes, such as it is presented in the fourth column of the table T3.3. In figure 3.19 all different positive samples obtain an ECL intensity something that verifies the presence of EG-COVID-19 genome onto gold's electrode surface. Both of positive samples obtain the same ECL intensity value, in this case we suppose that the system is found in a saturation phase.

Additionally, we perform more experiments maintaining constant the Ct number and following the same process as it was described above; thus, the initial sample was diluted as 8 times. Furthermore, a blank, a positive and a positive diluted samples was prepared for further investigation. Figure 3.20 presents the ECL intensity versus the potential measurement for these three samples.

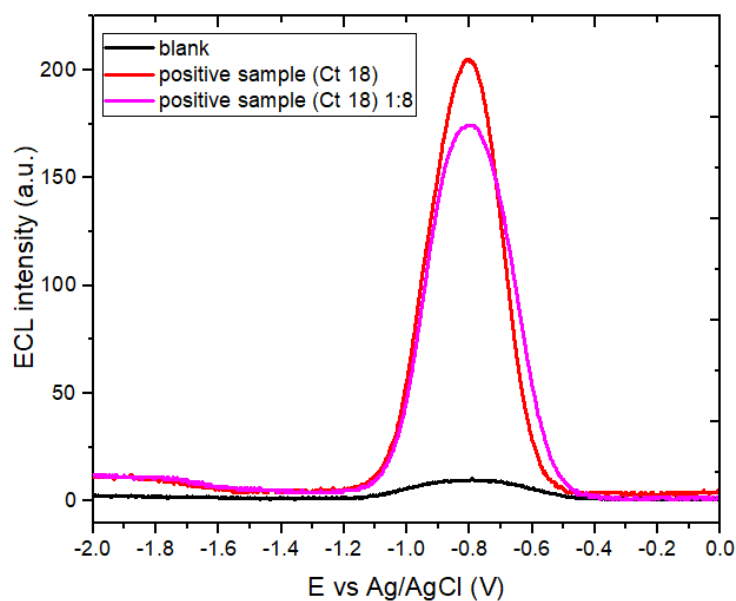


**Figure 3.20:** ECL intensity vs potential for different concentration of EG-COVID-19 (positive and 1:8 dilution of positive sample). In PBS 0.1 M, 14  $\mu\text{M}$  intercalated  $[\text{Ru}(\text{phen})_2\text{dppz}]^{2+}$  and 50 mM  $\text{K}_2\text{S}_2\text{O}_8$ . Working Au electrode with P1,P2 and P3 formation vs Ag/AgCl reference electrode with scan rate  $0.3 \text{ V s}^{-1}$ . PMT bias of 750V.

However, the Ct number is very low which means that the viral charge of measurement is very high. On the other hand, a small curve for blank measurements is presented in figure 3.20; an aspecific adsorption of Ruthenium complex may be remained in the gold's electrode surface.

The diluted sample (pink line) presents a weaker ECL intensity than the clear positive sample (red line). This difference is no proportional with the dilution number of these samples, which means that this process does not allow us to create a clear calibration plot for the calculation of LoD of EG-COVID-19 genome, because in every case the ECL intensity is very high.

According to this, new approaches for the determination and extraction of real samples EG-COVID-19 have been performed. As they are presented in table T3.4 below, four individual experiments have been performed.

**Table T3.4:** Different Procedures for the detection of COVID-19 whole genome.

<b>Abbreviations</b>	<b>Procedures</b>
DIR	Direct UTM (Universal Transport Medium)
HT	UTM after incubation in 98°C for 5 min, then in RT for 5 min (thermal extraction)
PK	UTM after hydrolysis with proteinase K (40µL UTM +4µL of enzyme)
PK+HT	UTM after hydrolysis with proteinase K (40µL UTM and 4µL of enzyme), after that incubation 55°C for 5 min, 98°C incubation for 5 min and the in RT for 5 min

Firstly, a direct sample from a positive patient was taken and placed directly in the modification with probes (P1, P2 and P3) electrode's surface. In DIR procedure has been used the inhibitors for the virus deactivation before it placed onto electrode. Then we follow the same time of protocol as it was described on the chapter 3.4.1. Then after the HT procedure, the positive virus sample was placed in high temperature (98°C) for 5 min, and we kept it in RT conditions. After that, the electrode was placed on 50°C for 3 hours (step c figure 3.17). Additionally, for PK procedure, 40µL of a positive sample, after a hydrolysis process, was incubated in the surface of a modified electrode in the presence of 4µL of proteinase K for 3-4 h in 50°C. Finally, for PK+HT procedure, after the hydrolysis such as the PK procedure, a 40µL positive sample has been used and incubated in the presence of 4µL of proteinase K first in 55°C for 5 min and then in 98°C for 5 min for the extraction of the virus. After that, the sample follow the step c for the figures 3.17. It is well to be mentioned that the Ct of each case was maintained constant (Ct= 18).

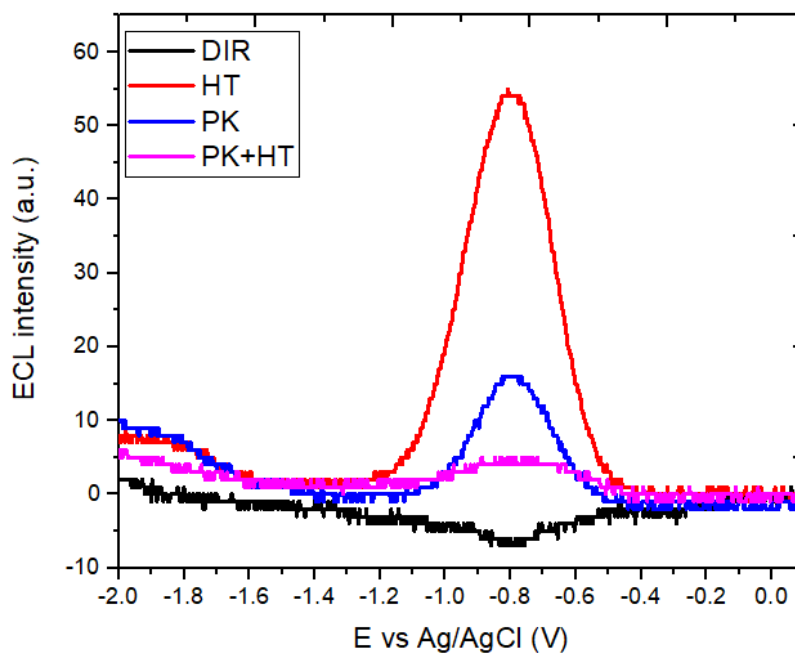


**Figure 3.21:** ECL intensity vs potential following different procedures according to the Table T3.4 for the detection of EG-COVID-19 (the concentration of the samples remains stable). In PBS 0.1 M, 14  $\mu$ M intercalated  $[\text{Ru}(\text{phen})_2\text{dppz}]^{2+}$  and 50 mM  $\text{K}_2\text{S}_2\text{O}_8$ . Working Au electrode with P1,P2 and P3 formation vs Ag/AgCl reference electrode with scan rate  $0.3 \text{ V s}^{-1}$ . PMT bias of 750V.

The figure 3.21 shows the ECL response of these four procedures. The DIR sample (black line) presents no ECL intensity which means that probably the binding EG-COVID-19 RNA had not been binded with the specific probes. However, without any duplex formation, it is impossible to have any intercalated Ruthenium molecules; thus, no light emission was observed. The red line presents the HT procedure, which obtains the highest ECL emission of 53a.u. The high thermal procedure can destroy easier the capsid of the virus; thus the RNA can be recognized by the three probes easier than the DIR procedure case. Although, for the PK procedure has been used also the enzyme named as proteinase K.

Proteinase K (molecular weight (MW) = 28.9 kDa) is a globular protein consisting of 279 amino acid residues and two disulfide bridges. It is a well-known serine protease with one chain. Proteinase K belongs to the class of subtilisin-like serine protease with the typical triad of Asp39-His69-Ser224. This protein is folded into  $\alpha$  and  $\beta$  rich regions without any clear domains. Proteinase K is stable and active in a wide spectrum of pH. The importance of proteinase K relies on its extensive use in research laboratories for providing high purity of DNA in isolation of nucleic acid, and in such industrial areas as laundry powders, food processing, etc [47–50]. Also Proteinase K, can be easily destroy the viral capsid and then the viral DNA or/and RNA can be easily released.

The PK process contains 4 $\mu$ L of proteinase K enzyme and exhibits an ECL intensity around of 20 a.u. On the other hand, HT+PK process with the same amount of Proteinase K exhibits an ECL value of 5 a.u. Both procedures present an ECL intensity



weaker than the HT procedure. We suppose that is due to the duplex structure which is not completely desorbed from the surface of the electrode and/or the presence of Proteinase K which sometimes is not capable to act in these conditions. In the conclusion, as it is presented by the figure 3.21 we keep the parameters of HT procedure for the determination of EG-COVID-19.

### 3.4.3 Detection of COVID-19 genome using HT procedure

In order to further optimization of the presented biosensor, a novel HT treatment has been investigated for viral RNA extraction, which does not need any of the expensive and time-consuming purification steps characteristic of the PCR-like extraction. In particular, figure 3.22a reports the ECL intensities vs applied potential measured in EG-COVID-19 solutions at different concentrations (up to ca. 4000 cps/mL): in this case, the only variation of the previously reported protocol is represented by the viral RNA extraction. Indeed, single-stranded RNA (ssRNA) has been extracted through a 5 minutes-long thermal treatment at 98°C, which is a temperature high enough to denature the capsid protecting the viral RNA, making it available for the hybridization with the three probes anchored on the electrodes' surface.

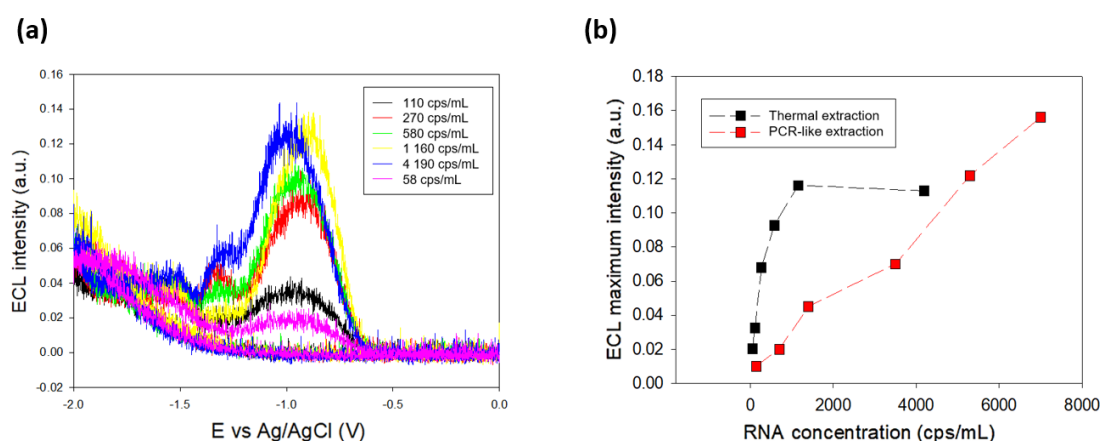


**Figure 3.22:** (a) ECL intensity vs applied potential for different SARS-CoV-2 RNA concentrations (58 – 4190 cps/mL), extracted through thermal treatment (HT). Working Au electrode with P1, P2 and P3 vs Ag/AgCl reference electrode, with scan rate of 0.3 V/s. PMT bias of 750 V. (b) Calibration curve and dependence of the response of the electrode on concentration of SARS-CoV-2, in PBS 0.01 M (pH 7.4). Comparison between results obtained upon either thermal or PCR-like extraction (Figure 3.18b), both making use of the 2-steps protocol (3 hours at 50 °C + 2 hours at RT).

First of all, observing data reported in figure 3.22a, it can be easily deduced that the presented thermal treatment effectively works as extraction, making possible to detect really few copies of EG-COVID-19 (i.e., 58 cps/mL), noteworthy without having made use of any analyte amplification and/or purification process, and having significantly reduced the time needed to perform the extraction procedure itself (from 70 to only 5 minutes). Furthermore, having analyzed separately the two different

extraction methods, it is worth carrying out a comparison between the previously reported PCR-like extraction (figure 3.18b) and the novel thermal treatment. In particular, figure 3.22b reports the ECL maximum intensity (at -0.8 V) vs EG-COVID-19 concentration, extracted either through PCR-like or thermal methodology: both of them allow an efficient detection of COVID-19 genetic code, giving back an ECL signal proportional to the viral nucleic acid concentration. Moreover, it can be clearly appreciated that thermal treatment results in ECL signals even more sensitive to smaller concentrations, providing a good linear behavior in the 0 – 2000 cps/mL range.

### 3.4.3.1. Detection of COVID-19 genome using biological matrixes and one step protocol

At this point, having demonstrated the efficient analytical performances of the presented novel ECL biosensor in the detection of EG-COVID-19, the next goal was to further decrease the time needed to perform the entire detection protocol. To this aim, a simpler one-pot recognition and intercalation step (90 minutes RNA+[Ru(phen)<sub>2</sub>dppz]<sup>2+</sup> at 50°C in PBS 0.01 M, pH 5.5) has been applied, instead of doing them separately. This strategy has been compared with the previously reported two-steps protocol, and with other different combinations of time and temperatures, summarized in Table T3.5.

**Table T3.5:** Summary of the different protocols applied to 10 electrodes, in order to compare them and analyse the analytical performances related to the novel one-step protocol (entry e). Every entry has been repeated in two sets (i.e., applied to two electrodes).

Entry	Experimental conditions
a	3 hours RNA at 50°C + 2 hours [Ru(phen) <sub>2</sub> dppz] <sup>2+</sup> at RT
b	1 hour RNA at 50°C + 1 hour [Ru(phen) <sub>2</sub> dppz] <sup>2+</sup> at RT
c	1 hour RNA at 50°C + 2 hours [Ru(phen) <sub>2</sub> dppz] <sup>2+</sup> at RT
d	1 hour RNA at 70°C + 1 hour [Ru(phen) <sub>2</sub> dppz] <sup>2+</sup> at RT
e	90 minutes (RNA + [Ru(phen) <sub>2</sub> dppz] <sup>2+</sup> ) at 50°C

The obtained data have been depicted in figure 3.23, which reports a histogram of the ECL intensities vs applied potential measured in EG-COVID-19 solutions at fixed concentration (500 cps/mL): in this case, viral ssRNA has been extracted through the thermal treatment.

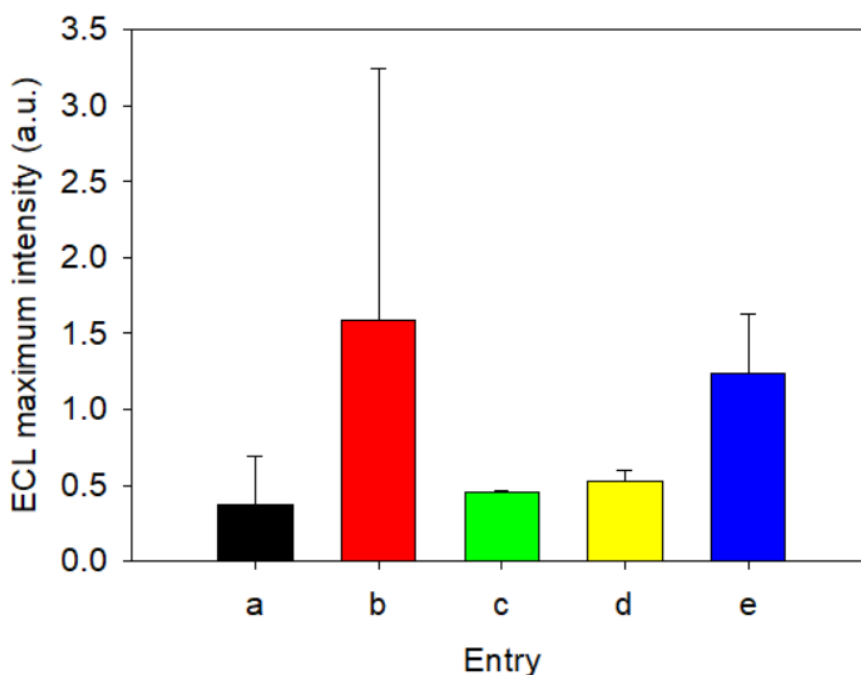


**Figure 3.23:** Maximum ECL intensity vs applied experimental conditions (see Table T3.5) and fixed SARS-CoV-2 RNA concentration (500 cps/mL). Every entry has been repeated in two sets (i.e., applied on two electrodes): calculated standard deviations have been reported as error bars on the histogram. Working Au electrode with P1, P2 and P3 vs Ag/AgCl reference electrode, with scan rate of 0.3 V/s. PMT bias of 750 V.

From the reported plots, it is worth noting that entry *e* (corresponding to the novel one-step protocol) results to be characterised by much higher ECL signals for the same ssRNA concentration. On the other hand, changes in temperature, RNA incubation time and/or  $[\text{Ru}(\text{phen})_2(\text{dppz})]^{2+}$  intercalation time give back ECL signals that are identical between them. Also, it must be mentioned that the poor reproducibility related to entry *b* (i.e., high standard deviation value) could probably be due to a DNA contamination occurred at some point inside the system under analysis.

### 3.4.3.2 Investigations on the matrix effect

In order to analyse more in detail, the analytical performances of the developed PCR-free COVID-19 detection method, investigations on the matrix effect were needed, simulating a real sample behaviour. To this aim, a commercial negative nasal SARS-CoV-2 test has been exploited, in combination with the viral RNA thermal extraction and the one-pot recognition and intercalation step protocol. Particularly, commercial viral transmission medium (VTM, containing negative nasal test) has been used as matrix: it has been subjected to the same thermal treatment applied to COVID-19 genome, then it has been added to RNA solutions. Afterwards, electrodes were incubated with RNA using the one-step protocol (90 minutes VTM+RNA+ $[\text{Ru}(\text{phen})_2(\text{dppz})]^{2+}$  at 50°C). The obtained data have been depicted in figure 3.24a, which reports the ECL intensities vs applied potential measured in COVID-19 RNA solutions at different concentrations (0 – 20 000 cps/mL), in commercial VTM.

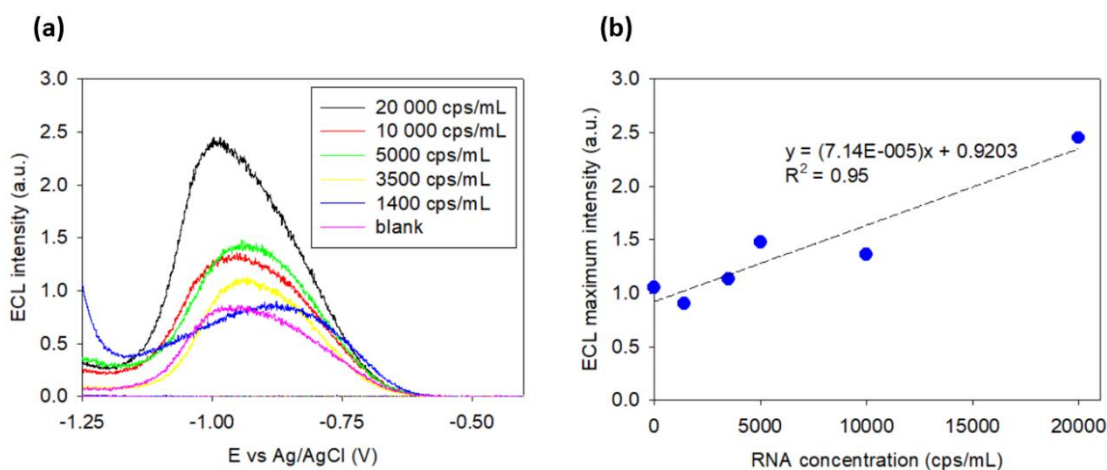


**Figure 3.24:** (a) ECL intensity vs potential for different concentration of SG COVID-19 (0-20000 cps mL<sup>-1</sup>), in commercial VTM; (b) calibration curve of ECL intensity vs COVID-19 concentration PBS 0.1 M, 14 μM intercalated [Ru(phen)<sub>2</sub>dppz]<sup>2+</sup> and 50 mM K<sub>2</sub>S<sub>2</sub>O<sub>8</sub>. Working Au electrode with P1, P2 and P3 formation vs Ag/AgCl reference electrode with scan rate 0.3 V s<sup>-1</sup>. PMT bias of 750V.

As it can be easily appreciated from the plot reported in figure 3.24b, a linear dependence between the ECL maximum intensity (at -0.8 V) and the viral ssRNA concentration is found, reporting an R<sup>2</sup> value of 0.95. Moreover, comparing the obtained results (figure 3.24b) with the data previously reported in figure 3.22b, it can be easily observed that the matrix effect results in higher COVID-19 RNA concentrations to be detected by the presented biosensor (coupled with a higher ECL intensity signal). In fact, in this case the calculated LoD was 14 cps/μL (i.e., 23.3 aM), which is higher with respect to the experiments performed in the absence of the matrix.

### 3.5 Conclusions

In summary, we developed a novel molecular sensor for ultrasensitive and PCR-free detection of HBV and COVID-19 whole genome. Our method exploits a surface cooperative hybridization at miniaturized gold electrode with ECL transduction through the intercalation of [Ru(phen)<sub>2</sub>dppz]<sup>2+</sup> complex, using potassium persulfate (K<sub>2</sub>S<sub>2</sub>O<sub>8</sub>) as coreactant. By combining the superior analytical performances of ECL and the signal amplification offered by the intercalation of a high number of ECL-active Ru complexes, we were able to detect HBV and COVID-19 whole genome from real sample without any amplification step, reaching a LoD of 0.06 cps μL<sup>-1</sup> (i.e. 0.1 aM) and 1.4 cps μL<sup>-1</sup> (23.3 aM), respectively. This approach may be performed with extremely simple and portable instrumentation and ongoing research in our laboratories is dedicate to the detection of viral genomes using the same strategy. The present results represent indeed an important step towards the development of rapid, sensitive and amplification free molecular Point-of-Care (PoC) test for monitoring infectious diseases.

## References

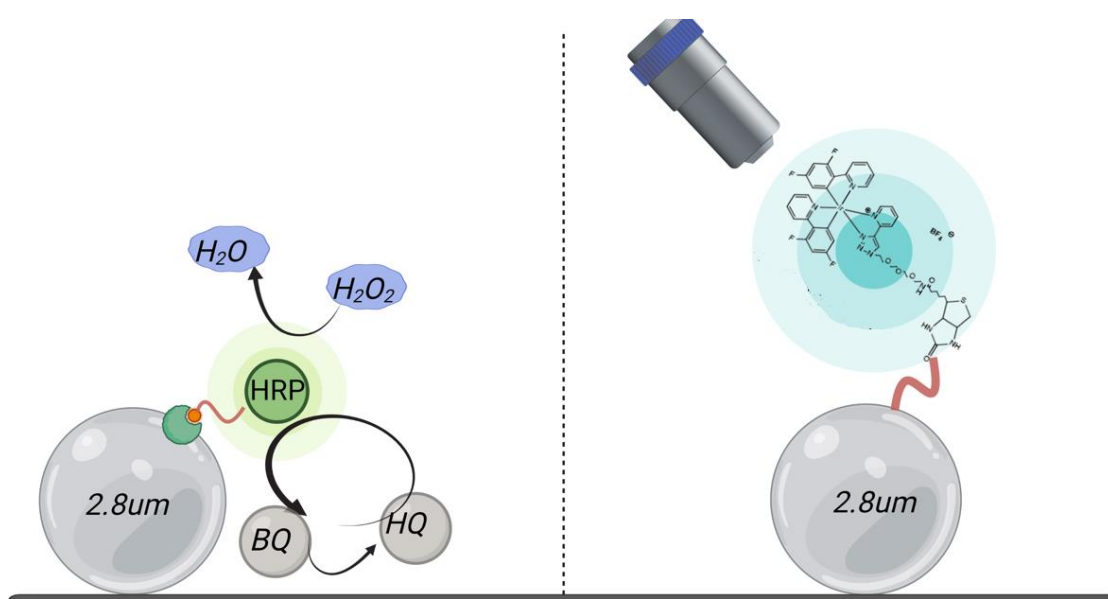
- [1] M.J. Espy et al. *Clin. Microbiol. Rev.* 19 (2006) 165–256.
- [2] J. Cheong et al. *Nat. Biomed. Eng.* 4 (2020) 1159–1167.
- [3] Z. Fan et al. *Biosens. Bioelectron.* 178 (2021) 113015.
- [4] E. Nunez-Bajo et al. *Nat. Commun.* 11 (2020).
- [5] S. Petralia, S. Conoci, *ACS Sensors.* 2 (2017) 876–891.
- [6] C. Wang et al. *Nano Today.* 37 (2021) 101092.
- [7] F. Arduini et al., *Trends Anal. Chem.* 79 (2016) 114–126.
- [8] E. Kerr et al. *Sensors Actuators, B Chem.* 330 (2021) 129261.
- [9] Y. Wen et al. *Sci. Rep.* 84 (2012) 14–18.
- [10] S. Petralia et al. *Analyst.* 142 (2017) 2090.
- [11] A.A. Leonardi et al. *ACS Sensors.* 3 (2018) 1690–1697.
- [12] World Health Organization (WHO), *Global Health Sector Strategy on Viral Hepatitis, (2016) 2016–2021.*
- [13] J. Summers et al. *Proc. Natl. Acad. Sci. U. S. A.* 75 (1978) 4533–4537.
- [14] C. Transy et al. *Proc. Natl. Acad. Sci. U. S. A.* 89 (1992) 3874–3878.
- [15] A. Sauerbrei et al. *J. Hosp. Infect.* 64 (2006) 358–365.
- [16] M. Chevreuil et al. *J. Phys. Chem. B.* 124 (2020) 9987–9995.
- [17] T.G. Bell et al. *Intech.* 8 (2016) 177–200.
- [18] C. Sakai et al. *Biochem. Biophys. Res. Commun.* 581 (2021) 103–109.
- [19] J. Inoue et al. *Viruses.* 13 (2021).
- [20] Y. Lin et al. *Sci. Rep.* 8 (2018) 1–9.
- [21] M. Bierhoff et al. *J. Pregnancy.* 2019 (2019).
- [22] J.-M. Kim et al. *Public Heal. Res Perspect.* 11 (2020) 3–7.
- [23] P. Zhou et al. *Nature.* 579 (2020) 270–273.

- [24] V.D. Menachery et al. *Curr. Opin. Virol.* 23 (2017) 1–7.
- [25] M.M. Lai, et al. *J. Virol.* 38 (1981) 661–670.
- [26] S. Petralia et al. *Colloids Surfaces B Biointerfaces.* 187 (2020) 110648.
- [27] E. Auvinen et al. *Mol. Diagnosis Ther.* 21 (2017) 45–57.
- [28] D. Paraskevis et al. *J. Virol. Methods.* 103 (2002) 201–212.
- [29] A. Abe et al. *J. Clin. Microbiol.* 37 (1999) 2899–2903.
- [30] T. Alice et al. *J. Clin. Microbiol.* 45 (2007) 828–834.
- [31] P. Nikolaou et al. *Biosens. Bioelectron.* 209 (2022) 114165.
- [32] M. Gebala et al. *ChemPhysChem.* 11 (2010) 2887–2895.
- [33] Y. He et al. *Anal. Chem.* 87 (2015) 9777–9785.
- [34] L. Yang et al. *Biosens. Bioelectron.* 70 (2015) 268–274.
- [35] J. Chambron et al. *Chem. Phys. Lett.* 182 (1991) 603–607.
- [36] A.E. Friedman et al. *J. Am. Chem. Soc.* 112 (1990) 4960–4962.
- [37] C. Hiort et al. *J. Am. Chem. Soc.* 115 (1993) 3448–3454.
- [38] A. Zanut et al. *Anal. Chem.* (2021)157-162.
- [39] O. V. Reshetnyak et al. *Electrochim. Acta.* 43 (1997) 465–469.
- [40] X.X. Liang et al. *Electrochim. Acta.* 312 (2019) 313–319.
- [41] X. Wang et al. *Anal. Chem.* 90 (2018) 3013–3018.
- [42] T. Zhou et al. *Adv. Sci.* 7 (2020) 1–10.
- [43] P. Dai et al. *Anal. Chem.* 87 (2015) 12372–12379.
- [44] A. Fiorani et al. *Chem. Sci.* 11 (2020) 10496–10500.
- [45] H. Huang et al. *Nanoscale.* 2 (2010) 606–612.
- [46] L. Ismail et al. *Appl. Catal. B Environ.* 201 (2017) 573–581.
- [47] Y. Tao et al. *J. Biomol. Struct. Dyn.* 28 (2010) 143–157.
- [48] C. Betzel et al. *Biochemistry.* 40 (2001) 3080–3088.

[49] R. Tomar et al. *Biochimie*. 91 (**2009**) 951–960.

[50] L.A. Stone et al. *Biochemistry*. 46 (**2007**) 245–252.

# CHAPTER 4



**Surfaces could be replaced by other platforms such as magnetic beads?**



## 4.1 Introduction

One main factor in the evaluation process of an electrochemical or ECL biosensor is reproducible regeneration of the sensing surface. This renewal is a difficult task since it requires reviving the recognition element bound to the transducer surface. Moreover, this drawback makes it difficult for the biosensors to be integrated into automatic systems [1-6]. An alternative approach to achieve this renewal is applying the disposable MBs to build up the biosensors. With the assistance of an external magnet, the in situ biosensing surface is built up by localizing the recognition element coated MBs on the electrode area. The electrode surface can be easily renewed by alternate positioning of the external magnet. Meanwhile, MBs provide a high surface area to immobilize the biomolecules as much as possible, resulting in a lower detection limit. Moreover, the use of MBs can play the dual role of concentration and purification. It is particularly efficient in detecting analytes in complex sample matrix, which may exhibit either poor mass transport to biosensor or physical blockage of biosensor surface by non-specific adsorption[6]. MBs-based techniques can take away the need for sample pretreatment by centrifugation or chromatography, thus shortening the handling time [7]. In addition, most of the MBs, especially the iron oxide ones, are biocompatible and non-genotoxic; they can either be applied for simple adsorption of biomolecules, or functionalized or encapsulated in polymers or metal or silica NPs or carbon materials to enhance the biocompatibility and increase the functionalities[8],[9]. Therefore, MBs have been providing a promising experimental platform for developing both electrochemical and ECL biosensors.

The modification of MBs can be held easily, immunosensors can be combined with enzymes such as HRP. In general, the metalloenzymes can be used as biological substrates for redox reactions. A well-known mechanism is the horseradish peroxidase (HRP), hydrogen peroxide ( $H_2O_2$ ) and the use of a redox mediator such as hydroquinone (HQ). This approach gives the opportunity to study a  $2e^-$  transfer in electrochemical reactions. The electron transfer occurs between an electroactive species and an electrode surface, whether the electrode material determines the overall rate of the electrochemical reaction, and could even be used to estimate the allotrope of the material in question [10] and/or the determination of an analyte based on the differential current values. Indeed this mechanism was used by several groups such as Ge et al.[12] co-immobilized anti-MC antibody and HRP on silica-coated ferroferric oxide ( $Fe_3O_4$ ) MBs and used them as carriers. Once the sandwich immunoreaction was completed, electrochemical measurements were recorded according to the oxidation of the thionine mediator, which was catalyzed by both the HRP and  $Fe_3O_4$  MBs. Another electrochemical approach is a simple amperometric sandwich-based immunoplatfrom suitable for the sensitive determination of CD147 protein in lysed and entire exosomes isolated from CRC cancer cell lines with different metastatic capacity is reported for the first time using MBs by the group of Prof. S. Campuzano[13]. The proposed strategy relies on the covalent attachment of specific CD147 capture antibodies onto the surface of commercially available carboxylate

magnetic microbeads and the use of biotinylated antibodies and streptavidin-HRP conjugates as detectors and enzymatic tracers, respectively, to perform the amperometric transduction at SPCEs.

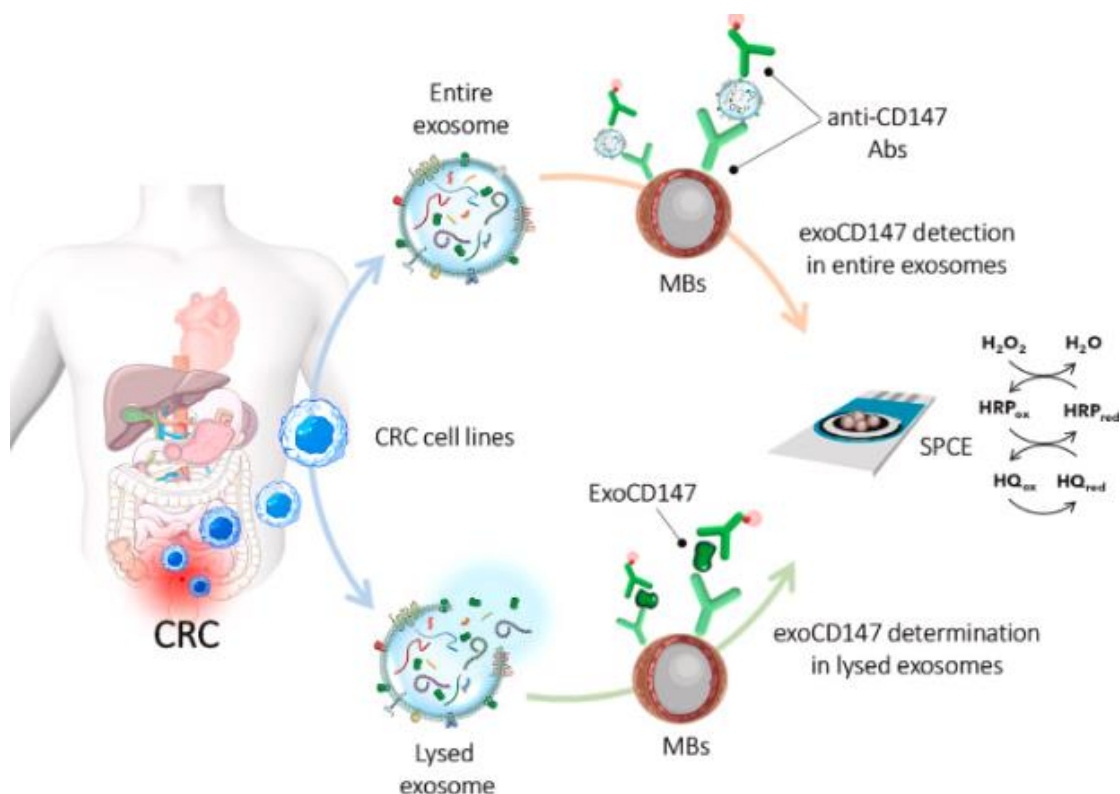


**Figure 4.1:** Schematic display of the implementation of the proposed amperometric sandwich-based immunosensing strategy for the determination of CD147 in entire (upper route) or lysed (down route) CRC isolated exosomes. Permission of [13].

The use of MBs as antibody immobilisation support is described in several magneto-controlled competitive immunoassays and immunosensors. In the simplest approach, the immunocomplexes are first formed and later captured on magnetised electrodes for the electrochemical measurement.

#### 4.1.1 Magnetic Beads for electrochemiluminescence applications

Typically,  $\text{Ru}(\text{bpy})_3^{2+}$  ECL immunoassay uses streptavidin-coated paramagnetic beads to bind with the biotinylated antibodies. The beads act as the solid support and form sandwich structure with the antigens and the ECL tag-labeled antibodies. The magnetic sandwich sample is delivered to the electrode, and when the required electric potential is exposed on the electrode, the light subsequently emits in the presence of a  $\text{Ru}(\text{bpy})_3^{2+}$  co-reactant (e.g. TPA) and is measured in a photomultiplier tube and digitally recorded. The cell is then washed and ready for the next assay. ECL immunosensor provides a disposable, sensitive and selective platform for determining

target proteins with short assay time and simple operations. It has been extensively explored and commercially developed since last century [14].

To further improve its sensitivity, one shortcut is the use of the nanoparticles (NPs) to modify the MBs is, such as the core-shell Fe<sub>3</sub>O<sub>4</sub>-gold NPs[15]. However, because ECL immunoassay has been mature and commercial, recent publications about MBs-based ECL immunosensors were fewer. Even though some works have been reported, the researcher paid most attention to the functionalized ECL tags by advanced materials for signal amplification [14–18], or ultrasensitive assay of new analytes [18]. For example, Zhan and Bard [16] applied liposomes (~100-nm diameter) containing Ru(bpy)<sub>3</sub><sup>2+</sup> as the ECL tag for a sandwich-type immunoassay of human C-reactive protein with the detection limit of 100 ng mL<sup>-1</sup>. Li et al. proposed an ultrasensitive ECL immunoassay of carcinoembryonic antigen with detection limit of 8.0 × 10<sup>-15</sup> M (1.6 pg mL<sup>-1</sup>) by using NPs as the carrier of ECL tags for ECL signal amplification. This ECL immunosensor was distinctive from the conventional ones based on MBs, where the MBs were used as platforms for separation and only one or few luminophore molecules were attached to the antibodies. In this protocol, multiple Ru(bpy)<sub>3</sub><sup>2+</sup> species have been conjugated to a NPs that was corresponding to one antigen molecule. Thus significant signal amplification was reached [17]. Additionally, ultrasensitive detection of 1,3,5-trinitrotoluene (TNT) contaminations in soil and creek water samples was accomplished by the sandwich type ECL immunosensors. Detection limit was ≤0.10 ± 0.01 ppb and was about 600-fold lower as compared with the most sensitive TNT assay method in the literatures[19]. In these ECL immunosensors, the used MBs were almost the normal streptavidin-coated ones [16],[14] and a similar trend was also found for the DNA and aptamer biosensors.

Works on MBs-based DNA biosensors have been recently concentrated on amplification protocols for sensitive specific detections of analytes such as plant viruses [20], plant pathogenic bacteria [21], telomerase activity [22] point mutation[23], single-mismatched DNA and cells[13]. MBs used herein were just one assistant technique to establish these protocols, but it must be pointed out that MBs was also one of the crucial factors to reach these highly sensitive, simple, time-effective, and reproducible determinations.

#### **4.1.2 Magnetic beads conjugated with luminophore complexes**

With the development of ECL analysis, various ECL luminophores including organic small molecules[24], organic polymers[25], inorganic nanomaterials[26] and inorganic complexes have been extensively studied. Among aforementioned luminophores, iridium(III) complexes possess unparalleled superiorities such as excellent quantum efficiency, tunable photophysical properties and long lifetime[27] thus having aroused the research interest in ECL field. For example, Wei'group severally used horse spleen apoferritin nanocages and PEGylated apoferritin to

encapsulate iridium(III) complexes for preparing single-signal-based immunosensor [28]. Li's group also designed a dinuclear iridium(III) complex for ECL determination of pesticides [29]. The reported applications of iridium(III) complexes were mainly based on anodic ECL emission and rarely based on cathodic or bipolar ECL emissions. This limitation may be caused by weak cathodic emission and lack of suitable dual-regulating factor for achieving the different change of bipolar ECL signals associated with the target.

Recently, various materials such as metal nanoparticles, metal oxides and organic nanomaterials have been developed to improve ECL intensity. For instance, metal organic framework [30], Ag nanoparticles [31], and Fe@Fe<sub>2</sub>O<sub>3</sub> nanowires [32] were adopted as accelerators to boost cathodic or anodic ECL signal. However, these reported accelerators acted only on a single cathodic or anodic emission, not on bipolar emission simultaneously.

Iridium complexes can be used for the development of biosensors, as mentioned in the previous chapters. In such cases iridium nanorods (NRs) can be used as luminophore complexes. Recent research has demonstrated that Ir NRs were modulated by poly(styrene-co-maleicanhydride) (PSMA) to simultaneously emit strong bipolar ECL signals in the presence of anodic coreactant *N,N*-diisopropylethylenediamine (DPEA) and cathodic coreactant persulfate (S<sub>2</sub>O<sub>8</sub><sup>2-</sup>). Meanwhile, Ag NPs were explored as dual-regulating coreaction accelerator to simultaneously boost the bipolar emissions of Ir NRs. With the combination of dual-emitting character of Ir NRs and dual-regulating effect of Ag NPs, a novel mono-luminophore-based ECL ratio strategy was developed [32].

## 4.2 Analytical approach in a standard electrochemical system using MBs

Here, to the best of our knowledge for the first time, we examine the effect of a different size MBs system based on a standard electroanalytical mechanism (HRP/H<sub>2</sub>O<sub>2</sub>/HQ). Our scope is to investigate the difference analytical features changing the size of MBs. This project is a collaboration with the group of Prof. S. Campuzano from the University of Madrid (UCM).

### 4.2.1 Chemicals and Materials

Analytical grades were used for this work. Streptavidin-modified MBs (str-MBs, Ø=2.8µm, concentration of 0.72mg/mL) was purchased by Roche company, (str-MBs,

$\varnothing=0.1, 0.3, 0.5\mu\text{m}$ , concentration of 5, 5, and 10 mg/mL respectively) were purchased by Ademtech company and (str-MBs,  $\varnothing=1.0\mu\text{m}$ , concentration of 10mg/mL) was purchased by Termo-Fisher company. Anti-peroxidase (horseradish) (rabbit) antibody biotin conjugated (b-Ab) was purchased from Rockland stored in  $-40^{\circ}\text{C}$  in aliquots of  $5\mu\text{L}$ .

All solutions were prepared using water purified by the Milli-Q purification system ( $18.2\text{ M}\Omega\text{ cm}$ ). Sodium Chloride, and tris-hydroxymethyl-aminomethane-HCl (Tris-HCl) were from Scharlab. 3,3',5,5'-Tetramethylbenzidine (TMB), hydroquinone (HQ) and hydrogen peroxide ( $\text{H}_2\text{O}_2$ , 30% w/v) were provided from Sigma-Aldrich. The used buffers included: 10 mM phosphate buffer saline solution (PBS) pH 7.4; B&W buffer pH 7.5 (0.01 mol/L Tris-HCl pH 7.5 containing, 1 mmol/L EDTA and 2 mmol/L NaCl) and 50 mM phosphate buffer (PB) solution pH 6.0.

#### 4.2.2 Instrumentation

Amperometric measurements were performed at room temperature ( $25^{\circ}\text{C}$ ) in stirred solutions using a model CHI812B (CH Instruments, Inc.) potentiostat controlled by the CHI812B software. Electrochemical stirring cells was a 10 mL glass cells from Pobel where the SPCEs placed on a homemade polymethylmethacrylate (PMMA) casing with an embedded neodymium magnet (AIMAN GZ) were immersed.

Screen-printed carbon electrodes (SPCEs, DRP-110), with a 4 mm- $\varnothing$  carbon working electrode include a carbon counter electrode and an Ag pseudo-reference electrode. Specific cable connectors (DRP-CAC) used as interface between the SPCEs was from Metrohm-DropSens.

Absorption spectra were recorded using a Cary 60 UV-Vis spectrophotometer (Agilent) using a 2mL glass cuvette.

### 4.3 Preparation of ASSAY

Figure 4.2a demonstrates the development of the methodology which involves one immunoassay strategy for the determination of HRP using modified MBs with selective antibody. First, MB modified with streptavidin (str-MBs) was incubated with a standard concentration of biotinylated Antibody (b-Ab). According to the chemistry between streptavidin and biotin the b-Ab can be immobilized onto str-MBs. Afterwards, the str-MBs/b-Ab was incubated with a standard concentration of HRP, which can be easily recognized by the b-Ab during a standard incubation time. The subsequent magnetic capture of the modified MBs on the working electrode surface of the disposable electrodes allowed the amperometric transduction with the  $\text{H}_2\text{O}_2/\text{HQ}$  system ( figure 4.2b).

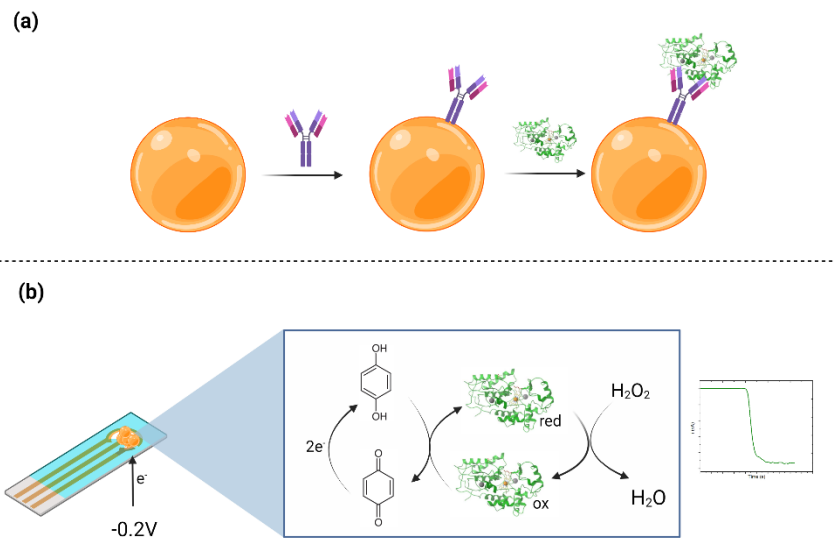


**Figure 4.2:** (a) Preparation steps for the development of the biosensors. (b) Amperometric method for the determination of HRP

**Table T4.1:** Optimal conditions for the preparation of MBs/b-Ab/HRP

\*After 10 times dilution of the principal solution

Size of MBs ( $\mu\text{m}$ )	Optimal MB Volume ( $\mu\text{L}$ )	Optimal b-Ab concentration ( $\mu\text{g/mL}$ )	Optimal b-Ab incubation time (min)	Optimal HRP incubation time (min)
2.8	3	10	30	30
1	5	10	30	45
0.5	10*	5	30	30
0.3	2	7.5	10	10
0.1	2	10	15	30

For the preparation of each MBs/b-Ab/HRP category every parameter such as volume of MBs, concentration of b-Ab and, incubation time was optimized as it is presented

in table 4.1. All washing and incubation steps were carried out in 1.5 mL microcentrifuge tubes. After each step, the tubes with the MBs suspension were placed in the magnetic concentrator for 2 min to remove the corresponding supernatant. The preparation of MBs/b-Ab/HRP conjugates (Figure 4.2) involved the use of a determinate  $\mu\text{L}$  of str-MBs suspension which was washed twice with 50  $\mu\text{L}$  of B&W buffer (pH 7.5). Thereafter, the str-MBs were incubated for determined minutes (25 °C, 950 rpm) with 25  $\mu\text{L}$  of determined concentration ( $\mu\text{g mL}^{-1}$ ) of b-Ab prepared in B&W buffer solution (pH 7.5). After washing twice with B&W, the modified MBs was placed in a standard concentrated solution of HRP ( $\text{ng mL}^{-1}$ ) and then they incubate for specific time (25 °C, 950 rpm). The HRP was prepared in a PBS pH 7.4 solution. After washing twice with PBS pH 7.4, the MBs were transferred onto the SPEs' electrochemical active surface, which is placed in a specific homemade PMMA holder with magnet.

### 4.3.1 Amperometric detection of HRP

The ensemble SPCE-PMMA casing was immersed into the measuring cell containing 10 mL of 50 mM PB pH 6.0 and 100  $\mu\text{L}$  of a fresh 100 mM HQ solution prepared in the same buffer. The amperometric measurements were recorded under stirring by applying  $-0.20\text{ V}$  vs. the Ag pseudo-reference electrode upon adding 50  $\mu\text{L}$  of 100 mM  $\text{H}_2\text{O}_2$  solution prepared daily in 50 mM PB (pH 6.0) until the steady state was reached. The variation in the cathodic current resulting from the HRP-catalyzed reduction of  $\text{H}_2\text{O}_2$  mediated by HQ, which is initially in the quinone oxidized form, was recorded. The analytical responses presented throughout the text correspond to the difference between the steady state and the background currents.

### 4.3.2 Optimal conditions

The effect of the experimental variables involved in the preparation of HRP/b-Ab/str-MBs immunoconjugates on the amperometric were evaluated. Considering that, the optimization criterion was the largest ration between the cathodic currents measured with the immunosensor in the presence of 0-10 ng/mL HRP standard sample (S) and in the absence of it (B). The variables tested were: (a) the volume of MBs, (b) the concentration of b-Ab, (c) the incubation time of b-Ab, and (d) the incubation time of HRP for each different size of MBs. The results acquired are presented in Figure 4.3-6.

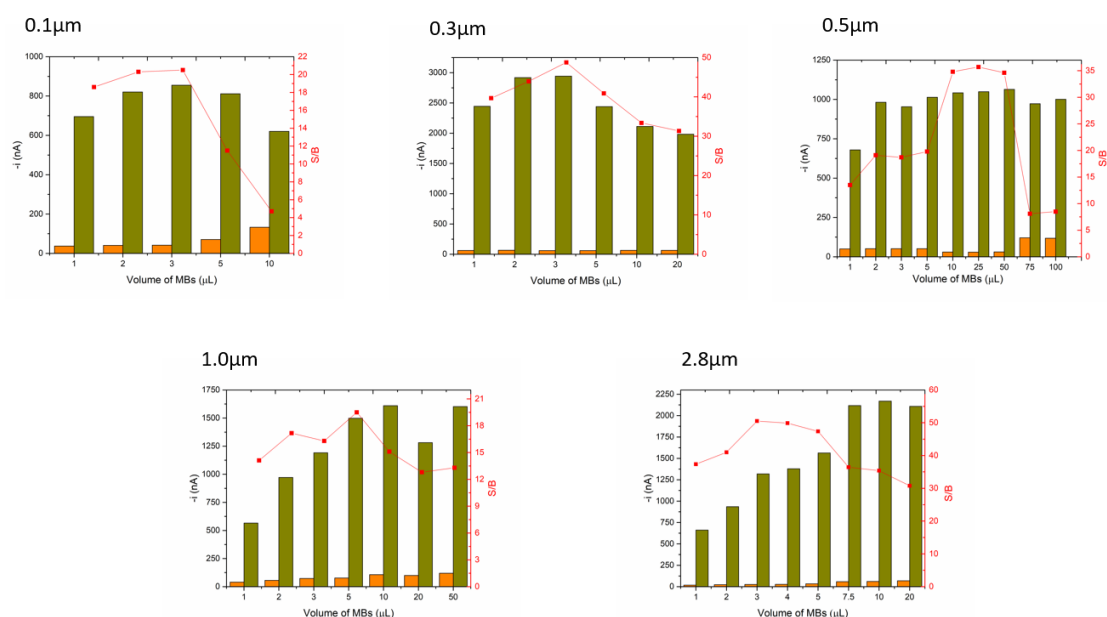


**Figure 4.3:** Optimization for the volume of MBs

According to the results of Figure 4.3, the optimal volume of each size of MBs varies and it changes in each MBs. The influence of the volume of MBs on the amperometric response was tested by incubating the commercial str-MBs with a standard concentration of b-Ab ( $10 \mu\text{g}/\text{mL}$ ) and a standard concentration of HRP (5 or 10 ng/mL). Each sample (S) was tested in comparison with a blank (B) value without the presence of analyte. We chose the optimal volume of each category based on the best electrochemical relationship (S/B). The S/B relationship is presented with the red dots in every single figure. On one hand, it must be noticed that the blank (B) value increases when the MBs volume also increases. This phenomenon could be a result of the MB reduction in negative potential because of the Fe center. On the other hand, the sample (S) signal exhibits increments and decrements depending on the MBs volume. This phenomenon could be explained by the block of the electron transfer. A huge amount of MBs and their position of the electrode's surface (one above the other), can limit the electron transfer and a weaker EC signal can be produced.

The concentration of the immobilized b-Ab onto MBs can also affect the electrochemical signal of the sensors. In each case the MBs surface must be covered by the best concentration of b-Ab without any interference. In figure 4.4, several concentrations of b-Ab (0-50  $\mu\text{g}/\text{mL}$ ) have been used for the same concentration of HRP. However, the best S/B value has been chosen as the optimal for each MBs category.



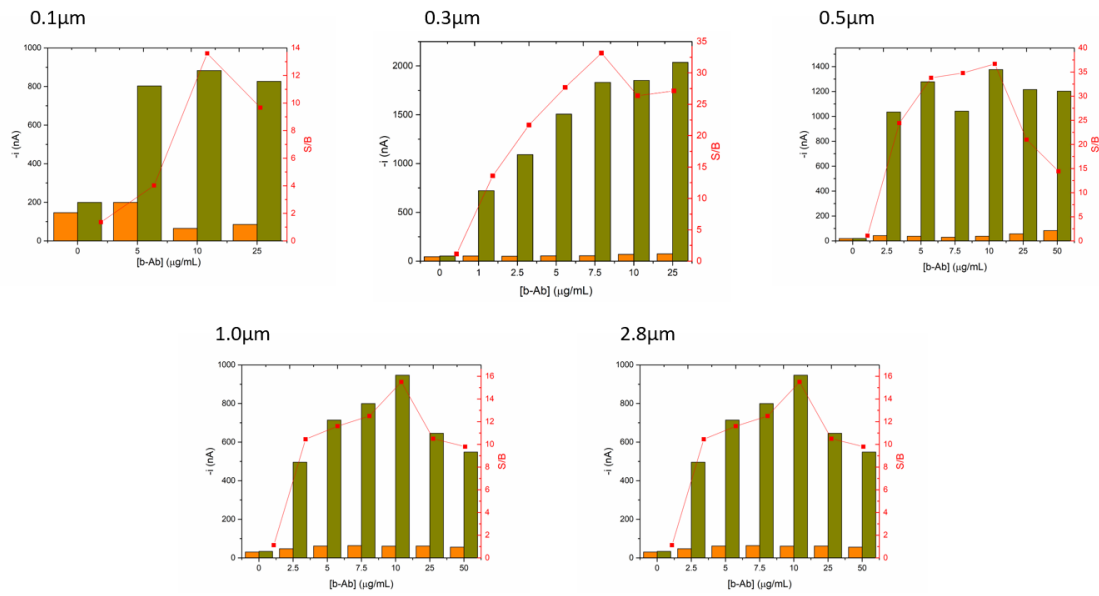


**Figure 4.4:** Optimization for the concentration of biotinylated Antibody

Figures 4.5 and 4.6 show the effect of incubation time of b-Ab and HRP, respectively. By using the optimal values of the Figures 4.3 and 4.4, we evaluate the optimal incubation time for a constant concentration of b-Ab and HRP. For each time optimization we use a range of 0-60 min. The summary of optimal conditions is presented in table 4.1 and the incubation has occurred under 25°C and 950 rpm.

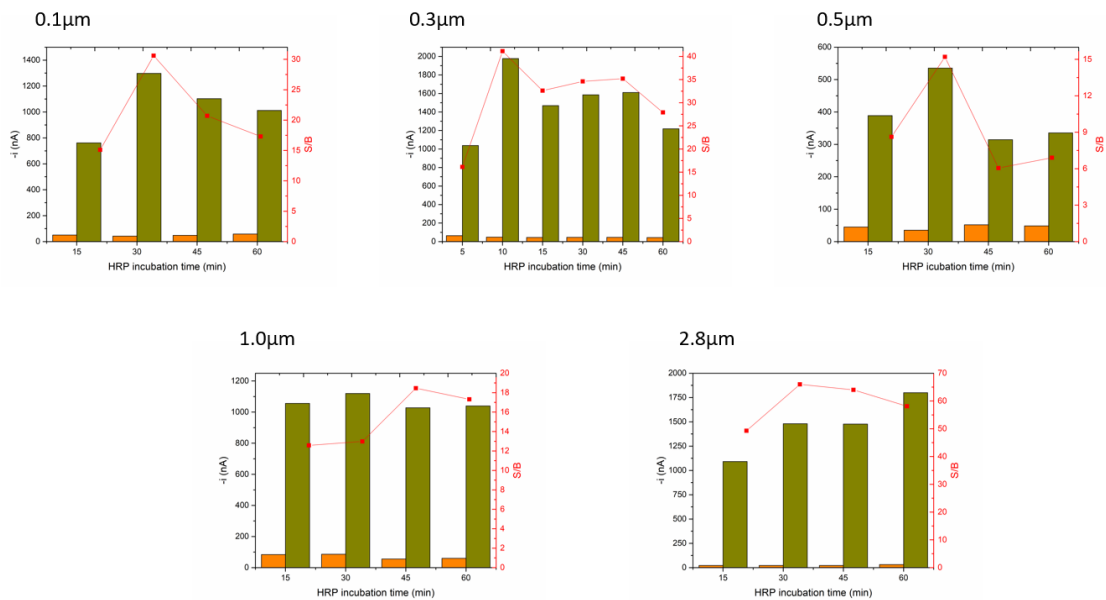


**Figure 4.5:** Optimization for the incubation time of HRP

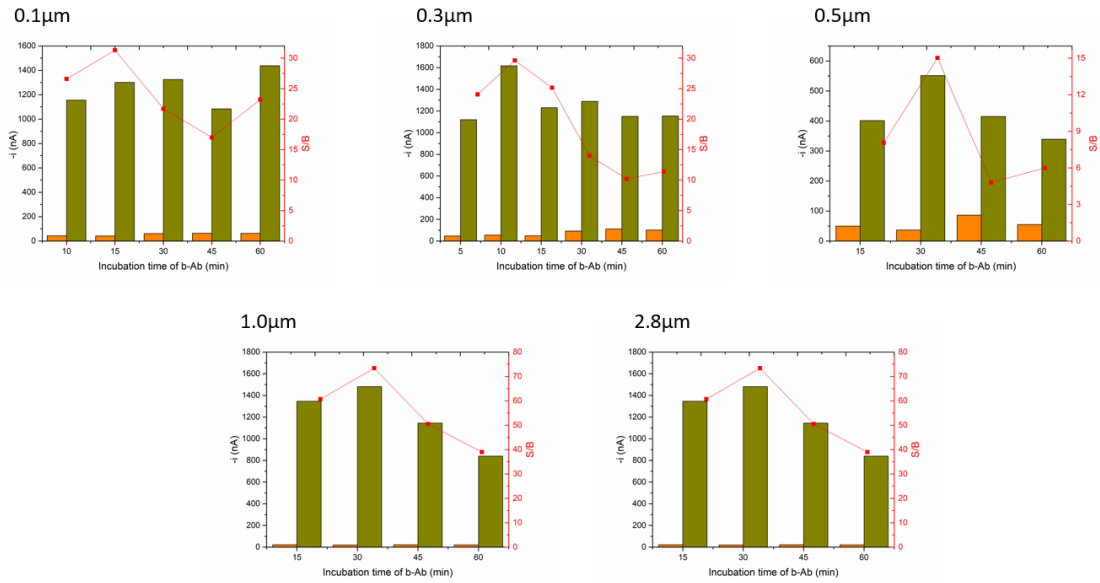


Figure 4.6: Optimization for the incubation time of biotinylated Antibody

## 4.4 Analytical characteristics for the determination of HRP

Under the optimized conditions, figure 4.7(right) displays the amperometric currents for the MBs 2.8 μm. A linear behavior ( $R^2 = 0.992$ ) was observed from 4.9-29.4 ng/mL of HRP and the amperometric read outs are presented in figure 4.7(left). As much as the concentration of the HRP is increased, the amperometric signal is also increased.

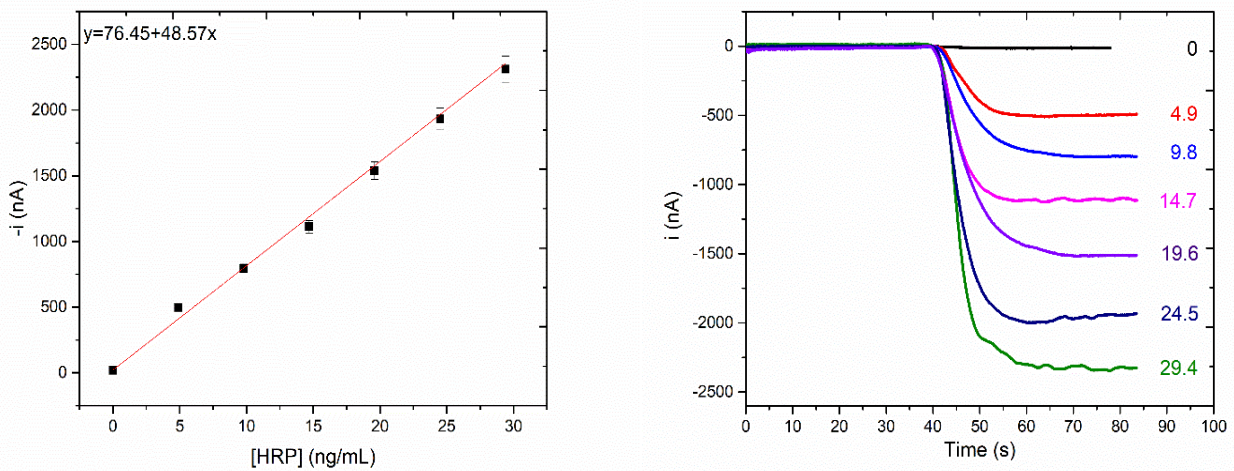
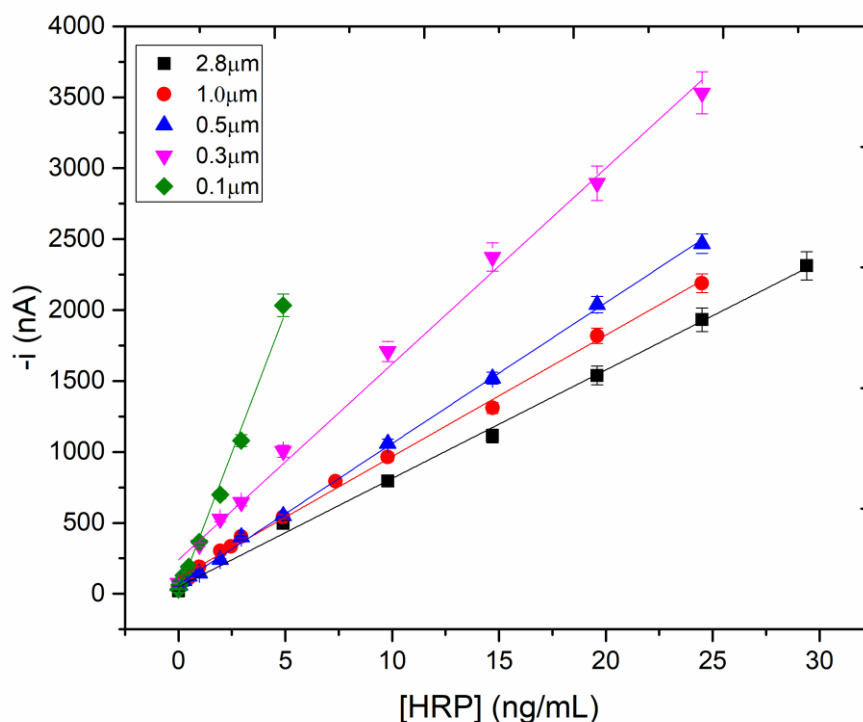


Figure 4.7: Dependence of the amperometric responses with the concentration of HRP standards prepared in buffered solution (left) calibration plot and amperometric traces (right) obtained with the developed immunoplatfrom under optimized working conditions. Range: 0-29.4 ng/mL (b).

According to the previous experimental set-up and the optimal conditions of every MBs size, we perform the same procedure in the same linear range for the rest of the cases. In figure 4.8 is presented the amperometric cathodic current versus the captured HRP concentration for every MBs using the same type SPEs.



**Figure 4.8:** Calibration plots constructed with the developed bio-platform for the amperometric determination of HRP in different concentration ranges.

This amperometric bio-platform is developed for the comparison of amperometric cathodic currents according to the mechanism  $\text{HRP}/\text{H}_2\text{O}_2/\text{HQ}$ . Five different sizes of MBs (0.1-2.8 μm) were tested; the smallest MBs (0.1 μm) presents the highest amperometric readout signal among the rest of the MBs. On the other hand, the largest one (MBs 2.8 μm) obtains the lowest amperometric signal, having the same HRP concentration.

For each case, the limit of detection (LoD) was estimated according to the  $3x S_b/m$  criterion, where  $S_b$  was the standard deviation of 10 measurements obtained in the absence of HRP and  $m$  the slope of each calibration plot. The limit of quantification (LQ) was calculated according to the  $10x S_b/m$ . All the electroanalytical features are presented in the Table T4.2. The differences among the slopes, but also the LoDs, are a result of the different size of MBs. The immobilized HRP in the smaller size of MBs, is oxidized easier than the HRP of the bigger one.

**Table T4.2:** Electroanalytical features for MBs

Size of MBs ( $\mu\text{m}$ )	Linear range (ng/mL)	Slope (nA $\times$ mL/ng)	Intercept (nA)	LoD (ng/mL)	LQ (ng/mL)	RSD (%)	Stability (Days)
2.8	4.9-29.4	74.92	48.57	0.07	0.22	4.3	18
1.0	0.49-24.5	83.85	111.7	0.10	0.35	3.0	14
0.5	0.049-24.5	97.23	63.81	0.06	0.20	2.8	14
0.3	0.98-24.5	132.7	304.7	0.11	0.39	4.2	11
0.1	0.049-4.9	386.6	8.2	0.02	0.06	3.9	11

#### 4.4.1 Mechanism and electron-proton transfer

The reduced form of HRP can be chemically reoxidized by  $\text{H}_2\text{O}_2$ . Generally, direct electron transfer between HRP and an electrode is difficult because of the active sites of HRP which are deeply buried in a thick protein shell. On the other hand, electron transfer via a mediator, is more effective for establishing an electrical connection between the redox centers and the electrode. The principal electrochemical mechanism is presented in figure 4.2. The mediator HQ serves as an electron-proton transfer that enables electrochemical  $\text{O}_2$  reduction in the potential of  $-0.2\text{V}$ , that every electrochemical reaction occurs. The oxidized mediator is electrochemically reduced on the electrode, leading to a raise of the reduction current.

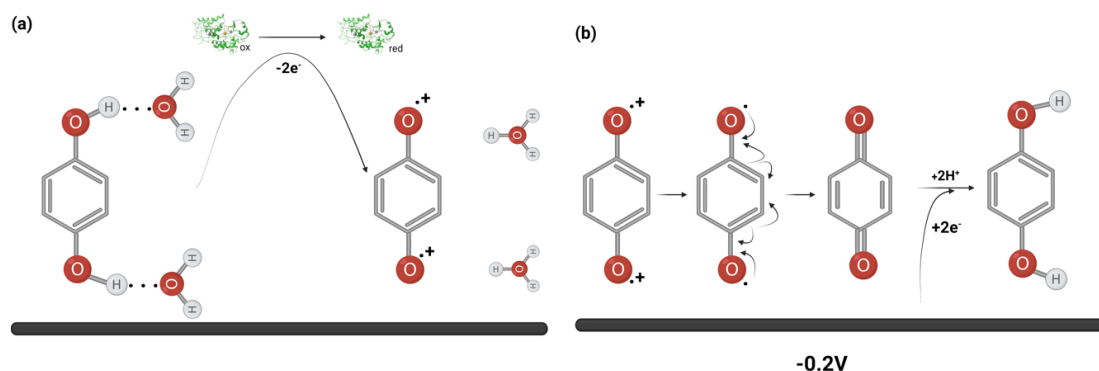


**Figure 4.9:** (a) Enzymatic reaction of HRP (b) The two steps reaction based on proton-electron transfer and the current reaction.

At first, the HQ is oxidized via the enzymatic redox reaction of HRP (figure 4.9a), producing radical cations in 1,4 HQ. This reaction held on the presence of a water molecule which acts as base. Additionally, reactions involved are two-step reactions, where the hydrogen bonds between HRP and HQ in water buffer. The result of this reaction is the production of radical cations which latter undergoes to proton transfer to form HQ radical to carboxylate bond (figure 4.9b). The BQ can easily react with the electrons given by the continuous reduction of the electrochemical system (-0.2V) returning to the principal form of HQ. This reaction is given by 2 electrons and 2 protons. As a result of this procedure, we can measure the different currents through proton- electron transfer.

However, the mechanism mentioned above it clearly depends on the distance between capture HRP and the generation of the radicals in the surface of the electrode. The faster is the generation of the radical (figure 4.9a), the higher is the current production from BQ to HQ (figure 4.9b). In this case, owing the same amount of captured HRP onto MBs surface via an b-Ab, five different sizes of MBs have been tested. Figure 4.10a exhibits the difference in the amperometric response of MBs for 5ng/mL of HRP, versus the exact same time of 80s for every measurement. The addition of H<sub>2</sub>O<sub>2</sub> has been done at 40 seconds of the measurement in each case.

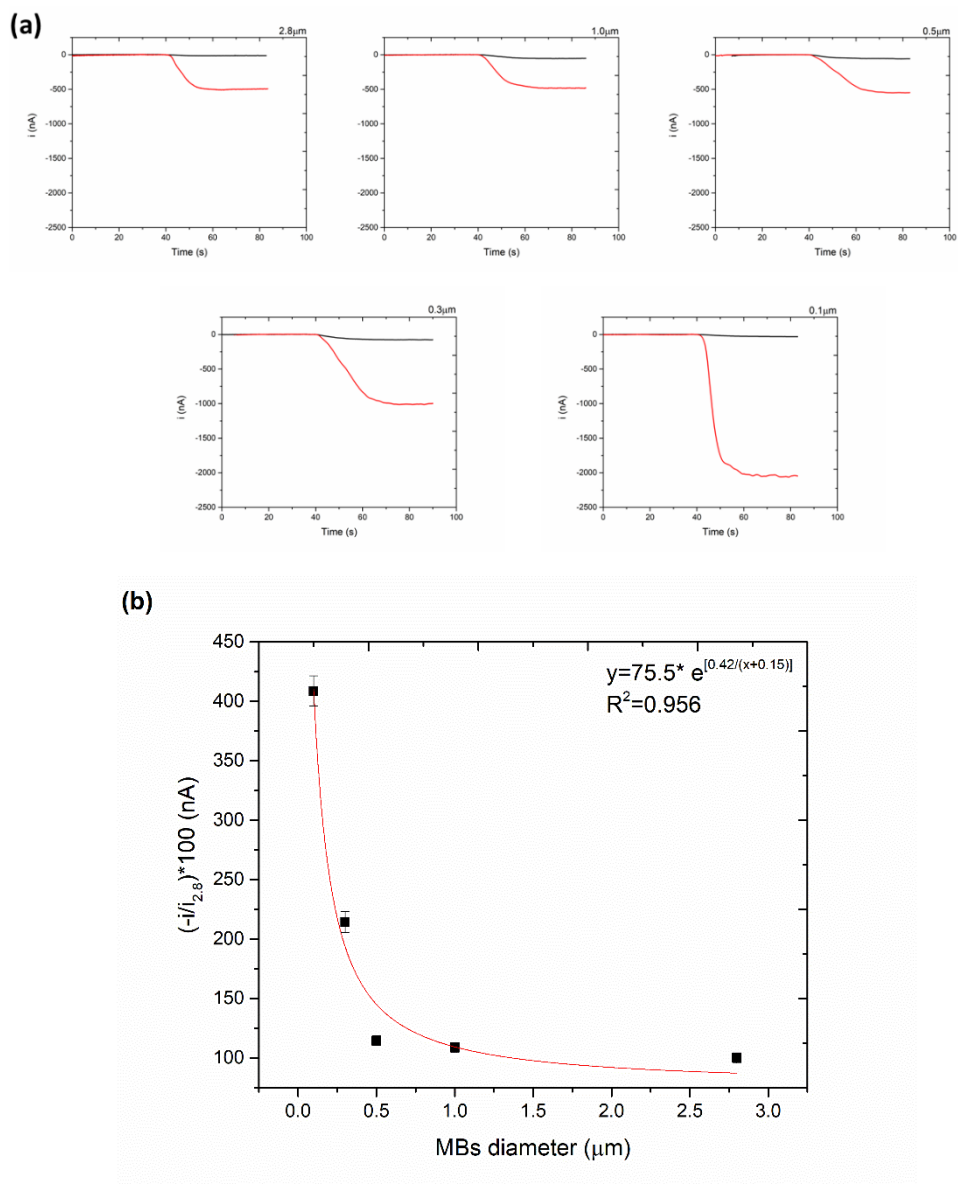


**Figure 4.10:** Amperometric responses for the detection of 5ng/mL of HRP for (a) Different size (0.1-2.8 μm) of MBs (b) Normalized currents vs the MBs diameter.

According to different currents, obtained from different size of MBs, an exponential behavior is presented in figure 4.10b. Every current value has been normalized according to the current of 2.8 μm MBs. The figure 4.10b exhibits the normalized current values of each MBs for a 4.9 ng/mL captured HRP versus to the MBs diameter owing the exponential equation of  $y = 75.5 \times \exp \left[ \frac{0.42}{x+0.15} \right]$ .

## 4.4.2 Stability and capture efficiency

An important factor in the field of electrochemical biosensors is the stability of the system. We examine the electrochemical response of every MBs size in difference days at the range of 0-25 days. The stability of the system is considered the stability of the blank signal (S/B) ration. In figure 4.11 presents the values of S/B ration for every different MBs and in table T4.2 are presented the days of stability. However, the 0.1 $\mu$ m MBs obtained a certain stability for 11 days in contrary of the biggest 2.8  $\mu$ m MBs that the stability is affirmed for 24 days. This phenomenon could be explained by the ability of biomolecules to be immobilized in a standard surface area. In every case the surface of the MBs is saturated by the b-Abs; but the smallest the surface is, the less stability of b-Abs remains.

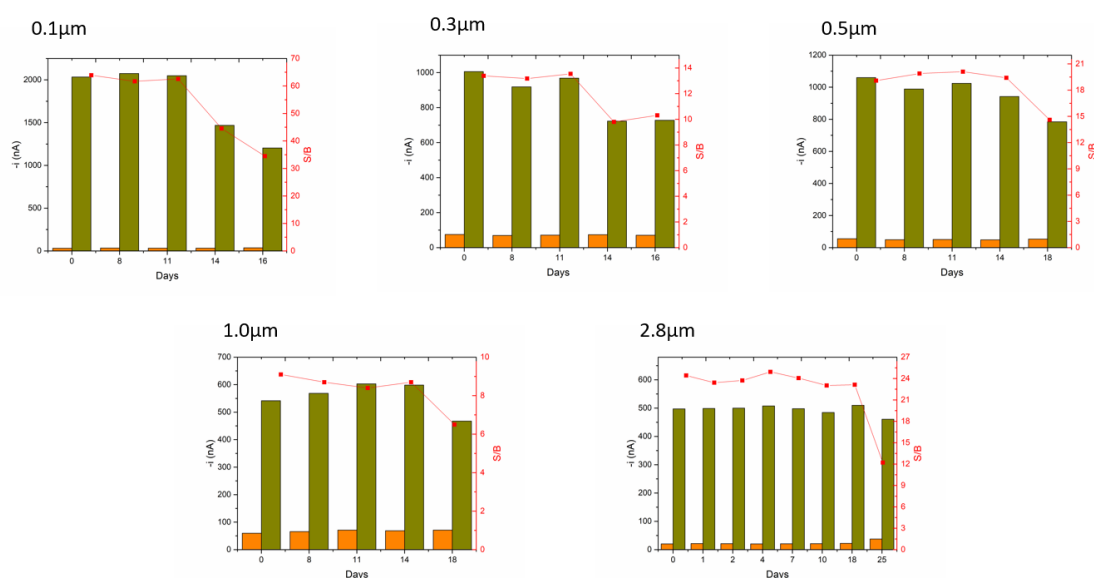


**Figure 4.11:** Control figures constructed to check the storage stability of b-Abs/MBs stored in filtered PBS at 4 °C for the assay format. The amperometric responses were measured in the absence (orange bars, B) or in the presence (green bars, S) of 10 ng/mL HRP standards. The calculated S/B ratios are displayed as red squares.

Furthermore, the capture efficiency of b-Abs has also been investigated using spectrophotometric instrumentation. Different concentrations of HRP have been examined in a range of 1-20 ng/mL (Figure 4.12 a). To detect the specific concentration of HRP we used the system of H<sub>2</sub>O<sub>2</sub> and TMB [33] in a standard concentration of 100mM and 50 $\mu$ M, respectively. The oxidation of TMB in PB pH 6, produces a blue color which changes to yellow with a wide absorbance band at 450 nm in UV-vis spectrum. Initially, this experiment in a homogeneous phase is performed, recording each measurement 5 min after the addition of H<sub>2</sub>O<sub>2</sub>. In the range

of 1-20 ng/mL this system exhibits a linear behavior following the equation represented in figure 4.12 b ( $y=0.02x+0.009$ ) and  $R^2$  equal to 0.993.

In the end, we performed the same procedure separately in HRP/b-Ab/MBs and the remain solution in which the incubation of HRP has been held for a maximum concentration of 20 ng/mL. In a homogeneous phase the maximum absorbance of the system using 20ng/mL of HRP was 0.43 a.u. contrary to the system HRP/b-Ab/MBs which presented of 0.40 a.u. The absorption of the remaining solution was measured at 0.02 a.u., after performing all the washes as they were described above in the experimental section. Figure 4.12 c exhibits analytically the absorbance curves of TMB absorbance in three different cases. According to that, we calculated the captured efficiency of b-Ab owing the value of 98%.

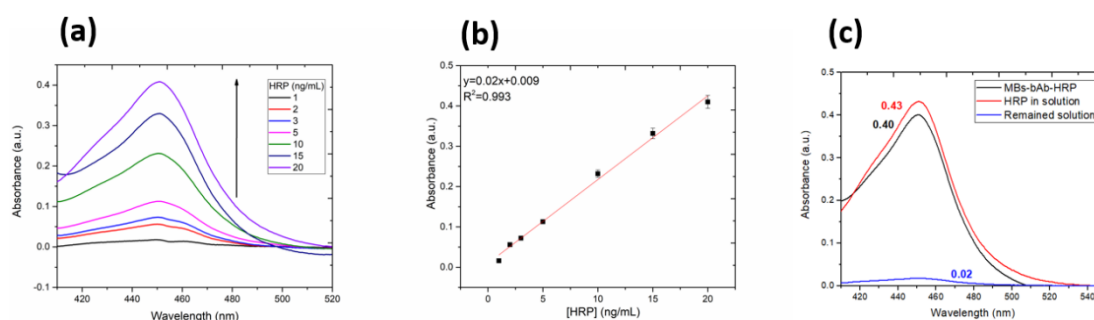


**Figure 4.12:** (a) Fluorescence response of HRP/TMB/H<sub>2</sub>O<sub>2</sub> system in filtered PBS solution using different HRP concentrations (b) Calibration plot of fluorescence response and (c) Absorbance of: (i) HRP/H<sub>2</sub>O<sub>2</sub>/TMB in solution (red curve), (ii) ASSAY of MBs/b-Ab/HRP/H<sub>2</sub>O<sub>2</sub>/TMB (black line) and (iii) remained solution after the separation of MBs. Size of MBs: 2.8 $\mu$ m; Solution PBS pH 6.

## 4.5 Magnetic beads directly conjugated with iridium dyes

The development of organometallic compounds in preference to organic molecules, vis-à-vis bioimaging applications, has been underway for the last few years because they fulfill the stringent criteria associated with these types of materials. The molecular designing of effective phosphorescent materials for bioimaging applications is a challenging task and must entail with high quantum yield. The maximum quantum yield for small fluorophore cannot exceed to 25%, whereas cent percent quantum yield could be achieved in case of phosphorescent metal complexes which is attributed to spin orbit coupling, and singlet-triplet excitation [35-38].

Most streptavidin-based applications require biotinylating of the target molecules. Although chemical biotinylating is straightforward and commonly used, the technique lacks target selectivity and stochastically modifies a broad range of chemically similar groups. On the other hand, several chemoenzymatic techniques developed in recent

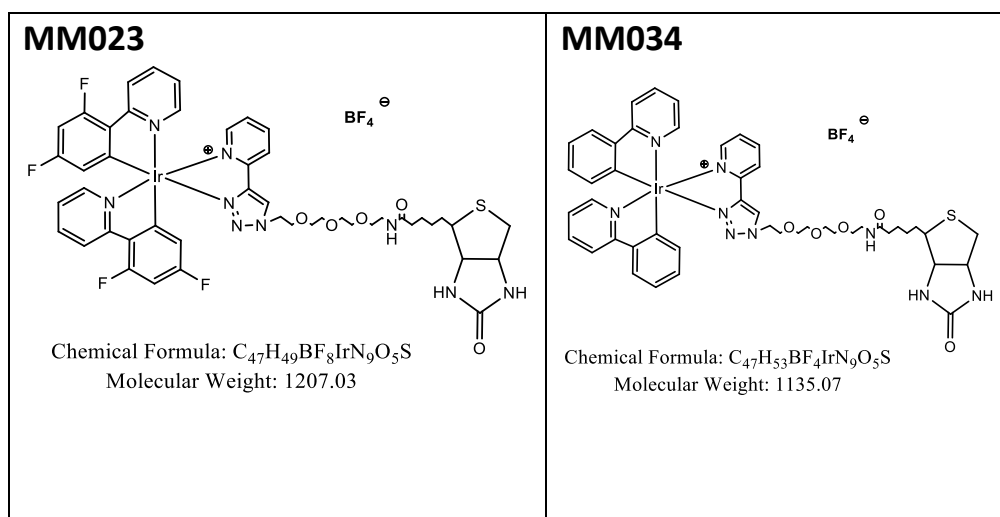


years can introduce selective biotinylation of proteins in cultured cells and in vivo [34]. An alternative to chemical biotinylation includes enzymatic biotinylation, which uses a fused biotin acceptor sequence and a biotin ligase to introduce site-specific modifications [35]. Enzymatic biotinylation results in highly selective modification of a small number of proteins and is appropriate for live cell imaging or for affinity purification and downstream analysis. Together, improvements in biotinylation techniques, both chemical and enzymatic, and newly engineered streptavidin variants have played an important role in advancing the streptavidin–biotin technology in new areas of science.

Biotinylated biomolecules are commonly recognized by fluorophore-labeled streptavidin molecules. Since biotin has four binding sites, it can act as a bridge and biotinylated biomolecules can be recognized by streptavidin-reporter conjugates. However, this strategy does not apply to fluorescent biotin conjugates because they suffer from severe self-quenching upon binding to avidin [36],[37].

In view of this, in collaboration with A. Bossi (CNR Milan) we have recently designed a series of luminescent cyclometalated biotinylated iridium(III) polypyridine complexes. In the chapter 1 the investigation of novel dyes has been done in aprotic conditions instead in this case that the investigation will be held in aqueous solution. According to that, the use of biotin-streptavidin chemistry gives us the opportunity to work in aqueous solution using MBs. Additionally, several studies have noticed that more hydrophobic transition metal biotin conjugates can provide higher degrees of emission enhancement [38],[39]. In consideration of these factors, our luminescent cyclometalated iridium (III) with biotin ligand are presented in the Table T4.3. In such way, the streptavidin-MBs that we used previously can be conjugated directly with iridium dyes.

**Table T4.3:** Cyclometalated iridium (III) with biotin ligand

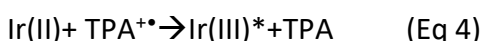
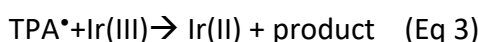
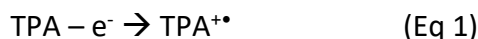


#### 4.5.1 Preparation of MBs@Ir(III) conjugation.

Streptavidin-coated beads with a diameter of 2.8 $\mu\text{m}$  were functionalized with biotinylated iridium complexes. The magnetic beads solution (diameter 2.8  $\mu\text{m}$ ; Dynabeads beads, ThermoFisher scientific, total surface area of  $7 \times 10^9 \mu\text{m}^2$ , 6 mL) was poured in a 20 mL vial, and the beads were collected using a magnet for 2 minutes. Afterwards, iridium complexes dissolved in two individual vials of 15 mL of 0.01M PBS pH 7 in such way that the concentration was 0.83 $\mu\text{M}$  and 0.88 $\mu\text{M}$  for the MM023 and MM034 compound, respectively. Subsequently, 750 $\mu\text{L}$  of str-MBs solution was added in 15 mL of PBS pH 7 solution (0.83 $\mu\text{M}$  of MM023 and 0.88  $\mu\text{M}$  MM034), followed by 3 hours incubation at 37 $^\circ\text{C}$  under rotation to form the biotin-streptavidin bond. The solution was separated with a magnet and the solution was discharged. After the separation of MBs@Ir the last step of incubation was repeated for 2 more time by using supernatant for avoid the aspecific adsorption. After the third incubation step, the MBs@Ir were ready to be placed in the electrochemical cell for the ECL measurements.

#### 4.5.2 Electrochemiluminescence readout for MBs@Ir(III)

After the preparation of conjugated MBs with iridium complex a three-electrode cell was used for the ECL readout. The cell was placed in a small distance from the PMT for the light detection into a dark box. The MBs was remained immobilized onto Pt's surface using a magnet. However, in such case we applied only positive potentials from 0V to +2V given that the presence of TPA. In contrary from the chapter 1 and the annihilation mechanism, in this case we are going to be based on the ECL coreactant mechanism (see chapter of introduction, figure I.1b). Analytically, the mechanism is presented below in equations 1-5:



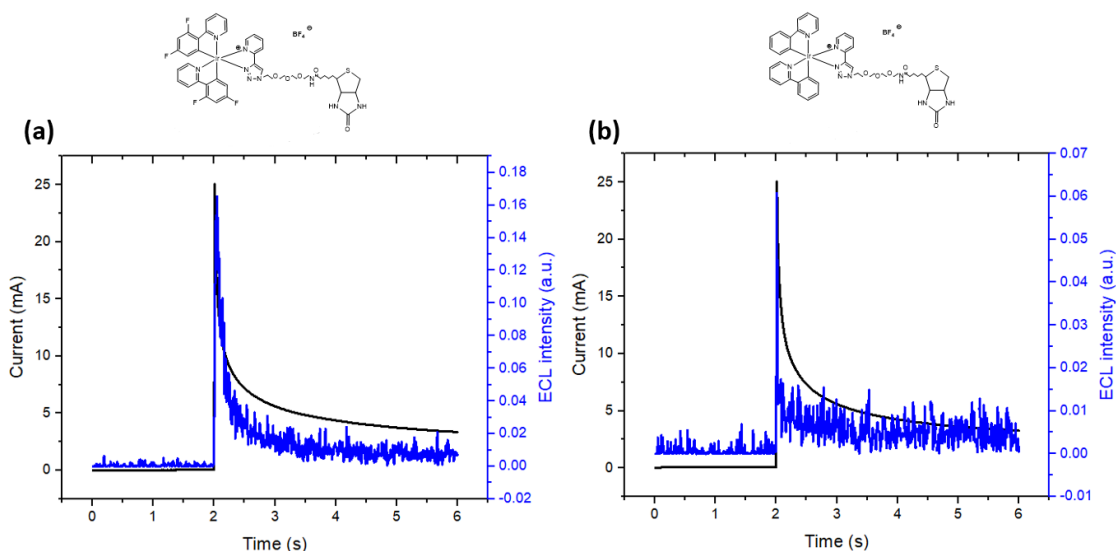


**Figure 4.13:** ECL intensity registered during a chronoamperometric measurement of compound onto MBs of (a)  $0.83\mu\text{M}$  MM023 (b)  $0.88\mu\text{M}$  MM034; Amplification  $0\mu\text{A}$ . Solvent:  $0.1\text{M}$  PBS with  $180\text{mM}$  TPA pH 6.8. Working electrode: Pt wire vs Ag/AgCl electrode; PMT 750V.

Figure 4.13 exhibits the chronoamperometric currents (black line) registered ECL intensity (blue line) of the  $2.8\ \mu\text{m}$  MBs@Ir(III). In the first case (figure 4.13 a), complex MM023 exhibits both ECL intensity and the lifetime of complex are higher than the MPP034 complex (figure 4.13 b). This difference may be for the presence of fluorine in the aromatic ring. The fluorine may give the stability in the iridium complex and enhance the ECL intensity.

On the other hand, here we use a lower amplification ( $0\mu\text{A}$ ) for the detection of the light emission from the chronoamperometric measurements in chapter 1 (please see chapter 1 complexes AB141 and AB 148). Indeed, in this case the ECL intensity is much lower than the ECL intensity we obtained on the aprotic solvents (AcN). This approach is not so effective than the investigation of ECL efficiency in aprotic solution because fluorescent biotin molecules suffer from efficient self-quenching due to resonance-energy transfer (RET). A possible way to resolve this problem is the binding with avidin as it was presented by Lo et al. [40].

Also, the observed quenching is associated with the hydrophobicity of the biotin-binding sites, given that the emission quantum yields, and lifetimes of the complexes are higher and longer in more nonpolar solvents (such as acetonitrile), instead of the polar solvents (such as PBS).

## 4.6 Conclusions

In this chapter we replaced the electrochemical surface with MBs. At first, a simply amperometric sensor, dependent on the size of the MBs, was developed based on a standard electroanalytical system (HQ/H<sub>2</sub>O<sub>2</sub>) for the detection of HRP. The recommended strategy relies on the covalent attachment of a biotinylated antibody onto MBs which is capable to capture the HPR molecules. Applying a constant negative potential (-0.2V) and registering the amperometric curves, a different value of LoD was calculated each time.

The 0.1 $\mu$ m MBs exhibit the best electrochemical response owing a really low LoD equal to 0.02ng/mL. These results demonstrate an exponential behavior between the size of MBs and the current of a standard HRP concentration. The use of smaller size MBs could be a way to decrease the limit of detection of an electrochemical based biosensor without any amplification.

Moreover, a direct conjugation of Iridium complexes has been performed, taking advantage of the strong covalent bond between streptavidin and biotin. This system can be used in biosensors application conjugating biomolecules such as antibodies and preparing assays. However, iridium complexes from chapter 1 have been modified by biotin ligand; so they can be bonded onto MBs. ECL emission has been registered but a quench phenomenon is observed according to RET theory. Biotinylated Iridium dyes could potentially be applied as ECL luminophores modified MBs in water, by exploring their ECL proprieties. Such strategy is currently under analysis in our laboratory for the development of a multicolor biosensors.

## References

- [1] O. Philippova et al, *Eur. Polym. J.* 47 (2011) 542–559.
- [2] C. Albretsen et al, *Anal. Biochem.* 189 (1990) 40–50.
- [3] W. Wu et al, *Sci. Technol. Adv. Mater.* 16 (2015).
- [4] Z. Chen et al, *Chinese Chem. Lett.* 29 (2018) 1601–1608.
- [5] M. Duan et al, *Nanotechnology.* 29 (2018).
- [6] N. Jaffrezic-Renault et al, *Sensors.* 7 (2007) 589–614.
- [7] I.M. Hsing, Y. Xu, W. Zhao, *Electroanalysis.* 19 (2007) 755–768.
- [8] S. Solé et al, *TrAC - Trends Anal. Chem.* 20 (2001) 102–110.
- [9] L. Stanciu et al, *Sensors.* 9 (2009) 2976–2999.
- [10] E.P. Randviir et al, *Mater. Today.* 17 (2014) 426–432.
- [11] R. A. Marcus, *J. Chem. Phys.* 24 (1955) 966–978.

- [12] S. Ge et al, *Biosens. Bioelectron.* 49 (2013) 111–117.
- [13] V. Pérez-Ginés et al, *Biosens. Bioelectron.* X. 11 (2022).
- [14] N. Gan et al, *Int. J. Electrochem. Sci.* 6 (2011) 5146–5160.
- [15] J. Hou et al, *Int. J. Electrochem. Sci.* 6 (2011) 2845–2858.
- [16] W. Zhan et al, *Anal. Chem.* 79 (2007) 459–463.
- [17] M. Li et al, *Electroanalysis.* 22 (2010) 333–337.
- [18] N. Gan et al, *Sensors.* 11 (2011) 7749–7762.
- [19] T.L. Pittman et al, *Anal. Chim. Acta.* 632 (2009) 197–202.
- [20] Y. Bing Tang et al, *Anal. Chim. Acta.* 582 (2007) 275–280.
- [21] J. Wei, B. Wu, *Sensors Actuators, B Chem.* 139 (2009) 429–434.
- [22] X. Zhou et al, *Electrochem. Commun.* 10 (2008) 564–567.
- [23] D. Zhu et al, *Biosens. Bioelectron.* 24 (2009) 3306–3310.
- [24] J.L. Liu et al, *Anal. Chem.* 93 (2021) 10890–10897.
- [25] N. Wang et al, *Angew. Chemie - Int. Ed.* 60 (2021) 197–201.
- [26] P. Wang et al, *Anal. Chem.* 93 (2021) 15785–15793.
- [27] L. Zhang et al, *Anal. Chem.* 93 (2021) 4628–4634.
- [28] L. Yang et al, *Anal. Chem.* 93 (2021) 16906–16914.
- [29] L. Lu et al, *Anal. Chem.* 90 (2018) 11716–11722.
- [30] X. Wang et al, *Anal. Chem.* 93 (2021) 14178–14186.
- [31] F. Yang et al, *Biosens. Bioelectron.* 173 (2021) 112820.
- [32] G. Yang et al, *Biosens. Bioelectron.* 216 (2022) 114629.
- [33] L. Gao et al, *ACS NA.* 5 (2011) 6736–6742.
- [34] M.W.L. Popp et al, *PLoS Pathog.* 8 (2012) 1–16.
- [35] J. Kim et al, *Nat. Protoc.* 4 (2009) 506–517.
- [36] H.J. Gruber et al, *Bioconjug. Chem.* 8 (1997) 552–559.
- [37] M. Marek et al, *Bioconjug. Chem.* 8 (1997) 560–566.
- [38] K.K.W. Lo et al, *J. Am. Chem. Soc.* 124 (2002) 9344–9345.
- [39] K.K.W. Lo, K.H.K. Tsang, *Organometallics.* 23 (2004) 3062–3070.
- [40] K.K. Lo et al, *Organometallics.* 23 (2004) 3108–3116.

## CONCLUSIONS AND PERSPECTIVES

Electrochemistry is a powerful analytical technique, very promising for ultrasensitive biomarker analysis, early disease diagnosis sensors, environmental investigations, and monitoring of chemical and biological process.

Electrochemiluminescence is a technique based on electrochemistry and many different strategies is used for increasing ECL efficiency, nevertheless, further increase of sensitivity can be for its biosensor application. In this study, based on different strategies, we evaluate the substitution of metal-based dyes and the use of Mox as working electrodes. Furthermore, an ultrasensitive sensor has been developed using a novel study approach. As a final point, we established the replacement of the standard electrode surfaces with MBs and the enhancement of EC signal.

In a more analytical way, novel rational synthetic strategies prompted the development of nanomaterials with suitable features for increasing luminophores efficiency. Thermally activated delayed fluorescence materials (TADF) and BODIPYs have been studied and showed a huge ECL signal owing a high ECL efficiency. The aprotic solvent (AcN) helps the annihilation mechanism of ECL emission; thus, this type of materials exhibits a huge difficulty to be dissolved in aqueous solutions. Especially dyes such as **4DPA\_2Br\_IPN** and **OxaBo3** presents a high ECL efficiency of 7.6% and 20%, respectively, instead of a metal-based dyes such as  $[Ru(phen)_2dppz]^{2+}$  (0.02%) and Iridium complexes (<8%).

In ECL field, another important aspect is the nature of the electrode surface. New titanium dioxide (TiO<sub>2</sub>) porous nanomaterials have been used for ECL application based on the standard dye-coreactant system ( $[Ru(bpy)_3]^{2+}$  - TPA). On one hand, the use of high potentials is necessary for the oxidation of both dyes-coreactant molecules. On the other hand, a specific functionalization (using zirconium) was used for the immobilization of ruthenium complex onto porous nanoparticles of TiO<sub>2</sub>; thus, the investigation of two different ECL mechanisms occurs. The distance between the electrode surface and the immobilized ruthenium complex can affect both the ECL generation mechanism and ECL intensity.

In conclusion, electrochemiluminescence has been successfully exploited for analytical application also through studies on the ECL mechanism generation. A novel approach has been used without any sequence or signal amplification for the determination of whole viral genome such as the ds-DNA of HBV and the RNA of COVID-19. The results were useful for developing biosensor for early disease diagnosis in real samples of positive patients. This recent biosensor is of greater prominence due the crucial importance of the biosensors according to the pandemic disease of 2019. Our technique demonstrates a really low LoD equal to 2.7 cps/mL for HBV and 14 cps/ $\mu$ L for the COVID-19 genome.

The combination of micromagnetic beads immunoassay and the electrochemical applications can enhance the sensitivity using a novel approach only by changing the dimensions of the MBs. The investigation of the electrochemical mechanism of a standard system mechanism of HRP/HQ/H<sub>2</sub>O<sub>2</sub> showed an enhanced signal mechanism at short distances (< 1 μm) from the electrode surface. In shorter distances we obtain a really low limit of detection for the analyte of HRP.

The investigation of new luminophores, the new nanoporous materials replacing the commercial electrode surfaces guide us to the expansion of biosensors and the study of new mechanisms which can also be applied for diagnostic reasons.

To sum up, electrochemiluminescence and electrochemistry have been successfully exploited for analytical purposes also through studies on the ECL/EC mechanism generation. Mechanistic investigations singled out different strategies for increasing both the intensity and efficiency in our system. The results were useful for developing biosensors, applied in early disease diagnosis and clinical monitoring. The recent strategies also gave an important boost towards an enhancement of ECL/EC signal for the detection of biomarkers in bioanalytical applications.

## Ringraziamenti / Acknowledgements / Ευχαριστίες

A questo punto vorrei ringraziare tutti voi che mi siete stati vicini a questi 3 anni difficili di dottorato. Σε αυτό το σημείο να ευχαριστήσω όλους όσους ήταν δίπλα μου αυτά τα 3 χρόνια.

Αρχικά ένα μεγάλο ευχαριστώ στην οικογένειά μου. Την μητέρα μου που όλα αυτά τα χρόνια ήταν είναι και θα είναι δίπλα μου, την μικρή μου (που μόνο μικρή δεν την λες) αδερφή (Γκοοοοφρετ), και φυσικά τον πατέρα μου. ΠΑΤΕΡΑ ΤΑ ΚΑΤΑΦΕΡΑ ΜΕ!! Επιτέλους μετά από χρόνια (είναι λίγο πολλά αλλά χαλάλι) ο κύκλος κλείνει! Τα καταφέραμε ΜΑΖΙ, και ΜΑΣ έφεραν εδώ όλες οι συζητήσεις-δύσκολες στιγμές σε πιλότους, σε χωράφια, σε κουβαλήματα κτλ. Δεν θα άλλαζα ούτε μια από αυτές τις στιγμές και αν μπορούσα να τις ξαναζήσω, ευχαρίστως θα τις ξαναζούσα μαζί σου. Ευχαριστώ λοιπόν και τους τρεις σας για ό,τι στερηθήκατε και ό,τι κάνατε για εμένα.

Grazie ai miei professori, colleghi, tesisti, e collaboratori di EMFM Lab. Grazie Lorenzo, Miriam, Sara, Claudio, Alessandra, Sandro, Maila per avermi sopportato in lab. Vorrei anche ringraziare i miei supervisor per la possibilità che mia hanno dato di effettuare il mio dottorato al loro gruppo.

I would like to thank Professor Susana Campuzano from Universidad de Madrid (UCM) for accepting and hosting me in her group in Madrid. I also thank GEBE group for these 4 amazing months I have spent with them. Especially I would like to thank my friends Viktor, Rebe, Eloy, Veronica and Cristina for all of the moments, conversations we had during my period on abroad. Not only my scientific skills have been improved but also my personal skills and thank you for that.

Dunque, è sempre bello e affascinante guardare la parte scientifica (nuove scoperte, cose che non sapevi che esistessero) però cosa succede fuori dal lab? Cosa succede quando torni a casa distrutto da lavoro dopo giorni e giorni sotto una cappa? Forse la parte più difficile è tornare a casa e sentirsi a casa e non sentirsi ingabbiato dentro quella. Grazie piccola morbida Giugi per avermi fatto sentire ogni giorno a casa e per dividerla con me. Grazie di starmi vicina ai momenti difficili ma anche felici, grazie che hai sempre creduto in me.

Ένα μεγάλο ευχαριστώ στον αδελφικό μου φίλο Δημήτρη που μεγαλώσαμε αλλά και ωριμάσαμε μαζί. Μια τέτοια φίλια δεν “καταλαβαίνει” από αποστάσεις και δυσκολίες. Ακόμα, ένα ξεχωριστό ευχαριστώ στον φίλο μου Γεράσιμο που τα τελευταία χρόνια είναι δίπλα μου σε δύσκολες αλλά και χαρούμενες στιγμές. Ευχαριστώ αυτά τα δύο άτομα που σπανίζουν στις μέρες μας.

Ένα ξεχωριστό ευχαριστώ στην φίλη μου Μυρτώ, που μέσα από τις συζητήσεις αλλά και αντιπαραθέσεις μας, με βοήθησε να δω διαφορετικά ορισμένες καταστάσεις. Ευχαριστώ από καρδιάς που σε όποια δυσκολία και αν είχα ήσουν πάντα δίπλα μου και πάντα πίστευες σε εμένα.

Grazie a tutti voi di via Irnerio 17, per i nostri momenti e il loro supporto ai miei momenti un po' difficili. Grazie di cuore Peppe, Roberto, Berza, Fede, Alice. Senza di



voi forse sarei rimasto senz'altro :) Grazie ai miei amici di palestra che senza di loro non sarei mai riuscito ad imparare l'italiano (non e' vero... pero'), grazie di cuore Enzo, Dema, Aurora, Alessandro, Sandro, Valentina, Antonia, Daniele, Davide e Riccardo.

Grazie a tutti voi.